

SI AND $\text{Si}_{1-x}\text{Ge}_x$ NANOCRYSTALS: SYNTHESIS, STRUCTURAL
CHARACTERIZATION, AND SIMULTANEOUS OBSERVATION OF QUANTUM
CONFINED AND INTERFACE RELATED PHOTOLUMINESCENCE

A THESIS SUBMITTED TO
THE GRADUATE SCHOOL OF NATURAL AND APPLIED SCIENCES
OF
MIDDLE EAST TECHNICAL UNIVERSITY

BY

NADER ASGHAR POUR MOGHADDAM

IN PARTIAL FULFILLMENT OF THE REQUIREMENTS
FOR
THE DEGREE OF DOCTOR OF PHILOSOPHY
IN
PHYSICS

MARCH 2010

Approval of the thesis:

**SI AND $SI_{1-x}GE_x$ NANOCRYSTALS: SYNTHESIS, STRUCTURAL
CHARACTERIZATION, AND SIMULTANEOUS OBSERVATION OF QUANTUM
CONFINED AND INTERFACE RELATED PHOTOLUMINESCENCE**

submitted by **NADER ASGHAR POUR MOGHADDAM** in partial fulfillment of the requirements for the degree of
Doctor of Philosophy in Physics Department, Middle East Technical University by,

Prof. Dr. Canan Özgen
Dean, Graduate School of **Natural and Applied Sciences**

Prof. Dr. Sinan Bilikmen
Head of Department, **Physics**

Prof. Dr. Raşit Turan
Supervisor, **Physics Department, METU**

Examining Committee Members:

Prof. Dr. Çiğdem Erçelebi
Physics Department, METU

Prof. Dr. Raşit Turan
Physics Department, METU

Prof. Dr. Macit Özenbaş
Metallurgical and Materials Engineering Department, METU

Prof. Dr. Atilla Aydınlı
Physics Department, Bilkent University

Asist. Prof. Dr. Hande Toffoli
Physics Department, METU

Date:

I hereby declare that all information in this document has been obtained and presented in accordance with academic rules and ethical conduct. I also declare that, as required by these rules and conduct, I have fully cited and referenced all material and results that are not original to this work.

Name, Last Name: NADER ASGHAR POUR MOGHADDAM

Signature :

ABSTRACT

SI AND $\text{Si}_{1-x}\text{Ge}_x$ NANOCRYSTALS: SYNTHESIS, STRUCTURAL CHARACTERIZATION, AND SIMULTANEOUS OBSERVATION OF QUANTUM CONFINED AND INTERFACE RELATED PHOTOLUMINESCENCE

Moghaddam, Nader Asghar Pour
Ph.D., Department of Physics
Supervisor : Prof. Dr. Raşit Turan

March 2010, 104 pages

In this work we have prepared Si and $\text{Si}_{1-x}\text{Ge}_x$ nanocrystals by rf magnetron co-sputtering method. The effect of annealing parameters and Ge content of x on the structural and optical properties sandwiched $\text{SiO}_2/\text{SiO}_2$: Si: Ge/ SiO_2 nanostructures have been investigated. For characterization we have used cross-sectional high resolution electron microscope (HREM), X-ray diffraction (XRD), Raman spectroscopy (RS), Fourier transform infrared (FTIR), photoluminescence (PL), and temperature dependent PL (TDPL) techniques.

It was shown that Ge content of x , annealing temperature, and annealing time are important parameters affecting the structural and optical properties of the nanocrystals. We have observed a uniform $\text{Si}_{1-x}\text{Ge}_x$ nanocrystal formation upon annealing at relatively low temperatures and short annealing time. However, Ge-rich $\text{Si}_{1-x}\text{Ge}_x$ nanocrystals do not hold their compositional uniformity when annealed at high temperatures for enough long time. A segregation process leads to the separation of Ge

and Si atoms from each other and formation of Si-rich core covered by a Ge-rich shell. Related to the optical properties of Si and $\text{Si}_{1-x}\text{Ge}_x$ nanocrystals, influence of annealing treatments and Ge content of x on the simultaneous observation and relative contribution of quantum confined and interface related radiative emission to PL spectra are investigated. On the other hand, temperature dependent photoluminescence (TDPL) measurements have been applied to investigate in detail the involving PL mechanisms and the competing thermally activated emission process and the thermally activated escape process of carriers into nonradiative recombination centers and/or tunneling of the excitons into the interface or to larger nanocrystals.

Keywords: $\text{Si}_{1-x}\text{Ge}_x$ Nanocrystals, Quantum Confined Effects, Defects, Structural Characterization, Optical Characterization.

ÖZ

SI VE $Si_{1-x}Ge_x$ NANOKRISTALLERİ: SENTEZLENMESİ, YAPISAL KARAKTERİZASYONU VE QUANTUM HAPSOLMA VE ARAYÜZEY KAYNAKLI FOTOLÜMINESANSININ AYNI ANDA GÖZLENMESİ

Moghaddam, Nader Asghar Pour
Doktora, Fizik Bölümü
Tez Yöneticisi : Prof. Dr. Raşit Turan

Mart 2010, 104 sayfa

Bu çalışmada Si ve $Si_{1-x}Ge_x$ nanokristaller rf magnetron eş saçırma yöntemiyle hazırlandı. Tavlama parametreleri ve Ge içeriğinin (x) SiO_2/SiO_2 : Si: Ge/ SiO_2 katmanlı yapısının oluşumuna, gelişimine ve yapısal ve optik özelliklerine etkileri incelenmiştir. Karakterizasyon için kesitsel yüksek çözünürlüklü elektron mikroskobu, X-ışını kırınım (XRD), Raman spektrometresi (RS), Fourier dönüşümü kızılötesi (FTIR), fotolüminesans (PL) ve sıcaklık bağımlı PL (TDPL) teknikleri kullanıldı.

Ge içeriğinin (x), tavlama sıcaklığı ve zamanının nanokristallerin yapısal ve optik özelliklerini etkileyen önemli parametreler oldukları görüldü. Göreceli olarak düşük sıcaklıklarda ve kısa tavlama zamanlarında düzenli $Si_{1-x}Ge_x$ nanokristal oluşumu gözlemlendi. Fakat Ge-zengin $Si_{1-x}Ge_x$ nanokristaller yüksek sıcaklıklarda gerektiği kadar uzun süre tavlандıklarında birleşim düzenini kaybetmektedirler. Ayrışma işlemi Ge ve Si atomlarının birbirlerinden ayrılmasına ve Si-zengin çekirdeğin Ge-zengin kabukla sarmalandığı yapının oluşmasına neden olmaktadır. Si ve $Si_{1-x}Ge_x$ nanokristal-

lerin optik özellikleriyle ilgili olarak, tavlama işleminin ve Ge içeriğinin (x) quantum hapsolme ve arayüzey kaynaklı ışınımsal emisyonun birlikte gözlemlenmesine ve bunların göreceli olarak PL spektrumuna katkı sağlamasına etkisi incelenmiştir. Diğer yandan, sıcaklık bağımlı PL ölçümleri (TDPL) olası PL mekanizmalarının detaylı olarak incelenmesi ve termal olarak aktif hale gelen taşıyıcıların ışınımsal olmayan merkezlere kaçıışı ve veya excitonların arayüze veya daha büyük nanokristallere tünellemesini incelemek için yapıldı.

Anahtar Kelimeler: $\text{Si}_{1-x}\text{Ge}_x$ Nanokristalleri, Quantum Hapsolma Etkileri, Defectler, Yapısal Özellikler, Optiksel Özellikler

To: My Family

ACKNOWLEDGMENTS

First of all, I would like to express my gratitude to my supervisor Prof. Dr. Raşit Turan, for having provided me excellent working conditions, encouragement and guidance throughout this study. I am grateful to the examining committee members Prof. Dr. Çiğdem Erçelebi, Prof. Dr. Macit Özenbaş, Prof. Dr. Atilla Aydınlı, and Asst. Prof. Dr. Hande Toffoli for their valuable hints helped and encouraged me to go ahead with my thesis. The author is most grateful to his family members for their continued moral support. I wish to thank all colleagues and friends from the lab. Thanks to Arif Sinan Alagöz, Selcuk Yerci, Ayşe Seyhan, Arife Gencer Imer, Mustafa kulakci, Ilker Yıldız, Umut Bostancı, Buket Kaleli, Döndü Şahin, Ilker Doğan, Urcan Güler, and Zeynep Deniz Eygi. I would like to express my thanks to Terje G. Finstand and Stainer Foss for TEM measurements. I also would like to thank the Turkish Ministry of Education and Scientific and Technical Research Council of Turkey (TUBITAK) for financial support during this study.

TABLE OF CONTENTS

ABSTRACT	iv
ÖZ	vi
DEDICATION	viii
ACKNOWLEDGMENTS	ix
TABLE OF CONTENTS	x
LIST OF FIGURES	xiii
CHAPTERS	
1 INTRODUCTION	1
2 PHYSICAL AND ELECTRONIC PROPERTIES OF BULK Si, Ge, AND $\text{Si}_{1-x}\text{Ge}_x$ AND THE SIZE ISSUE	4
2.1 Motivation	4
2.1.1 Physical Properties of Si, Ge, and $\text{Si}_{1-x}\text{Ge}_x$	4
2.1.2 Band Structure of Si, Ge, and $\text{Si}_{1-x}\text{Ge}_x$	5
2.2 Quantum Confinement Effect	6
3 SYNTHESIS OF Si, AND $\text{Si}_{1-x}\text{Ge}_x$ NANOCRYSTALS IN SiO_2 MATRIX BY RF MAGNETRON CO-SPUTTERING: EXPERIMENTAL PROCEDURES	9
3.1 A Brief Review of the Preparation Methods	9
3.2 Synthesis of Si and $\text{Si}_{1-x}\text{Ge}_x$ Nanocrystals by rf Magnetron Co-sputtering Method	11
3.2.1 Sputtering Parameters	14
3.2.2 Annealing Treatments	16
4 STRUCTURAL CHARACTERIZATION OF THE Si AND $\text{Si}_{1-x}\text{Ge}_x$ NANOCRYSTALS EMBEDDED IN SiO_2 MATRIX	17
4.1 Transmission Electron Microscopy (TEM)	17
4.1.1 Experimental Results	18

4.2	X-Ray Photoemission Spectroscopy (XPS)	26
4.2.1	Experimental Results	26
4.3	X-Ray Diffraction Spectroscopy (XRD)	28
4.3.1	Experimental Results	31
4.4	Fourier Transform Infrared Spectroscopy (FTIR)	34
4.4.1	Experimental Results	35
4.5	Raman Spectroscopy	36
4.5.1	Experimental Results	37
5	OBSERVATION OF CORE-SHELL STRUCTURE IN $\text{Si}_{1-x}\text{Ge}_x$ NANOCRYSTALS	39
5.1	Motivation	39
5.2	Experimental Details	41
5.3	Observation of Core-Shell Structure by TEM	42
5.4	Deconvolution of the XRD Peaks	45
5.5	Further Support from Raman Spectroscopy	47
6	OPTICAL CHARACTERIZATION OF THE Si NANOCRYSTALS EMBEDDED IN SiO_2 MATRIX IN WEAK QUANTUM CONFINED REGIME	51
6.1	Quantum Confined Effect vs Interface Related Radiative Recombination	52
6.2	Annealing Treatment Evolution of the PL Spectra from Si Nanocrystals in Weak Quantum Confined Regime	54
6.2.1	Annealing Treatment Evolution of the X-Ray Diffraction Spectra	55
6.2.2	Annealing Temperature Evolution	57
6.2.3	Annealing Time Evolution	62
6.3	Temperature Dependent PL Spectra from Si Nanocrystals	63
6.3.1	Temperature Dependent Evolution of the Integrated PL Intensity	63
6.3.2	Temperature Dependent Evolution of the PL Energy	66
6.4	Si=O Double Bonds in the Interface, Further Support by FTIR Spectroscopy	69
6.5	Influence of Annealing Time and Temperature on the TDPL of the Si Nanocrystals	74

7	OPTICAL CHARACTERIZATION OF THE $\text{Si}_{1-x}\text{Ge}_x$ NANOCRYSTALS EMBEDDED IN SiO_2 IN WEAK QUANTUM CONFINED REGIME MATRIX	77
7.1	Motivation	77
7.2	Experimental Details	79
7.3	Annealing Treatment Evolution of the PL Spectra from the Samples with $P_{Ge} = 0$ W (Si Nanocrystals)	80
7.4	Annealing Treatment Evolution of the PL Spectra from $\text{Si}_{1-x}\text{Ge}_x$ Nanocrystals with $P_{Ge} = 10$ W	82
7.5	Evolution of the PL Spectra from $\text{Si}_{1-x}\text{Ge}_x$ Nanocrystals with the Same Annealing Treatment and Different $P_{Ge} = 0, 5, 10,$ and 20 W	85
8	CONCLUSION	88
	REFERENCES	90
	VITA	98

LIST OF FIGURES

FIGURES

Figure 2.1	The diamond lattice structure of silicon and germanium.	5
Figure 2.2	Band structures of silicon and germanium. In the case of silicon two results are presented: nonlocal pseudopotential (solid line) and local pseudopotential (dashed line) [7].	6
Figure 2.3	Band-gap energy of random bulk $\text{Si}_{1-x}\text{Ge}_x$ alloys as a function of the Ge mole fraction x . Inset: lattice parameter of the alloy. The solid line is Dismukes's law [10].	7
Figure 3.1	Schematic diagram of capacitive coupled sputtering system [42].	12
Figure 3.2	The nano-D 100 sputtering system.	14
Figure 3.3	The sputtering chamber.	15
Figure 4.1	Cross-sectional TEM image of the samples annealed at 900 (a), 1000 (b), and 1100 °C (c) for 1 <i>h</i>	19
Figure 4.2	High resolution cross-sectional TEM image of the samples annealed at 900 °C for 1 <i>h</i>	19
Figure 4.3	Size distribution of the nanocrystals in the sample annealed at 900 (a), 1000 (b), and 1100 °C (c) for 1 <i>h</i>	20
Figure 4.4	Selected area diffraction patterns of the samples annealed at 900 (a), 1000 (b), and 1100 °C (c) for 1 <i>h</i>	21
Figure 4.5	Cross-sectional TEM image of the samples annealed at 1100 °C for 1 (a), 3 (b), and 5 <i>h</i> (c).	22
Figure 4.6	Size distribution of the nanocrystals in the sample annealed at 1100 °C for 1 (a), 3 (b), and 5 <i>h</i> (c).	22

Figure 4.7 Selected area diffraction patterns of the samples annealed at 1100 °C for 1 (a), 3 (b), and 5 h (c).	23
Figure 4.8 Cross-sectional TEM image of the samples with P_{Ge} of 5 (a), 10 (b), and 20 W (c) and annealed at 1100 °C for 1 h.	24
Figure 4.9 Size distribution of the nanocrystals in the sample with P_{Ge} of 5 (a), 10 (b), and 20 W (c) and annealed at 1100 °C for 1 h.	24
Figure 4.10 Selected area diffraction patterns of the samples with P_{Ge} of 5 (a), 10 (b), and 20 W (c) and annealed at 1100 °C for 1 h.	24
Figure 4.11 The higher hkl reflections of the sample annealed at 900 °C for 1 h (a), and a superposition of Ge and Si (531) reflection intensities of the sample annealed at 900 °C for 1 h compared with calculated values of Si and Ge (b)	25
Figure 4.12 The relative concentration of Ge, Si, O, and C with sputtering time in as-grown samples with $P_{Ge} = 5$ (a), 10 (b), and 20 W (c).	27
Figure 4.13 The x-ray diffraction geometry.	28
Figure 4.14 Annealing temperature evolution of the XRD spectra corresponding to the (111) diffraction in the samples with $P_{Ge}=20$ W and annealed for 1 h.	32
Figure 4.15 Annealing time evolution of the XRD spectra corresponding to the (111) (a), and to the (220) and (311) (b) diffractions in the samples with $P_{Ge}=20$ W annealed at 1100 °C.	32
Figure 4.16 Evolution of the XRD spectra corresponding to the (111) diffraction in the samples with different $P_{Ge}=0, 5, 10,$ and 20 W annealed at 1100 °C for 1 h.	33
Figure 4.17 Annealing temperature (a) and annealing time (b) evolution of the XRD spectra corresponding to the (111) diffraction in the samples with $P_{Ge}=0$ W (Si nanocrystals).	34
Figure 5.1 Cross-sectional TEM image of the sample annealed at 1100 °C for 1 h (a) and 3 h (b).	43
Figure 5.2 Size distribution of the nanocrystals in the sample annealed for 1 h (a) and 3 h (b). Insets show the selected area diffraction patterns.	44

Figure 5.3 XRD pattern of the as grown and the samples annealed at different times in the 2θ interval of $24 - 31^\circ$ corresponding to (111) planes (a), and $44 - 56^\circ$ corresponding to (220) and (311) planes (b), and the decomposition of the (111) diffraction peak of the sample annealed for 3 h (c).	46
Figure 5.4 Raman spectra of the samples annealed at 1100°C for 1 h (a), 3 h (b), and decomposed peaks of the Si-Ge vibration mode of the sample annealed at 1100°C for 3 h (c).	48
Figure 6.1 Room temperature PL spectra of the Si nanocrystals.	54
Figure 6.2 X-ray diffraction spectra of the Si nanocrystals.	56
Figure 6.3 Decomposed PL spectra of the samples annealed at 900, 1000, and 1100°C for 1 h (a-c) respectively.	58
Figure 6.4 Decomposed PL spectra of the samples annealed at 1100°C for 1, 3, and 5 h (a-c) respectively.	63
Figure 6.5 Temperature dependent PL spectra of the sample annealed at 1000°C for 1 h.	64
Figure 6.6 Integrated intensity of peak <i>Q</i> , peak <i>I</i> and peak <i>A</i> as a function of temperature and the ratio of peak <i>Q</i> / peak <i>I</i>	65
Figure 6.7 Temperature dependent evolution of the peak position of peak <i>Q</i> , peak <i>I</i> , peak <i>A</i> , and whole peak.	67
Figure 6.8 Effect of annealing treatments on the FTIR spectra of the co-sputtered $\text{SiO}_2/\text{Si}:\text{SiO}_2/\text{SiO}_2$ samples.	70
Figure 6.9 Comparison between FTIR spectra of the SiO_2 -sputtered and co-sputtered $\text{SiO}_2/\text{Si}:\text{SiO}_2/\text{SiO}_2$ samples under the same annealing treatments.	72
Figure 6.10 Temperature dependent PL spectra of the sample annealed at 900°C for 1 h.	75
Figure 6.11 Temperature dependent PL spectra of the sample annealed at 1100°C for 1 h.	76
Figure 6.12 Temperature dependent PL spectra of the sample annealed at 1100°C for 5 h.	76
Figure 7.1 Annealing treatment evolution of room temperature PL spectra of the samples with $P_{Ge} = 0\text{ W}$ (Si nanocrystals).	81

Figure 7.2 Decomposed PL spectra of the samples with $P_{Ge} = 0$ W (Si nanocrystals) annealed at 900, 1000, and 1100 °C for 1 h (a-c), and annealed at 1100 °C for 1, 3, and 5 h (d-f).	82
Figure 7.3 Annealing treatment evolution of room temperature PL spectra of the samples with $P_{Ge} = 10$ W.	83
Figure 7.4 Decomposed PL spectra of the samples with $P_{Ge} = 10$ W annealed at 900, 1000, and 1100 °C for 1 h (a-c), and annealed at 1100 °C for 1, 3, and 5 h (d-f).	84
Figure 7.5 Annealing treatment evolution of FTIR spectra of the samples with $P_{Ge} = 10$ W.	85
Figure 7.6 PL spectra of the samples with $P_{Ge} = 0, 5, 10,$ and 20 W annealed at 1100 °C for 5 h.	86
Figure 7.7 FTIR spectra of the samples with $P_{Ge} = 0, 5, 10,$ and 20 W annealed at 1100 °C for 5 h.	86
Figure 7.8 Decomposed PL spectra of the samples with $P_{Ge} = 0$ (a), 5 (b), 10 (c), and 20 W (d) annealed at 1100 °C for 5 h.	87

CHAPTER 1

INTRODUCTION

In recent years, nanometer size Si and Ge crystals have been extensively studied because they offer new possibilities for indirect band gap semiconductors for optoelectronic applications. It has been demonstrated that the photoluminescence (PL) energy of noncrystalline Si is tunable from the band gap of bulk Si to the visible region by simply controlling the size. The tuning range can be expanded by $\text{Si}_{1-x}\text{Ge}_x$ alloy formation. So, alloy $\text{Si}_{1-x}\text{Ge}_x$ nanocrystals provide an advantage of fine tuning the electronic band structure which plays a detrimental role in the charging/discharging, and retention properties of the memory element. In order to fabricate high performance devices with $\text{Si}_{1-x}\text{Ge}_x$ nanocrystals, it is necessary to know and control their structural and optical properties which depend on several factors, including particle size, shape, surface condition, atomic composition, and compositional uniformity. These factors are very sensitive to the preparation parameters and post annealing treatments.

In this work we have prepared Si and $\text{Si}_{1-x}\text{Ge}_x$ nanocrystals by rf magnetron co-sputtering method. The effect of annealing parameters and Ge content of x on the structural and optical properties sandwiched $\text{SiO}_2/\text{SiO}_2$: Si: Ge/ SiO_2 nanostructures have been investigated. The formation and evolution of $\text{Si}_{1-x}\text{Ge}_x$ nanostructures and their average size, distribution, and crystallinity were studied by cross-sectional high-resolution electron microscope (HREM). The average sizes, composition, compressive stress, and root-mean-strain have been obtained by analyzing the data from X-ray diffraction (XRD) spectra. Raman spectroscopy being a powerful and non-destructive technique in the analysis of solid chemical structures has been performed to monitor

the compositional evolution of the samples as well. To identify structural damage to the SiO₂ matrix caused by sputtering and its evolution with Ge content and annealing treatments, Fourier transform infrared (FTIR) spectroscopy has been applied. In addition to the valuable information about the structural change and stoichiometry of the matrix it provides information related to the defect characteristics connected with the PL spectra. A wide range of important sample properties, such as electronic band structure, radiative and nonradiative carrier recombination processes, electron-photon coupling and the nature of defect and impurity centers, can be studied by PL. In addition to the basic PL technique the temperature dependent PL (TDPL) were utilized to investigate processes such as the thermally activated transport of carriers, the thermal population of electronic excited states, the quantum confined versus interface related radiative recombination of carriers.

The outline of the thesis is as follows: Chapter 2 reviews the fundamental aspects of this work. Physical properties and electronic Band Structures of the Si, Ge and Si_{1-x}Ge_x bulk crystals are briefly reviewed. General aspects of the quantum confined systems and the resulting features including blueshift of the emitted energy and the high emission efficiency are discussed. Furthermore, the quantum confined effects in Si and Ge nanostructures and a comparison between them have been introduced. Chapter 3 presents a brief review of the synthesis methods together with what was used within the framework of this thesis. Details about the sample preparation and growth can be found here. Chapter 4 refers to brief review of the the employed structural characterization techniques and obtained results. Those comprise TEM, XPS, XRD, Raman spectroscopy, and FTIR measurements. Chapter 5 is devoted to the special concept of core-shell observation in Si_{1-x}Ge_x nanocrystals with higher germanium content of $x = 0.69$ during prolong annealing at higher temperature of 1100 °C. This process has been evidenced by a double peak formation in the XRD and Raman spectra. We attributed this phase separation to the differences in atomic size, surface energy, and surface diffusion disparity between Si and Ge atoms leading to the formation of nonhomogenous structure consist of a Si-rich SiGe core covered by a Ge-rich SiGe shell.

Chapter 6 is related to the optical properties of the Si nanocrystals in weak quantum confined regime. Origin and evolution of the PL spectra are discussed in the light of XRD, FTIR, and TDPL measurements. It has been found that for all the samples PL peaks tend to decompose to four Gaussian peaks originating from radiative defects in SiO₂ matrix, *nc*-Si/SiO₂ interface related localized defects, localized states in the amorphous Si band gap and quantum confinement of excitons in smaller nanocrystals. Considering the observation of intense luminescence and its decomposition tendency in nanocrystals with average sizes larger than exciton's Bohr radius the necessity to distinguish between the role of smaller and larger nanocrystals in the PL mechanisms has been discussed. Furthermore, possible origin of the interface related localized states in particular Si=O double bonds in the *nc*-Si/SiO₂ interface have been discussed. Chapter 7 refers to optical properties of the Si_{1-x}Ge_x nanocrystals in a weak quantum confined regime with average sizes larger than the Bohr radius of excitons in Si and with a larger range Ge content of *x* between 0-0.85. Origin and evolution of the PL spectra, in a similar manner to that of Si nanocrystals, are discussed in the light of XRD, FTIR, and TDPL measurements. Influence of the Ge incorporation on the quantum confined related and interface related recombination has been discussed.

CHAPTER 2

PHYSICAL AND ELECTRONIC PROPERTIES OF BULK Si, Ge, AND Si_{1-x}Ge_x AND THE SIZE ISSUE

2.1 Motivation

2.1.1 Physical Properties of Si, Ge, and Si_{1-x}Ge_x

Silicon and germanium single crystals belong to the cubic class of crystals (figure 2.1). They crystallize in the diamond structure that consists of two face-centered cubic (fcc) crystal lattices that coincide if translated by a vector of $(1/4 \ 1/4 \ 1/4)$ along the diagonal of the unit cell. The coordination number for an atom in the diamond lattice is four, *i.e.* each substitutional silicon lattice atom is surrounded by four others in a tetrahedral configuration. The lattice constant of single crystalline undoped silicon is approximately $a_{Si} = 5.431 \text{ \AA}$ at room temperature [1], while that for germanium is between $a_{Ge} = 5.6573$ [2] and 5.6579 \AA [3]. For Si_{1-x}Ge_x alloy crystals to first order, the lattice constant varies linearly from that of silicon to that of germanium by increasing x , based on linear interpolation between a_{Si} and a_{Ge} , can be estimated as follows:

$$a_{SiGe}(x) = (a_{Ge} - a_{Si})x + a_{Si}. \quad (2.1)$$

However the best fit for the cubic lattice constant is obtained with a parabolic interpolation [4, 5]:

$$a_{Si_{1-x}Ge_x}(x) = 5.431 + 0.1992x + 0.002733x^2. \quad (2.2)$$

Silicon has a density of 2.329 g/cm^3 and that of germanium is 5.323 g/cm^3 and melting points are 1412 and $940 \text{ }^\circ\text{C}$, respectively [6].

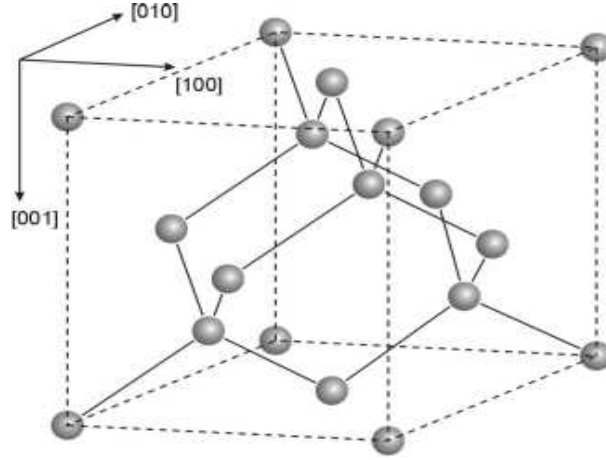


Figure 2.1: The diamond lattice structure of silicon and germanium.

2.1.2 Band Structure of Si, Ge, and $\text{Si}_{1-x}\text{Ge}_x$

Silicon and germanium belong to group IV of the periodic table. Both have an indirect band gap, *i.e.* the valence band maximum and conduction band minimum are located at different momentum vectors in the Brillouin zone. Figures 2.2 (a, and b) shows the band structures of the silicon and germanium bulk crystals in the reduced Brillouin zone scheme [7]. The respective valence band maxima are at the Γ point. The conduction band minima of silicon are near the X points along the $\langle 100 \rangle$ directions. In contrast, the conduction band minima in germanium are located at the L points in the $\langle 111 \rangle$ crystal directions. The silicon conduction band is therefore sixfold degenerate, whereas the germanium conduction band is fourfold degenerate. The valence band is twofold degenerate in both cases. The fundamental band gap is given by the energy difference between the valence band maxima and the conduction band minima. The indirect band gap is 1.17 eV at 0 K [8] (1.11 eV at 300 K) for silicon and 0.74 eV at 1.5 K [9] (0.66 eV at 300 K) for germanium, respectively. The $\text{Si}_{1-x}\text{Ge}_x$ material system is an alloy system with outstanding properties. It forms an ideal random alloy, *i.e.* Si and Ge are miscible in arbitrary proportions in the solid

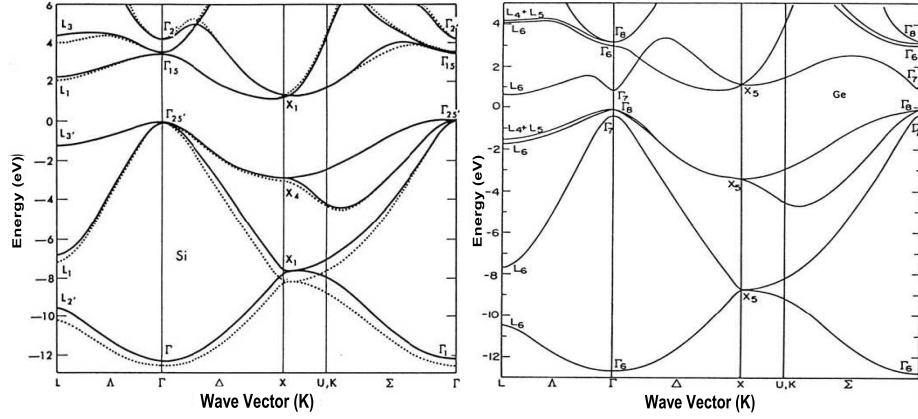


Figure 2.2: Band structures of silicon and germanium. In the case of silicon two results are presented: nonlocal pseudopotential (solid line) and local pseudopotential (dashed line) [7].

phase. On the one hand, the structural and chemical properties are similar enough to use in well-established standard Si process technology. On the other hand, they are different enough to provide selective structuring. In $\text{Si}_{1-x}\text{Ge}_x$ alloys, the fundamental band gap can be tuned with the Ge content in the mixture [10]. In $\text{Si}_{1-x}\text{Ge}_x$ bulk crystals, the original character of the silicon conduction band with the minima along the X direction is maintained up to $x = 0.84$. From $x = 0.84$ on, the conduction band minima are germanium-like and the minima are at the L points. The calculated band-gap energy of the alloy is plotted as a function of the Ge mole fraction x in figure 2.3 and compared with luminescence data [11]. The lattice parameter of the alloy (computed from the valence force field) is also plotted in the inset and matches Dismukes's law (solid line) [4].

2.2 Quantum Confinement Effect

The effect of confinement in a quantum mechanical system can be understood by considering the simple particle in a box problem, in which we solve for the wavefunctions (eigenstates) and energies (eigenvalues) of an infinite potential well using Schrodinger's wave equation. We can improve our approximation of a quantum dot by considering the particles of interest, excitons, in a three-dimensional, finite, spherical confinement potential representing the insulating matrix around the semiconduc-

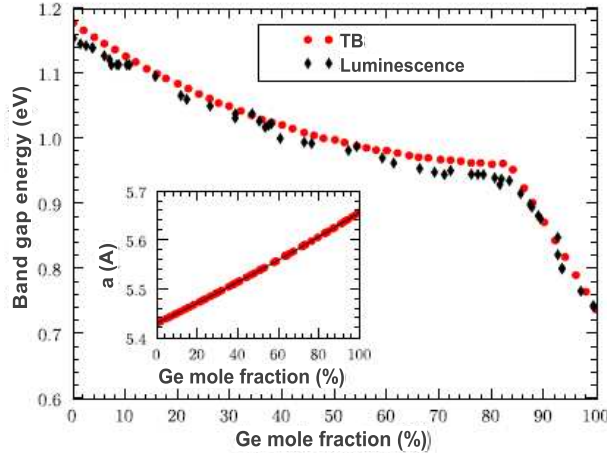


Figure 2.3: Band-gap energy of random bulk $\text{Si}_{1-x}\text{Ge}_x$ alloys as a function of the Ge mole fraction x . Inset: lattice parameter of the alloy. The solid line is Dismukes's law [10].

tor nanocrystal. Excitons are electron-hole composite states that are coupled together by Coulomb attraction. The mathematics used to describe an exciton is identical to the model of hydrogen atom. Therefore a Bohr radius for the ground state of the exciton corresponds to the critical length scale for confinement effects. In terms of the electron and the hole that comprise the exciton, the Bohr radius can be thought of as the typical separation distance. In silicon, the exciton Bohr radius is about 4.9 nm , a fairly small number among semiconductor quantum dots because of the relatively large effective mass of the charge carriers in silicon. This tells us that we can expect to observe quantum confinement effects in silicon nanocrystals that are smaller than approximately 5 nm in diameter.

By considering the particle in a box problem, the energy of the ground state exciton increases with increasing confinement. In fact, within the simple effective-mass approximation and assuming an infinite potential barrier the size-dependent effective bandgap varies according to:

$$E_{gap} = E_{gap}^{Si} + \frac{\pi^2 \hbar^2}{2\mu L^2} \quad (2.3)$$

where E_{gap} is the nc -Si bandgap, E_{gap}^{Si} is the silicon bandgap, μ the electron-hole reduced mass and L the diameter of the nc -Si. Thus, the optical gap for a quantum dot increases as its size decreases. In addition, when the e-h wavefunctions are squeezed

in real space they broaden in the momentum space, which causes a larger overlap of the e-h wavefunctions increasing the radiative recombination probability (quasidirect transitions) [12]. In fact, typical lifetimes of Si-nc are in the μs range, while those of bulk Si in the $msec$ range. Moreover, high emission efficiency is also a consequence of two additional facts: i) the spatial constrictions of e-h pairs in nc -Si, which are no longer free to diffuse as in bulk silicon; thus the probability to find nonradiative recombination centers is reduced significantly; ii) the decrease of the average refractive index of the material, which is an average between those of Si and of SiO_2 weighted on the Si content; this increases the light extraction efficiency from the material itself by reducing the internal reflections. As a result of all these factors, the typical internal quantum efficiency of nc -Si is larger than a few per cent and in the best samples reaches maximum values of 60 [13].

It is worth noting that power dependency of L is rather L^{-x} with $1 < x < 1.5$ or an even weaker in some cases. Such behavior has been a reason for supposing a key role for interface states in the radiative recombination process [14]. The question about the origin of the radiative electron-hole transitions in the nanocrystals remains under extensive debate even today. On the other hand, nanocrystal-nanocrystal interactions can play an important role in the emission spectrum. Furthermore, silicon oxygen double bond defect states at the surface of the nanocrystal can capture and localize the exciton [15-17].

In comparison with electronic properties of Si, Ge has a larger dielectric constant and smaller effective masses for electrons and holes, and the energy difference between the indirect gap and the direct gap is smaller. Thus, Ge nanostructures exhibit more prominent quantum size effects than Si nanostructures [18,19]. The Bohr exciton radius is larger in Ge (24.3 nm) than in Si (4.9 nm): this increases the oscillator strength of the indirect transitions, which enhances the magnitude of lattice vibration and causes a larger deformation of the crystal lattice to minimize the excitonic energy. As a result, stronger electron-phonon coupling is found in Ge nanocrystal. These electronic conditions lead to an expectation that it is much easier to change the electronic structure around the band gap of Ge.

CHAPTER 3

SYNTHESIS OF Si, AND $\text{Si}_{1-x}\text{Ge}_x$ NANOCRYSTALS IN SiO_2 MATRIX BY RF MAGNETRON CO-SPUTTERING: EXPERIMENTAL PROCEDURES

3.1 A Brief Review of the Preparation Methods

In this section we briefly review some of the most popular techniques to synthesize light emitting nanostructures. The simplest and the least expensive method is based on porous silicon (p -Si), which is fabricated by electrochemical etching of crystalline silicon substrates using hydrofluoric acid (HF) based solutions [20]. The specific conditions to obtain light emitting p -Si are reviewed in detail in references [21, 22]. Light emitting p -Si has a random, nanometric sponge-like structure with a fairly large surface area that can easily be accessed and chemically modified due to its porous characteristics. While this property of p -Si is of great advantage for certain applications, such as chemical [23, 24] and bio-chemical sensing [25, 26], it represents a major limitation for a consistent study of quantum size effects as the size, shape and even the dimensionality of the nanocrystalline silicon objects are not well defined and can vary between samples and preparation techniques. Furthermore, as the p -Si matrix may contain various species such as SiO_x , amorphous silicon (a -Si) and other amorphous derivatives of silicon, the exact surface termination of the nanocrystalline silicon objects cannot accurately be determined. Aging effects can be quite significant in p -Si and may affect both optical properties and transport phenomena.

The first experimental report on room-temperature PL from silicon nanostructures

other than *p*-Si, is related to silicon nanocrystals (*nc*-Si) fabricated by ion implantation of silicon into SiO₂ matrix [27]. Recently after, other methods to produce *nc*-Si embedded in SiO₂ matrices emerged, including chemical vapor deposition (CVD) [28] of sub-stoichiometric oxide (SiO_{*x*}), RF magnetron sputtering [29], reactive evaporation [30] and plasma enhanced CVD (PECVD) [31-33]. In principle, all these methods require high temperature annealing of the deposited films to produce phase separation of the excess silicon from the SiO₂ matrix followed by crystallization of the silicon into nanocrystalline particles. The ion implantation method [34-36] is quite popular due to its compatibility with the standard silicon CMOS technology (where it is routinely used to create doped silicon regions). In this technique silicon ions are extracted from the plasma, accelerated toward the SiO₂ substrate by an electric field and losing their energy after traveling a given depth in the substrate. The thickness and the profile of the implanted layer depend mainly on the implantation dose and the ion energy. In principle, the lower the ion energy the narrower the implanted zone, however, implantation dose also decreases at lower ion energies.

Another elegant method to produce continuous size variation of *nc*-Si in a single deposition run is the laser pyrolysis of silane in a gas flow reactor, which has been reported by Ledoux *et al.* [37]. In this technique a pulsed CO₂ laser produces a molecular beam of silicon nanoparticles having a size distribution of 3-7 *nm* with the larger nanoparticles moving slower than the smaller ones. Using a rotating mechanical chopper synchronized with the laser pulses, size selected nanoparticles are transmitted and deposited at different locations across the substrate. A slightly narrower size distribution but a much better control of the position and the density of *nc*-Si has been achieved by synthesizing Si/SiO₂ superlattices. This method has been introduced by Lockwood *et al.* [38] who have used silicon molecular beam epitaxy (MBE) system combined with ex-situ UV ozone oxidation for growing alternating nanolayers of amorphous silicon and SiO₂. A similar approach, based on depositing alternating SiO_{*x*}/SiO₂ layers with $1 < x < 2$, has also been introduced where phase separation during annealing gives rise to a formation of *a*-Si aggregates that later on crystallize to create *nc*-Si [39]. In this method, individual layers are deposited one on top of the other at deposition rates of about 2-4 *nm/min* to achieve a good thickness

control.

3.2 Synthesis of Si and Si_{1-x}Ge_x Nanocrystals by rf Magnetron Co-sputtering Method

A similar result of forming oxide layers with excess silicon concentration has been obtained by rf magnetron sputtering. The sputtering process (sometime referred as physical vapor deposition) involves a bombardment of silicon and SiO₂ solid targets by energetic ions (usually argon ions), removing atoms and molecules from the targets that are deposited on the substrate. As silicon dioxide is an electric insulator, an rf electric field is used to create the plasma between the substrate and the targets. A popular method to produce *nc*-Si is the co-sputtering technique [40, 41] in which, the two targets (usually pure silicon and quartz) are simultaneously exposed to the ions, producing a mixed layer of silicon and oxide with the excess silicon being used to create *nc*-Si after high temperature annealing.

Capacitive coupled sputtering is the most commonly used sputtering arrangement [42]. In this system target is cathode and substrate is anode facing to the cathode (figure 3.1). Variable dc / rf (most commonly 13.56 MHz) power supply is used to accelerate the ions toward the target. In the rf case blocking capacitor and matching network is necessary to develop dc self bias and optimize power transfer from rf supply to the plasma. The rf sputtering has advantageous of having high deposition rates, sputtering of insulating targets, low power and low pressure operation conditions. In some configurations substrate is also negatively biased to clean the substrate surface before deposition. The substrate may be heated or cooled depending on configuration but cathode must be cooled during sputtering. Substrate moves relative to target in some configurations in order to get better film uniformity or to prepare complex film. Turbo molecular, diffusion or sublimation pumps are used to reach low base pressure before sputtering. Inlet gas or gas mixtures introduced to the chamber by gas flow controllers. Process gas pressure ranges from a few millitorr to few hundred millitorrs. Plasma is sustained by secondary electron ejection from cathode and impact

ionization of neutral gas atoms.

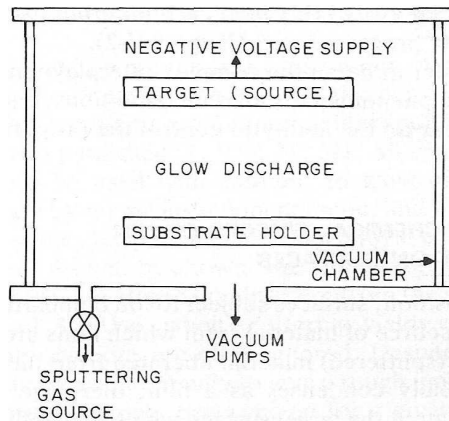


Figure 3.1: Schematic diagram of capacitive coupled sputtering system [42].

If a sample is placed on view of the sputtered face of target in vacuum then sputtered atoms condense on the sample. This is still an effective way of thin film deposition technique used in integrated circuit technology [43]. A simple schematic of setup is shown at figure 3.1. The easiness of film thickness control, availability of various sputtering targets materials, deposition without compositional changes and mass production compatibility make the sputter deposition powerful thin film deposition technique in IC technology. High temperature melting point targets can be easily deposited by sputter deposition. On the other hand, slow deposition rates compared to thermal evaporation techniques is the main disadvantage of sputtering. Reactive sputtering is an attractive way to form desired compound on elemental target surface and deposition it to the substrate. In some cases it is used to reinforce the deficient constituent of composite target at the deposited film. Varying ratios of oxide, nitride, sulfide and carbide gases are mixed with noble gas for reactive sputtering.

Particle flux, substrate to target distance and view angle are important parameters of deposition. Substrate should be as close as possible to target since deposition rate increases with decreasing distance but not enter to plasma region. Typically substrate is located 5-7 cm above the target. Substrate should be placed parallel to target and their axes should coincide to get uniform films. Usually, in order to improve uniformity, the substrate is rotated and placed far enough from the targets. In certain

cases however, particularly when size-dependent phenomena are to be investigated, it is desirable to put the substrate nearby the targets without rotation. In this case, the excess silicon concentration along the deposited film continuously varies from one edge of the substrate to the other edge [44]. The thickness and the amount of excess silicon concentration are determined by the rf power as well as by the geometry of the sputtering chamber.

On the other hand, sputtering gas pressure affects the deposition rate. Deposition rate makes a maximum with increasing gas pressure at constant power. Low efficiency in the ion collection of cathode at low pressure and increasing scattering of sputtered atoms with gas ions at high pressure reduce deposition rate. Sputtering is carried out at gas pressure giving the maximum deposition rate. Desired gas pressure can be controlled either throttling gas inlet or chamber pumping speed. Chamber pumping speed can be controlled by throttling pump inlet or pump speed. Heating of the target materials is an important issue, that should be considered. During bombardment of target over 95 percent of ion energy is transformed as heat. Therefore target material must be cooled to stay at sputtering regime. Maximum power flux is the limiting factor in both dc and rf magnetron sputtering since exceeding this power results in cracking of target. Thermal conductivity of target and back plate play important roles in cooling rate of target.

Magnetic field is added to sputtering systems to increase deposition rate. Magnetic field is used to sustain and increase the ion density in the plasma by trapping electrons near target surface. Hence low pressure sputtering (up to 10^{-5} torr) with high deposition rate can be performed. Permanent magnets or electromagnets are used at different geometries to obtain uniform magnetic fields parallel to the target's surface and perpendicular to electric field so electrons follow circular and spiral path [42].

nano-D 100 is a multi target capacitive coupled dc and rf magnetron sputtering system manufactured by Vaksis ltd. (see figures 3.2 and 3.3). Complex structures and compounds can be prepared using three 3 inch circular magnetrons installed. One of the magnetrons is connected to 600 W 13.56 MHz rf supply other two are 500 W and 1 kW dc supplies; hence various conductors and insulator can be co-sputtered.

Up to 2 inch substrates can be mounted on circular rotating substrate holder. Target to substrate distance and angle is adjustable. Base pressure up to 10^{-7} torr can be achieved with installed Turbo Molecular Pump (TMP). Argon is used for sputtering gas and reactive sputtering can be performed with three channel controlled gas inlet. High purity oxygen and nitrogen gases are installed to the system. Substrate can be heated before or during deposition via infrared heater from the back side up to 1000 °C. Deposited film thickness is monitored with a crystal oscillator.

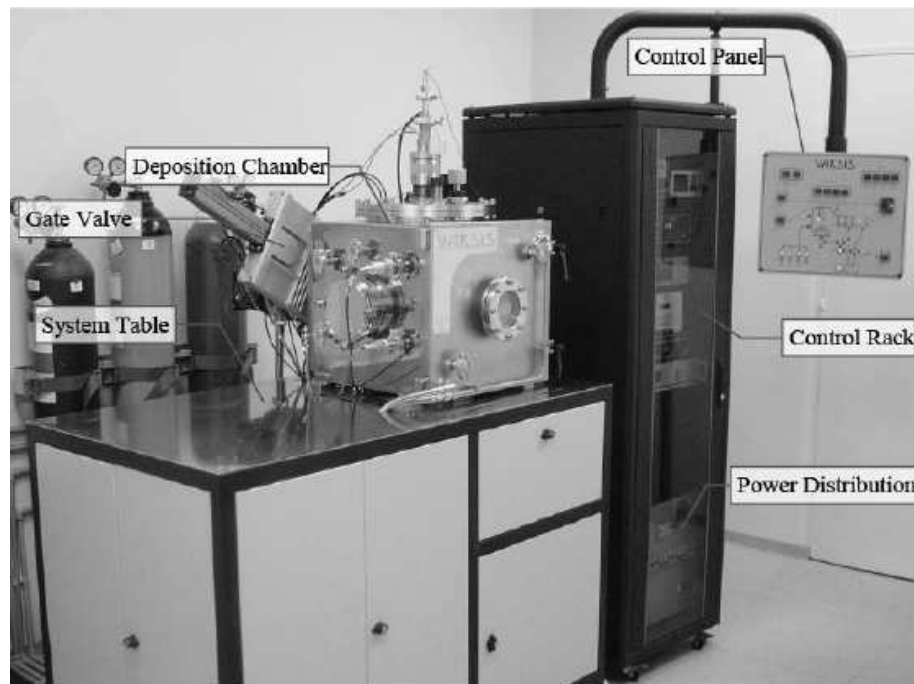


Figure 3.2: The nano-D 100 sputtering system.

3.2.1 Sputtering Parameters

Si and $\text{Si}_{1-x}\text{Ge}_x$ alloy nanocrystals embedded in SiO_2 matrices were prepared by a rf co-sputtering method. The substrates were *n*-type Si $< 100 >$ with the resistivity of 5-10 Ωcm . A whole 3-in. substrate was cleaved into several 4 cm \times 4 cm pieces, which were used for subsequent processing. After degreasing and dipping in a dilute HF solution, the Si substrate was loaded into the sputtering chamber.

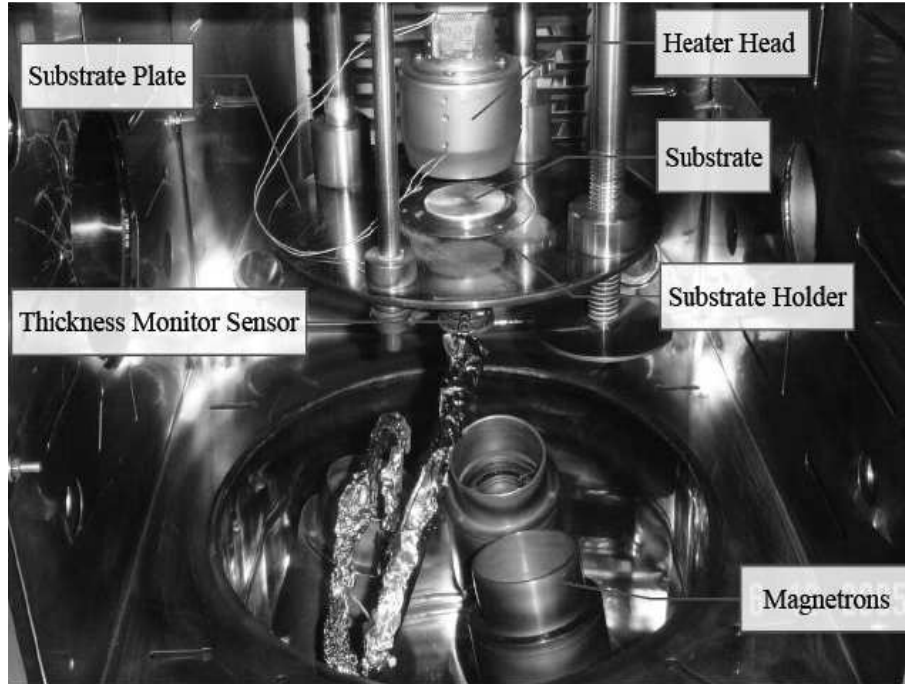


Figure 3.3: The sputtering chamber.

Si, Ge and SiO₂ sputtering targets were simultaneously sputtered in Ar gas with a flow rate of 50.0 *sccm*. The base pressure of the sputtering chamber was 1.5×10^{-6} . Before sputtering the samples were heated at 500 °C for 30 *min* under vacuum in the sputtering chamber in order to remove residual contamination and water molecules at its surface. The pressure during the sputtering process was kept at 3 *mTorr* by controlling the conductance with the gate valve between the chamber and the pumping system. The deposition rates can be controlled separately by changing the power and the distance between the substrate and the target. In this work, those of Si and SiO₂ were fixed (100 W and 350 W, respectively) and that of Ge was varied to control the Ge content of x in the films. We have synthesized SiO₂/SiO₂: Si: Ge/SiO₂ sandwich films to understand the influence of the annealing time, annealing temperature, and Ge content of x on the structural and optical properties of *nc*-Si and *nc*-Si_{1-x}Ge_x embedded in SiO₂ matrices. The bottom SiO₂ layer with the thickness of about 40 *nm* was deposited on Si to restrain Ge atoms from growing epitaxially on the Si substrate in the post-annealing process. The top SiO₂ layer with the thickness of about 40 *nm* was deposited to impede the diffusion of Ge atoms out of the surface. The typical

deposition rate was 4 nm/min , and the thickness of the films was about 350 nm .

3.2.2 Annealing Treatments

After growth, wafers were cleaved and annealed in a quartz tube furnace under flowing N_2 gas at ambient pressure for times (t) varying between 1-5 h and temperatures (T) of 900, 1000, and 1100 $^\circ\text{C}$. Each sample was annealed only once at a specific T and a certain t , *i.e.*, no cumulative annealing experiments were performed. In general, the formation mechanism for Si and $\text{Si}_{1-x}\text{Ge}_x$ nanocrystals embedded in SiO_2 matrix goes through the familiar sequence of nucleation and growth, often followed by coarsening of nanocrystals due to Ostwald ripening. Structural characterization including, formation, evolution, relative concentration, and Ge content of x of the nanostructures were studied by cross-sectional high-resolution TEM, XRD, XPS, Raman spectroscopy, and FTIR measurements. For optical characterization PL and TDPL measurements have been used.

CHAPTER 4

STRUCTURAL CHARACTERIZATION OF THE Si AND $\text{Si}_{1-x}\text{Ge}_x$ NANOCRYSTALS EMBEDDED IN SiO_2 MATRIX

4.1 Transmission Electron Microscopy (TEM)

The TEM technique has been used to obtain detailed information on the internal structure of nanostructures. Direct images of the structural elements can be obtained with resolutions down to the atomic scale. To apply this method of analysis, a high energy beam of electrons is fired in vacuo through a thin, electron-transparent region of the sample of interest [45, 46]. An image of the sample is impressed into the transmitted electron beam and is magnified by subsequent electromagnetic lenses. The image, with a magnification of up to or beyond a million times, is finally displayed on a fluorescent screen (for recording on photographic film) or on a computer monitor using an appropriate pick-up system.

The way in which the preparation of thin specimens is carried out for TEM often controls the quality of the final data obtained. A common approach to thinning relies upon removal of unwanted regions of a sample by low voltage Ar^+ ion milling in order to isolate the material to be studied in a foil approximately 1-100 *nm* in thickness. This process can be carried out to provide specimens in either plan-view or cross-sectional configuration, depending upon the type of observations to be made. The versatility of the TEM imaging method is very great, since a range of contrast mechanisms can be exploited. Depending upon the orientation of the specimen under the electron beam, image features can be related directly to the local thickness of material or to phase-

or diffraction-contrast imaging processes, each of which gives its own unique structural information [45]. Crystallographic defects which may be present can be imaged using diffraction contrast, while the atomic lattice itself is revealed by high resolution phase-contrast work.

4.1.1 Experimental Results

To acquire more information about the film crystallinity, $nc\text{-Si}_{1-x}\text{Ge}_x/\text{SiO}_2$ interface, SiO_2/Si substrate interface and mean diameter of the nanocrystalline region, cross-sectional high-resolution electron microscope [JEOL2010F] analysis was performed on the samples, which have been carried out at the University of Oslo. TEM samples were prepared as cross section specimens by gluing two substrates with film sides facing each other. The samples were then cut and mechanically thinned until $50\ \mu\text{m}$ thickness. The samples were further thinned using a GATAN 691 ion miller. $5\ \text{KeV}$ Ar^+ ion beams were directed from an angle of 5° below and 7° above until electron transparency.

In general, all the samples have three layers. The bottom layer, closest to the Si monocrystalline substrate consist of amorphous SiO_2 . The next layer is several hundred nanometers thick and consists of amorphous SiO_2 containing nanocrystals. The uppermost layer is amorphous SiO_2 layer containing no particles. Figures 4.1 (a-c) show the cross-sectional TEM image of the samples with the same $P_{\text{Ge}} = 20\ \text{W}$ annealed at different temperatures of 900 , 1000 , and $1100\ ^\circ\text{C}$ for $1\ \text{h}$, respectively.

For the sample annealed at $900\ ^\circ\text{C}$ there seem to be some lines across the film inclined $4\text{-}6^\circ$ to the normal of the film/substrate interface. These directions of the lines seem to be uniform across the film. The high resolution TEM (figure 4.2) indicates that the Si/Ge particles form these lines and that there is a tendency for the particles to grow on top of each other in a direction perpendicular to the film / substrate interface. The average size of the crystallites is about $5\ \text{nm}$ and large crystallites can reach the size of $10\ \text{nm}$ (figure 4.3 (a)). The film just started to be crystallized and crystal planes are observable as evident from selected area diffraction pattern (SAD) (figure

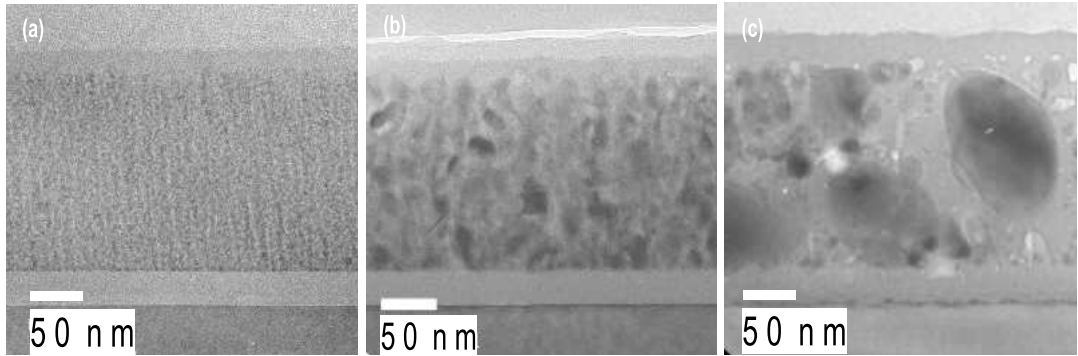


Figure 4.1: Cross-sectional TEM image of the samples annealed at 900 (a), 1000 (b), and 1100 °C (c) for 1 *h*.

4.4 (a)). This diffraction pattern shows continuous and complete rings which can be indexed as crystallographic planes of SiGe. Complete rings indicate that most part of the SiGe film remains amorphous. The other feature is that the interface between the amorphous SiO₂ layer and SiGe layer is very sharp and smooth.

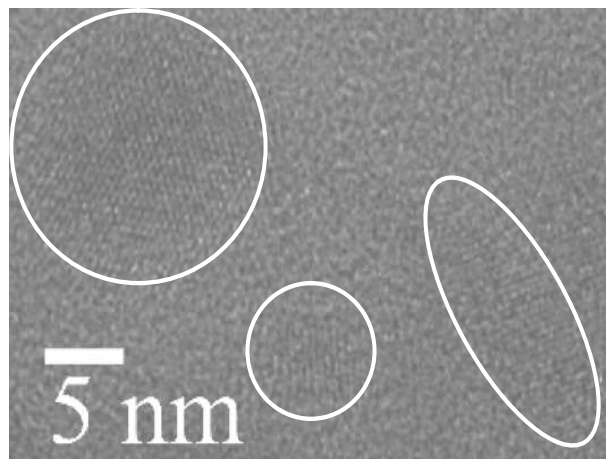


Figure 4.2: High resolution cross-sectional TEM image of the samples annealed at 900 °C for 1 *h*.

The cross-sectional TEM image of the sample annealed at 1000 °C shows that the grain size of the crystallites increases by increasing annealing temperature (figure 4.1 (b)), and, as evident from SAD pattern (figure 4.4 (b)), distinctive spots forming complete or incomplete rings illustrates the progress of crystallization. We see a combination of crystallized and amorphous SiGe clusters. The tendency for particles to grow on top of each other in a direction perpendicular to the film / substrate in-

interface decreases by increasing the annealing temperature. Also there is a distinctive layer between the amorphous SiO₂ layer and Si substrate, which is supposed to be caused by Ge diffusion. Comparing with the sample annealed at 900 °C, the interface between the SiO₂ and SiGe layers is no more smooth. The average sizes of the crystallites are 16 nm, and as can be seen from figure 4.3 (b) the density of crystallites is not uniform.

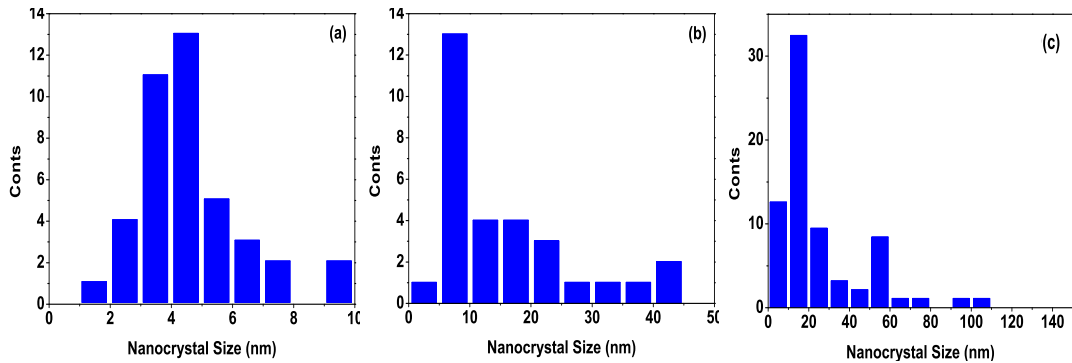


Figure 4.3: Size distribution of the nanocrystals in the sample annealed at 900 (a), 1000 (b), and 1100 °C (c) for 1 h.

For the sample annealed at 1100 °C for 1 h the cross-sectional TEM (figure 4.1 (c)) shows that the grain size of the crystallite increases, and as can be seen from SAD pattern, most of the SiGe film has been crystallized (figure 4.4 (c)). The average size of the crystallites is 22 nm and it varies from 5-110 nm (figure 4.3 (c)). It was observed that the properties of these nanostructures are sensitive to annealing treatments. By increasing annealing temperature the average size of the nanocrystals increases and their crystallinity have been enhanced. The other feature is preference of small size SiGe crystallites to lie in a row between the interface of SiGe layer and amorphous SiO₂ When the same sample is annealed at 1000 °C or above for 1 h.

The SiO₂ layer between the co-sputtered layer and the substrate does not appear to contain Ge and/or SiGe nanocrystals. This is an expected feature for this annealing treatment, the concentrations in this SiO₂ layer will be less than the solid solubility so there is no driving force for segregation except perhaps during the cooling down process, but since there already exist segregation sites within a short diffusion distance the concentration can be kept close to equilibrium during a large portion of the cooling

down process. So, comparing with the TEM image of the samples annealed at 900 and 1000 °C for 1 h, thickness of the upper and bottom SiO₂ layers is slightly decreased and the interface between the SiO₂ and SiGe layers is no longer flat.

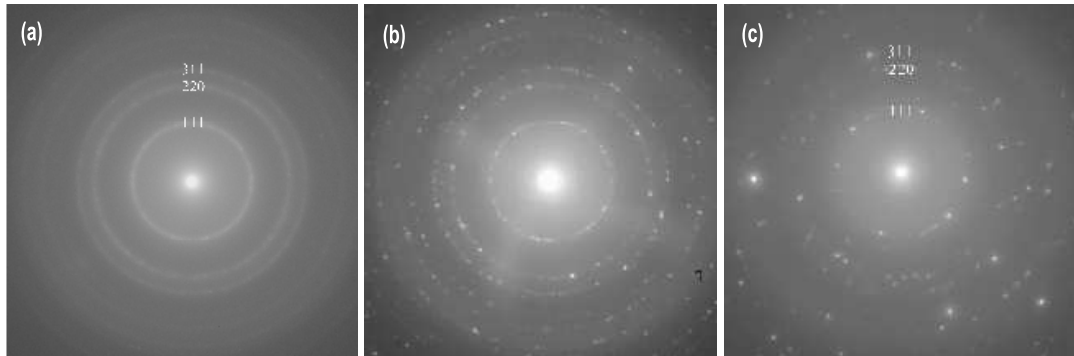


Figure 4.4: Selected area diffraction patterns of the samples annealed at 900 (a), 1000 (b), and 1100 °C (c) for 1 h.

Figures 4.5 (a-c) indicate the cross-sectional TEM image of the samples with the same $P_{Ge} = 20$ W annealed at 1100 °C for 1, 3, and 5 h, respectively. The structure of these samples is fairly similar. Mixtures of nanocrystals of all sizes with the same average of 22 nm exist within the co-sputtered layers. This large variation can be understood by the Ostwald Ripening process where large nanocrystals grow at the expense of smaller which shrink [19]. Size distribution comparison of these samples demonstrated in figures 4.6 (a-c), and the detail are discussed in next chapter. Compared with the TEM image of the samples annealed at 900 and 1000 °C for 1 h, the interface between the SiO₂ and SiGe layers is not flat.

On the other hand, in the sample annealed for 1 h there is a distinctive layer identified as Ge and/or SiGe precipitated onto the Si substrate which is supposed to be caused by Ge diffusion from the co-sputtering layer. Regarding the dependency of diffusion length on parameters like diffusivity of Ge atoms in SiO₂, annealing time and temperature, the sputtered pure SiO₂ layer did not act as a perfect diffusion barrier for Ge for this annealing regime. Diffusion of Ge atoms in SiO₂ and precipitation onto the Si substrate for samples annealed at elevated temperatures of 1000 °C and higher has been reported many times and generally is related to the complete miscibility between Ge and Si at high annealing temperatures. More detailed information is given

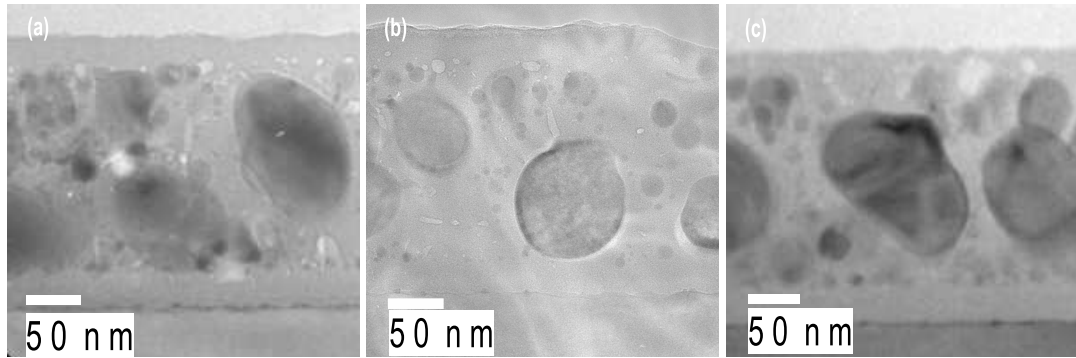


Figure 4.5: Cross-sectional TEM image of the samples annealed at 1100 °C for 1 (a), 3 (b), and 5 h (c).

in chapter 5. Also a bright contrast in the vicinity of the large islands, (like an outer shell) near the bottom SiO₂ layers, can be attributed to the Si atoms that have diffused from the substrate. Existence of large number of voids (or pores) in sputtered silicon oxide (as can be seen in our sample in figure 4.5) is necessary for diffusion of the Si atoms in the silicon oxide matrix.

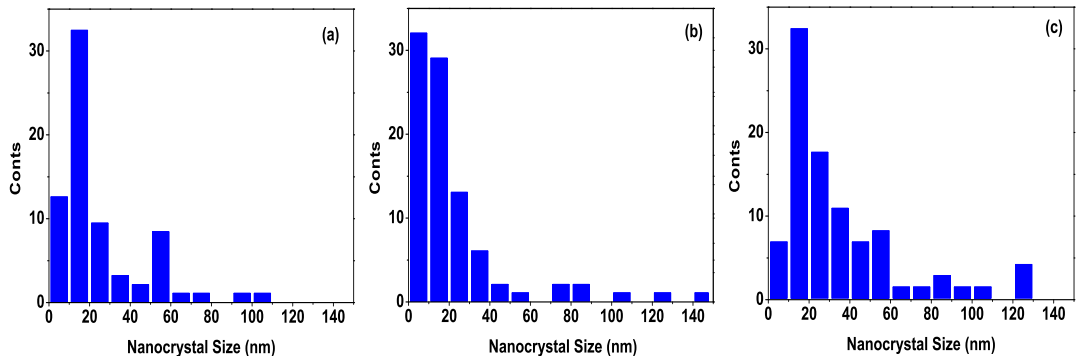


Figure 4.6: Size distribution of the nanocrystals in the sample annealed at 1100 °C for 1 (a), 3 (b), and 5 h (c).

The more striking feature in the TEM image of the samples annealed for prolonged time of 3 and 5 h, is the dark contrast appeared around the nanocrystals with sizes greater than 50 nm. These types of contrasts are often observed in TEM showing precipitates and can arise from different effects pertaining to the analysis method. Interface electron scattering often causes similar contrasts. But, this feature accompanied by a double peak formation in the XRD and Raman spectra. We interpreted

this as a phase separation in SiGe nanocrystals leading to the formation a Si-rich SiGe core covered by a relatively Ge-rich SiGe shell. We attributed this phase separation to the differences in atomic size, surface energy and surface diffusion disparity between Si and Ge atoms leading to the formation of non-homogenous structures [47]. The details are given in chapter 5.

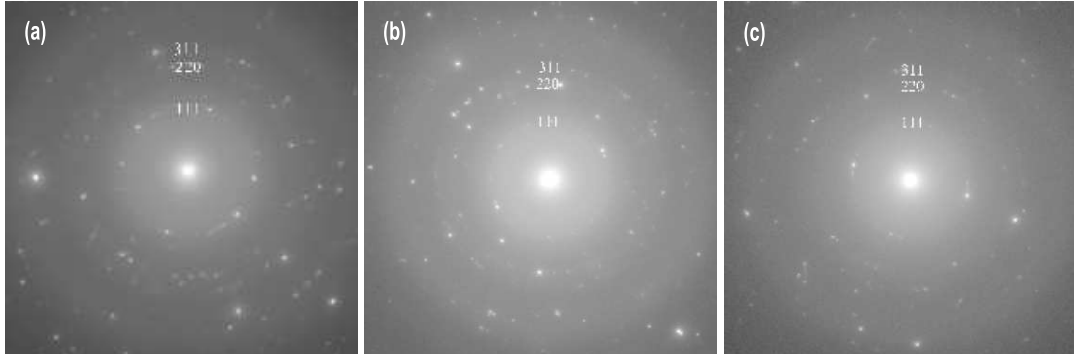


Figure 4.7: Selected area diffraction patterns of the samples annealed at 1100 °C for 1 (a), 3 (b), and 5 h (c).

Evolution of the cross-section TEM of samples with different Ge content ($P_{Ge} = 5, 10, \text{ and } 20 \text{ W}$) annealed at 1100 °C for 1 h are given in figures 4.8 (a-c). By increasing Ge content the average size of the crystallites have been increased from 9 to 11, and 22 nm (figures 4.9 (a-c)). Ge atoms are more mobile than Si atoms and therefore increase in Ge concentration may cause the accumulation of more atoms to form larger nanocrystals. The particle density is fairly uniform for the samples with lower Ge content. The other feature is the improved crystallinity of the samples by increasing Ge content (figures 4.10 (a-c)).

High resolution TEM images and selective area diffraction pattern studied from (111) and up to (531) diffraction indicate a diamond type structure of the samples. The reflections have uniform broadness and do not indicate any superposition of two diamond type nanocrystals of different unit cell size. The lattice spacing of the first diffraction ring [(111) plane] for all the sample is between those of Si (0.314 nm) and Ge (0.327 nm). SiGe nanocrystals of a wide range of sizes exist in all the samples.

Figure 4.11 (a) shows a magnification of the diffraction pattern originating from the

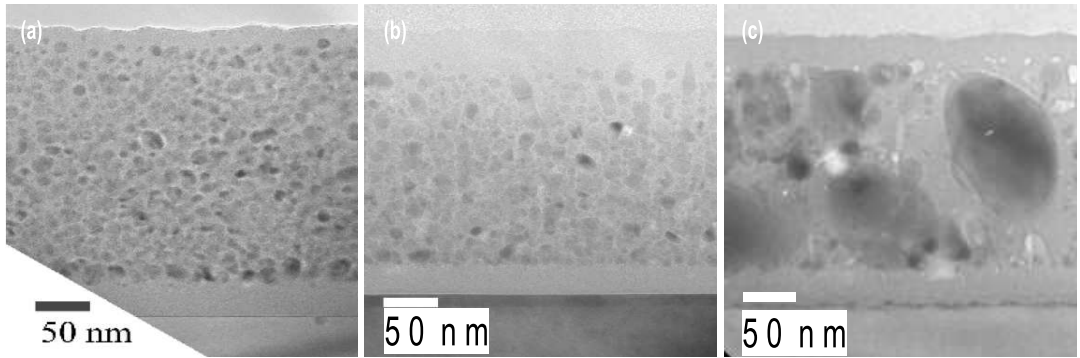


Figure 4.8: Cross-sectional TEM image of the samples with P_{Ge} of 5 (a), 10 (b), and 20 W (c) and annealed at 1100 °C for 1 h.

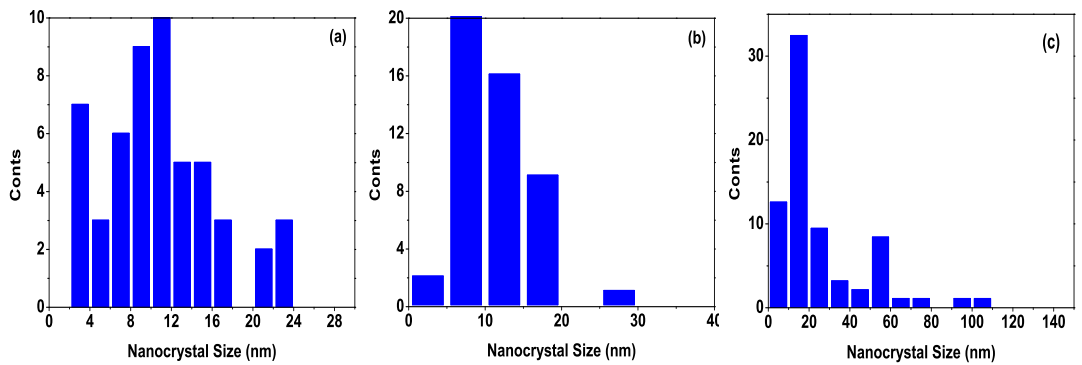


Figure 4.9: Size distribution of the nanocrystals in the sample with P_{Ge} of 5 (a), 10 (b), and 20 W (c) and annealed at 1100 °C for 1 h.

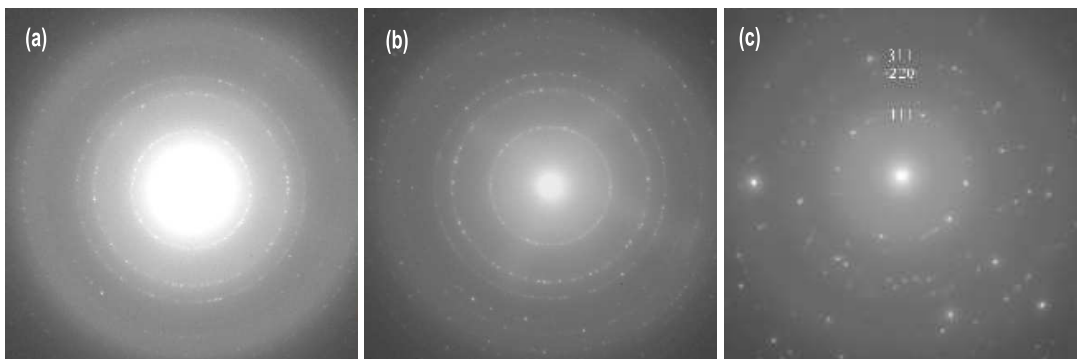


Figure 4.10: Selected area diffraction patterns of the samples with P_{Ge} of 5 (a), 10 (b), and 20 W (c) and annealed at 1100 °C for 1 h.

sample annealed at 900 °C for 1 h, in which higher order reflection are indexed. The reflection (531) was used to see if there was any indication of superposition of Ge

and Si intensities. This reflection has higher intensity than neighboring reflections (440) and (611), and is thus easier to distinguish in the diffraction pattern. Based on the nanocrystal crystal size as measured by HRTEM, the broadness of Ge and Si (531) reflection intensities can be calculated. A superposition of Ge and Si reflection intensities has been compared to the experimental diffraction signal from the sample annealed at 900 °C for 1 h, and is illustrated in figure 4.11 (b). The experimental diffraction has a peak that lies between the (531) reflection of the Si and Ge signal, and also has a shape that does not match the calculated diffraction pattern. The diffraction pattern of the film originates thus from one phase, *i.e.* a SiGe phase.

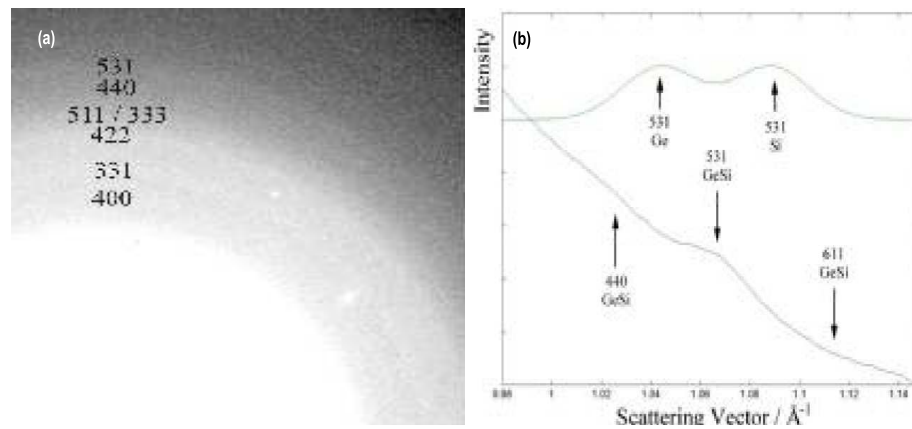


Figure 4.11: The higher hkl reflections of the sample annealed at 900 °C for 1 h (a), and a superposition of Ge and Si (531) reflection intensities of the sample annealed at 900 °C for 1 h compared with calculated values of Si and Ge (b)

Reflection (531) is flanked by (440) and (611) reflections. The (531) reflection is stronger than these two due to higher number of possible combinations of h, k and l. The top and bottom graph in figure 4.11 (b) represents diffraction signal from calculated diffraction pattern and the experimental diffraction pattern in figure 4.2, respectively, as function of scattering vector $\vec{s} = \vec{k}' - \vec{k}$. The calculated pattern is a superposition of Ge and Si (531) reflection signal, based on the nanocrystal size.

4.2 X-Ray Photoemission Spectroscopy (XPS)

In this case, the incident x-ray beam again excites atomic core levels to produce photoelectrons. However the energy spectrum of these particles is then measured, often using an electrostatic analyzer. In this way, with a suitably small energy spread in the incident x-ray beam, it is possible to determine small shifts in the core levels or the valence band of the atomic assembly in order to assess the chemical state of the probed atoms. The thickness of the analyzed layer in a sample is effectively the photoelectron escape depth. Using this technique has given much insight [48] into oxidation processes occurring in nanostructured material.

4.2.1 Experimental Results

As discussed in previous chapter, we have prepared $\text{SiO}_2/\text{SiO}_2$: Si: Ge/ SiO_2 sandwich films embedded on Si substrate by rf magnetron co-sputtering method with powers of $P_{\text{SiO}_2} = 350 \text{ W}$, $P_{\text{Si}} = 100 \text{ W}$, and $P_{\text{Ge}} = 0, 5, 10, \text{ and } 20 \text{ W}$. The bottom SiO_2 layer with the thickness of about 40 nm was deposited on Si to restrain Ge atoms from growing epitaxially on the Si substrate in the post-annealing process. The top SiO_2 layer with the thickness of about 40 nm was deposited to impede the diffusion of Ge atoms out of the surface. The thickness of the co-sputtered layer was fixed for all the samples (about 270 nm). By fixing deposition parameters of the Si and SiO_2 and varying that of Ge target, measurements have been performed to study the effect of Ge content on the annealing time and temperature evolution of the structural and optical properties of the nanocrystals. To do this, it is important to know the elemental composition of the atoms in the co-sputtered layer. Therefore, we should do XPS depth sputtering process until taking data from this region. On the other hand, on the surface there exist C atoms due to the contamination, which affects the elemental composition. So, to obtain the exact values of the elemental composition we should do sputtering until that of the C become zero and take the steady state data from the co-sputtering layer.

The XPS depth profile of the as-grown samples is carried out to obtain the relative elemental concentration in the co-sputtered layer. Equipping Specs XPS system at a vacuum of $1 \times 10^{-7} Pa$ depth profiles of Si, Ge, O, and C atoms were recorded. After three time sputtering with 2000 eV Ar^+ ions with the cycle of 2 min followed by a 4 min 3500 eV sputtering of the as-grown sample with $P_{Ge} = 20 W$, the steady state elemental composition values of 19, 32.9, 48.1, and 0 have been obtained for Ge, Si, O, and C atoms, respectively. For the sample with $P_{Ge} = 10 W$, the additional sputtering with 3500 eV Ar^+ ions with the cycle of 4 min has been performed two times, and the steady state elemental composition values of 9.1, 39, 51.9, and 0 have been obtained for Ge, Si, O, and C atoms, respectively. For the sample with $P_{Ge} = 5 W$, the additional sputtering with 2000 eV Ar^+ ions with the cycle of 6 min has been performed three times, and the steady state elemental composition values of 6.7, 40.5, 52.8, and 0 have been obtained for Ge, Si, O, and C atoms, respectively. The XPS depth profile of the as-grown samples with $P_{Ge} = 5, 10,$ and $20 W$ are given in figures 4.12 (a-c). As can be seen while the relative concentration of Ge increases by increasing P_{Ge} , those of O and Si decrease. This is due to the incorporation of more Ge atoms in co-sputtered layer and relative decrease of the co-sputtering time by increasing P_{Ge} .

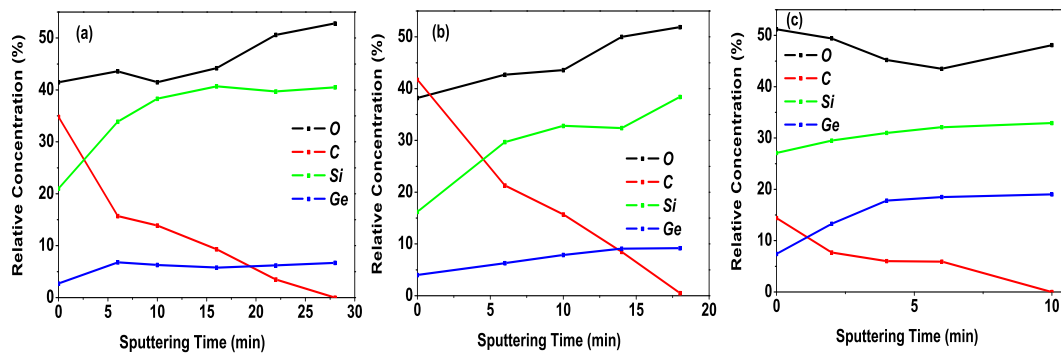


Figure 4.12: The relative concentration of Ge, Si, O, and C with sputtering time in as-grown samples with $P_{Ge} = 5$ (a), 10 (b), and $20 W$ (c).

4.3 X-Ray Diffraction Spectroscopy (XRD)

X-ray diffraction is a very versatile nondestructive technique. Information concerning bulk properties, *e.g.* the lattice constant of a material, the strain status of a layer, the mean crystalline size, and the Ge content of x in the case of $\text{Si}_{1-x}\text{Ge}_x$ nanostructures can be derived. The x-ray measurements were performed with an XRD diffractometer using the monochromatic Cu $K\alpha$ line at 1.5418 \AA . This wavelength is smaller than the lattice constant of silicon. Therefore, the incident plane wave is diffracted from the crystal. By using the XRD signals corresponding to (hkl) diffraction we can calculate the lattice constant for $nc\text{-Si}$ and $nc\text{-Si}_{1-x}\text{Ge}_x$ at the Bragg angle of:

$$\theta_{hkl} = \arcsin\left(\frac{n_{hkl}\lambda_{hkl}}{2a}\right) \quad (4.1)$$

with:

$$n_{hkl} = \sqrt{h^2 + k^2 + l^2} \quad (4.2)$$

where n_{hkl} Bragg peak, h, k, l Miller indices of the crystal plane, a lattice constant, θ_{hkl} Bragg angle, and λ_{hkl} is x-ray wavelength. Bragg peaks are measured by continuously changing ω while at the same 2θ is changed by double that amount. Rocking curves, *i.e.* diffracted beam intensity vs. incidence angle ω , are obtained from such $\omega - 2\theta$ -scans (figure 4.13).

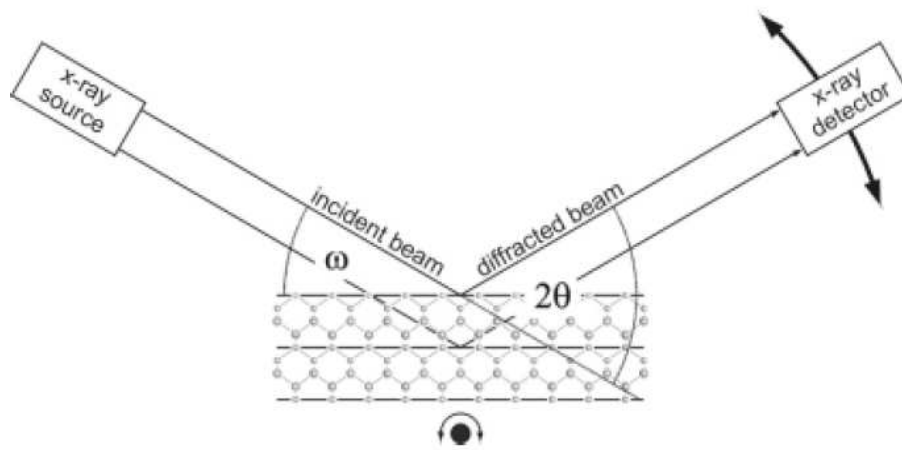


Figure 4.13: The x-ray diffraction geometry.

By using the obtained a values (a_{nc}) and its variation with respect to bulk Si and $\text{Si}_{1-x}\text{Ge}_x$ lattice constant (a_{bulk}), we can calculate the amount of strain on the nanocrystals and its evolution under annealing treatment from [49]:

$$\epsilon = \frac{\Delta a}{a_{bulk}} \quad (4.3)$$

where Δa is the difference between the lattice constant of the bulk and nanocrystalline structures.

Once the lattice constant of the $\text{Si}_{1-x}\text{Ge}_x$ alloy nanocrystals has been obtained, we can calculate the composition x by using:

$$a_{\text{Si}_{1-x}\text{Ge}_x}(x) = 5.431 + 0.1992x + 0.002733x^2. \quad (4.4)$$

This value was obtained by means of the relationship between lattice constant and Ge content, assuming that $nc\text{-Si}_{1-x}\text{Ge}_x$ is fully relaxed like crystalline bulk $\text{Si}_{1-x}\text{Ge}_x$ alloy [4]. However, because of the possible stress development on the nanocrystals, the actual value of x could be somewhat different. By using Raman spectra, we can determine the Ge content of x assuming that $\text{Si}_{1-x}\text{Ge}_x$ assuming a random mixing in the alloy, from the relative integrated intensities of the Ge-Ge and Si-Ge peaks. The values obtained from Raman and XRD analysis are in agreement with each other. However based on assumptions in both techniques, estimating the Ge composition include some uncertainties.

X-ray diffraction pattern also can be used to obtain the average size of the nanocrystals. It is well known that as a diffracting crystallographically coherent region becomes spatially smaller, the Bragg peaks are broadened. The volume average size of the diffracting region (D) can be related to the full width at half maximum w of a Bragg peak in a 2θ scale through the Scherrer formula [50]:

$$D = \frac{K\lambda}{B \cos \theta} \quad (4.5)$$

where λ is the x-ray wavelength (0.15418 nm), θ is the Bragg angle, and K is a constant on order of unity whose exact value depends on the specific shape and size distribution of the crystalline clusters and on the specific crystallographic direction of the diffracting planes. Calculated values for the (111) direction in many different

shapes and structures are close to $K = 1.2090$ to within few percent, so we have consistently adopted this value for the (111) reflection [51].

The FWHMs of the diffraction peaks were corrected for the instrumental broadening as measured for a polycrystalline Si sample before introducing them into equation 4.5 to determine D . Both instrument and specimen broaden the diffraction lines, and the observed line profile is a convolution [51]:

$$h(x) = g(x) * f(x) + \text{background} \quad (4.6)$$

To obtain microstructural parameters of the specimen, the physically (specimen) broadened profile f must be extracted from the observed profile h . The halfwidths $2\omega_f$ of the intrinsic (desired, specimen, physical) diffraction can be calculated by the formulas which are based on assumption on the shapes of the observed (measured) and instrumental profiles. If these are assumed to be Lorentzian-Lorentzian (LL), Gaussian-Gaussian (GG), or Lorentzian-Gaussian (LG), then [52]:

$$2\omega_f = 2\omega_h - 2\omega_g \quad (4.7)$$

$$2\omega_f = \sqrt{(2\omega_h)^2 - (2\omega_g)^2} \quad (4.8)$$

$$2\omega_f = 2\omega_h - \frac{(2\omega_g)^2}{2\omega_h} \quad (4.9)$$

respectively, where $2\omega_h$, $2\omega_g$ and $2\omega_f$ are halfwidths of the measured profile, the instrumental profile and the intrinsic profile respectively.

On the other hand, By using the XRD signal corresponding to (111) diffraction for determining quantities such as the mean crystallite size D and the root-mean-square strain $\langle e^2 \rangle^{1/2}$. We obtained these quantities by using pseudo-Voigt function in the variance-range method from the following expressions [51]:

$$w_{0f} = \frac{-L\lambda^2}{4\pi^2 D^2 \cos^2 \theta_0} + 4 \tan^2 \theta_0 \langle e^2 \rangle \quad (4.10)$$

$$k_f = \frac{K\lambda}{\pi^2 D \cos \theta_0} \quad (4.11)$$

where w_{0f} and k_f are intercept and slope parameters of the 'pure' or 'intrinsic' diffraction profile variance. We have used the Levenberg-Marquardt nonlinear least-squares

method to fit the individual peaks by a pseudo-Voigt function. The parameters K and L is related to the shape of the crystallites, and by assuming a spherical shape for the crystallites the values of $K = 1.2090$ and $L = 0$ have been used [51]. In the whole range between the Gauss and Lorentzian extremes of the strain-broadened Voigt profile. For Gauss strain broadening, $\frac{\epsilon}{\langle e^2 \rangle^{1/2}} \sim \sqrt{\frac{\pi}{2}} \sim 1.253$, and otherwise $0.5 \leq \frac{\epsilon}{\langle e^2 \rangle^{1/2}} \leq 2$. Besides the instrumental broadening correlation considered here, background and Cu $K\alpha_2$ line correlation have been applied as well.

4.3.1 Experimental Results

The XRD measurements were conducted with Rigaku Miniflex X-Ray powder diffractometer, using Conventional Bragg-Brentano $\omega-2\theta$ -scans to obtain the lattice constant, average size, Ge content of x , strains, and root-mean-square strain of the nc -Si and nc -Si $_{1-x}$ Ge $_x$ structures. The Cu $K\alpha$ line at 1.5418 Å was used as X-Ray source, and measurements were first conducted with scans between 15° and 60° at 0.04° steps acquisition time per angular step of 5 sec. Three peaks resolved at 2θ of about 28, 46, and 54° corresponding to (111), (220), and (311) diffractions have been observed, which are located between the expected (111), (220), and (311) Bragg peaks of Si and Ge. Then, the XRD measurements have performed with scans between 24-31 and 44-56° at 0.01° steps by long acquisition time per angular step of 15 sec to enhance the signal to noise ratio and obtain the exact position and FWHM of the peaks. The FWHM of the diffraction peak (0.13812) of a standard sample of polycrystalline Si powder, was recorded to eliminate the instrumental line broadening. The residual Cu $K\alpha_2$ was corrected by using the Rachinger correction method which assumes the intensity of the $K\alpha_2$ to be half that of $K\alpha_1$. The background correction was performed assuming quadratic polynomial background which gives the best fit. Peak profiles were assumed to be pseudo-Voigt, which is a combination of Gaussian and Lorentzian line shapes.

Figure 4.14 shows the x-ray diffraction patterns of the as-grown a -Si $_{1-x}$ Ge $_x$ and the nc -Si $_{1-x}$ Ge $_x$ annealed at 900, 1000, and 1100 °C for the same Ge power of 20 W and the same annealing time of 1 h. At first sight, the as-grown a -Si $_{1-x}$ Ge $_x$ film was

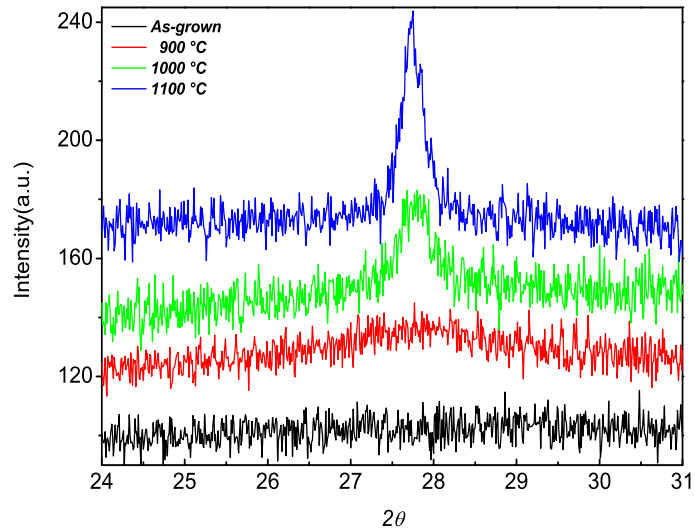


Figure 4.14: Annealing temperature evolution of the XRD spectra corresponding to the (111) diffraction in the samples with $P_{Ge}=20$ W and annealed for 1 h.

amorphous and its spectrum doesn't show any clear features. For annealed samples, in contrast, three peaks can be resolved at 27.8 , 46.3 , and 54.6° , which are located between the expected (111), (220), and (311) Bragg peaks of Si and Ge. As can also be seen, by increasing T the average size of the $nc\text{-Si}_{1-x}\text{Ge}_x$ was increased, as evidenced by the increased intensity of the peaks and reduced FWHM.

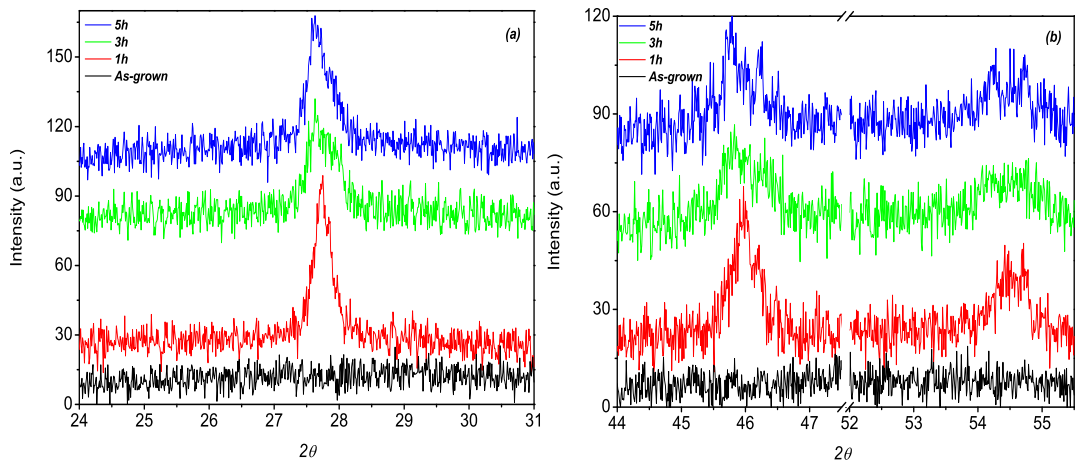


Figure 4.15: Annealing time evolution of the XRD spectra corresponding to the (111) (a), and to the (220) and (311) (b) diffractions in the samples with $P_{Ge}=20$ W annealed at 1100°C .

Figure 4.15 (a) shows the annealing time evolution of x-ray diffraction pattern of the

samples with the same $P_{Ge} = 20w$ and annealed at $1100\text{ }^{\circ}C$ for different duration of 1, 3, and 5 h. At first sight while in the XRD pattern of the sample annealed for 1 h there is a peak at 27.74° , in those of annealed for 3 and 5 h intensity decrease and the peak tends to decomposed two Gaussian peaks at 27.65 and 27.85° . As can also be seen, by increasing t from 3 h to 5 h, the intensity of the decomposed peak located at 27.85 doesn't change and that of located at 27.65° increase. Note that this feature is more clear for peaks located at 46 and 54.5° corresponding to (220) and (311) diffractions (figure 4.15 (b)). We attributed this tendency to the formation of core-shell structure in Ge-rich $nc\text{-Si}_{1-x}\text{Ge}_x$ during prolong annealing at higher temperatures. The more detailed discussion are given in chapter 5.

Figure 4.16 demonstrates the XRD spectra of the $nc\text{-Si}_{1-x}\text{Ge}_x$ prepared with different Ge power of $P_{Ge}=0, 5, 10,$ and $20 w$ and annealed at $1100\text{ }^{\circ}C$ for 1 h. It can be seen that the peak becomes narrower and intense as P_{Ge} increases, and shift to the lower 2θ values *i.e.* toward the Ge (111) diffraction peak. This implies that the mean size of crystalline regions and the Ge content of x increase with increasing excess Ge.

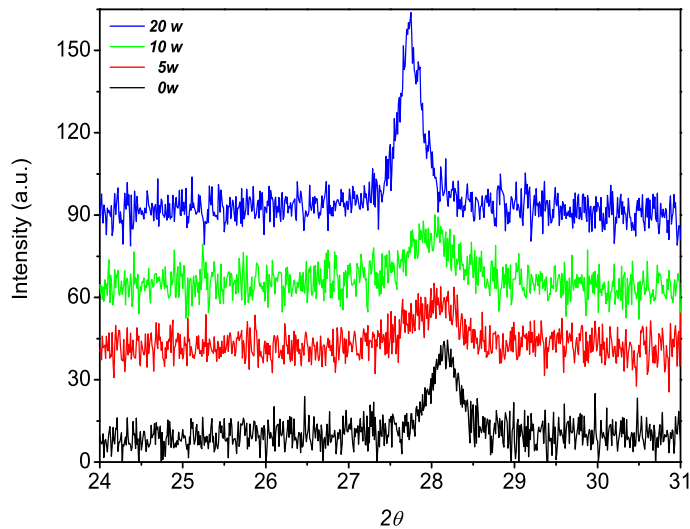


Figure 4.16: Evolution of the XRD spectra corresponding to the (111) diffraction in the samples with different $P_{Ge}=0, 5, 10,$ and $20 W$ annealed at $1100\text{ }^{\circ}C$ for 1 h.

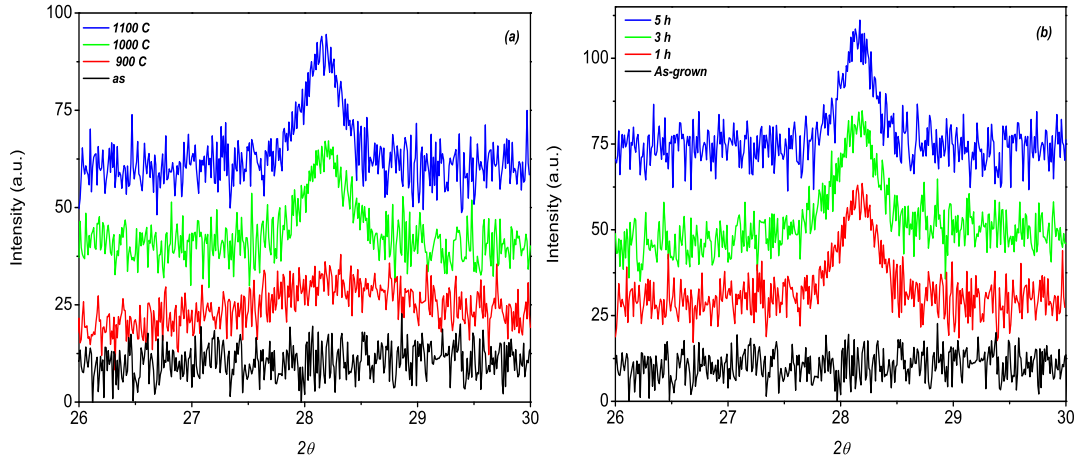


Figure 4.17: Annealing temperature (a) and annealing time (b) evolution of the XRD spectra corresponding to the (111) diffraction in the samples with $P_{Ge}=0$ W (Si nanocrystals).

4.4 Fourier Transform Infrared Spectroscopy (FTIR)

Infrared spectroscopy is one of the most widely used techniques for the study of the structure of amorphous silicon-based alloys. It is easily performed, is nondestructive, and gives information about bonding configurations and concentrations. The IR method is a powerful tool for studying relative concentrations of elements in the alloy and, when calibration is possible, absolute concentrations. Information about the structure of the films is usually obtained through the integrated absorption peaks of the considered vibrational mode from the relationship

$$I = \int \frac{\alpha(\omega)}{\omega} d\omega \quad (4.12)$$

where $\alpha(\omega)$ is the IR absorption coefficient; the integration is performed over the deconvoluted IR peaks after subtraction of the baseline. The intensity of the peaks is related to the absolute concentration of bonds. For the A-B bond the concentration of oscillators is given by

$$N_{A-B} = A_{A-B} \int \frac{\alpha(\omega)}{\omega} d\omega \quad (4.13)$$

where A_{A-B} is a constant depending on the refractive index of the material and the effective charge or oscillator strength of the dipole [53].

4.4.1 Experimental Results

The rf magnetron co-sputtering like ion implantation introduces many kinds of point defects into SiO₂ network. However, this network is characterized by a smaller degree of damage than that after a high-dose implantation. To identify structural damage to the SiO₂ network caused by sputtering and annealing, FTIR spectra were measured to determine the defect characteristics connected with the observed PL. In the stoichiometric SiO₂ film, three vibrational bands exist at 470, 810, and 1086 cm^{-1} , corresponding to rocking, bending, and asymmetric stretching vibrations of Si-O-Si bond, respectively [54]. These frequencies can vary with preparation technique, for example the latter one varies between about 1086 cm^{-1} for thermally grown SiO₂ to about 1055 cm^{-1} for SiO₂ deposited by low-temperature PECVD techniques. There are three modifications to the Si-O-Si asymmetric stretching band with decrease in the [O] / [Si] ratio: (i) the position of the peak decreases, (2) the characteristic shoulder on the high-frequency side of the band disappears, and (3) the full width at half maximum increases.

In the FTIR spectra of the as-grown samples another peak appears at 880 cm^{-1} , which has been annealed out during the heat treatment. This indicates that the as-grown co-sputtered samples are more off stoichiometric and thus many kinds of point defects have been formed, which some of them such as NOV and NBOHC are radiative recombination centers. The 880 cm^{-1} absorption mode has been discussed in the literature as a mode related to NBOHC situated on Si₆ rings as the origin of luminescence signal at 570-630 nm [55, 56] and disappears at temperatures above 900 °C [57]. On the other hand, for annealed co-sputtered samples specially those annealed at 1100 °C for prolong times of 3 and 5 h , in the low wave numbers side of the main Si-O-Si asymmetric stretching band a shoulder appears which has been attributed to the deep level defect states arising from Si dangling bond defects (p_b center) [57]. These defects exist in the nc -Si/SiO₂ interface which can be neutral, positively, or negatively charged [58]. Theoretically it has been founded that the carrier trapping at neutral p_b centers is nonradiative, whereas capture at charged centers can lead to photon emission at energies smaller than the bandgap of bulk silicon. Some experimental

studies ascribing the broad infrared emission band at 0.8-0.9 eV to the recombination of carriers trapped at Si dangling bonds have been reported.

In the annealed SiGe samples on the low-frequency side of the main Si-O-Si asymmetric stretching band a new shoulder appears, where corresponds to the Si-O-Ge vibration, and appears at 990 cm^{-1} . This shoulder changes with annealing temperature (T) and annealing time (t). The other feature is the increased intensity of the characteristic shoulder on the high-frequency side of the main Si-O-Si asymmetric stretching band in the co-sputtered samples. This shoulder corresponds to the asymmetric stretching mode of Si-O-Si vibration when two adjacent O atoms move out of phase (AS2TO) and has been attributed to coupled modes induced by disorder and its intensity provides then an estimation of disorder [54]. Based on quantum chemical calculations, Gole *et al.* suggested that a portion of the FTIR spectrum for a heavily oxidized porous silicon in the range $1100\text{-}1300\text{ cm}^{-1}$ can be reassigned to the Si=O stretching mode of the silanone-based oxyhydrides [60].

The FTIR spectroscopy was measured using Equinox spectrometer (Bruker), in the absorbance mode at wavenumbers between $400\text{-}4000\text{ cm}^{-1}$ with a resolution of 2 cm^{-1} . The FTIR absorbance spectra of the as-grown and annealed samples with $P_{SiO_2}=350\text{ W}$, $P_{Si}=100$, and 0 W , and $P_{Ge}=0, 5, 10$, and 20 w are discussed in detail in chapters 6 and 7.

4.5 Raman Spectroscopy

Raman spectroscopy is a powerful tool in studying the structural properties of crystalline and amorphous semiconductors [61]. In the first class of materials, only optical photons near the Γ point of the Brillouin zone can be annihilated or created, yielding respectively Stokes and anti-Stokes first-order Raman spectra, owing to the wave vector selection rule. In this case the position of the peaks from polarized Raman spectra can yield useful information about the stress of the network [62]. In second-order Raman scattering, all the phonons through the Brillouin zone can participate in photon-phonon interactions, so that, neglecting phonon interactions of higher or-

der yielding combination bands, the resulting spectra well reproduce the one-phonon density of states (PDOS) in which the frequency shift represents the double of the vibrational frequency [63].

4.5.1 Experimental Results

In general, the first-order Raman spectrum of a $\text{Si}_{1-x}\text{Ge}_x$ alloy consist of three main peaks due to nearest-neighbor Ge-Ge ($\sim 300 \text{ cm}^{-1}$), Si-Ge ($\sim 400 \text{ cm}^{-1}$), and Si-Si ($\sim 500 \text{ cm}^{-1}$) stretching vibrations [64]. The latter is weak in Ge-rich alloys and is also masked by the intense peak coming from the Si substrate. There are three main factors that affect the Raman frequencies of the $\text{Si}_{1-x}\text{Ge}_x$ alloy, Ge content of x , stress, and phonon confinement effect. With respect to the bulk relaxed $\text{Si}_{1-x}\text{Ge}_x$ (or Si) nanocrystals the Si-Ge, Si-Si and Ge-Ge bonds shift towards higher wave numbers [65] can result from the compressive stress on the nanocrystals due to the stretching of bonds with respect to relaxed $\text{Si}_{1-x}\text{Ge}_x$ (or Si) occurring near the interface of nanocrystals and SiO_2 matrix. As discussed early in XRD subsection, the stress resulted from volume expansion of $\text{Si}_{1-x}\text{Ge}_x$ during cooling down process can affect the Raman vibration modes as well. This effect will be more influenced in the sample for extended annealing. We note that, phonon confinement effect which is evident only for the crystallite sizes smaller than nanocrystals Bohr radius. The Ge content of x affects the Ge-Si vibration. Its intensity increases by increasing x and shifts towards the Ge-Ge vibration *i.e.* towards lower wave numbers [66].

The Raman spectra of the $\text{Si}_{1-x}\text{Ge}_x$ nanocrystals can be used to determine the Ge content of x . Assuming random mixing in the alloy, from the relative integrated intensities of the Ge-Ge and Si-Ge peaks [67], the Ge composition can be found by using the following expression:

$$\frac{I_{\text{Ge-Ge}}}{I_{\text{Si-Ge}}} = \frac{n_{\text{Ge-Ge}} + 1}{n_{\text{Si-Ge}} + 1} \frac{\omega_{\text{Si-Ge}}}{\omega_{\text{Ge-Ge}}} \frac{x^2}{2x(1-x)} \quad (4.14)$$

$I_{\text{Ge-Ge}}$ and $I_{\text{Si-Ge}}$ were obtained by integrating the areas under each peak and the $n_{\text{Ge-Ge}}$ and $n_{\text{Si-Ge}}$ are the Bose factors for the Ge-Ge and Si-Si phonon modes and ω 's are the frequencies of these different modes. The third term represents the relative fraction

of bonds in the alloy. From the XRD measurements, the obtained value is somewhat different. These two values obtained from Raman and XRD analysis are in agreement with each other. However based on assumptions in both techniques, estimating the Ge composition has uncertainties. For instance as discussed in the previous section, XRD data predicts the presence of a strain in the nanocrystals opposed to the assumption made in the calculation of Ge composition by XRD.

Raman scattering spectra were taken on a confocal micro-Raman (HR800, Jobin Yvon), attached with Olympus microanalysis system and a charge-coupled device (CCD) camera providing a resolution of 1 cm^{-1} . The spectra were carried out in backscattering geometry with the 632.8 nm line of He-Ne laser at room temperature. The more detailed information about evolution of the Raman spectra by Ge content, annealing temperature and time are given in the following chapters.

CHAPTER 5

OBSERVATION OF CORE-SHELL STRUCTURE IN $\text{Si}_{1-x}\text{Ge}_x$ NANOCRYSTALS

5.1 Motivation

In recent years, Si, Ge and their alloy nanostructures embedded in a dielectric matrix have widely been investigated because of their potential application in nanoelectronics and optoelectronics [68, 69]. In particular; the use of nanocrystals in flash memory cells instead of conventional floating gate is expected to improve the device reliability [70]. Alloy $\text{Si}_{1-x}\text{Ge}_x$ nanocrystals provide an advantage of fine tuning the electronic band structure which plays a detrimental role in the charging/discharging, and retention properties of the memory element [71]. In order to fabricate high performance devices with $\text{Si}_{1-x}\text{Ge}_x$ nanocrystals, it is necessary to know and control their structural and electrical properties [72, 73] which depend on several factors, including particle size, shape, surface condition, atomic composition, and compositional uniformity. Considering only thermodynamics of bulk materials, homogenous $\text{Si}_{1-x}\text{Ge}_x$ nanocrystals embedded in a SiO_2 matrix would be an equilibrium situation [68]. This situation has also been reported for annealing SiO_2 supersaturated by Si and Ge using ion implantation [74] or sputtering [75]. Other structures can be thought to exist in such a material system when taking surface effects and kinetics into consideration. There have been several theoretical studies on clusters of $\text{Si}_{1-x}\text{Ge}_x$ alloys indicating that a core-shell structure can be more stable than a homogenous structure [76, 77].

In the last few years, much effort has been focused on the synthesis, fabrication, and

characterization of the core-shell structures with tailored applications [73, 78]. At high Ge content, for samples prepared by rf magnetron co-sputtering and annealed at high temperatures no homogeneous $nc\text{-Si}_{1-x}\text{Ge}_x$ but a kind of composite nanocrystals consisting of a $nc\text{-Ge}$ core and amorphous $\text{Si}_{1-x}\text{Ge}_x$ shell evidenced from the Raman analysis was reported [79, 80]. From other experiments, Alonso *et al.* [81] by using molecular beam epitaxy method and Malachias *et al.* [82] by using chemical etching method observed dome islands that present spherical profiles consisting of a Si-rich core covered by a Ge-rich shell. In more recent experiments, $\text{Si}_{1-x}\text{Ge}_x$ self-assembled islands composed of strained Ge core and a more relaxed $\text{Si}_{1-x}\text{Ge}_x$ shell prepared by molecular beam epitaxy method were reported [83, 84]. A composition gradient in the $\text{Si}_{1-x}\text{Ge}_x$ nanocrystals can possibly arise by high temperature treatment of $\text{Si}_{1-x}\text{Ge}_x$ nanocrystals in SiO_2 on Si where several effects may contribute to the end results which could be different than those for a free $\text{Si}_{1-x}\text{Ge}_x$ particle. There is possibly a flux to and from the particles (islands ensemble) resulting in Ostwald ripening, which will be influenced by the different surface energies of small and large particles as well as Si or Ge bonds on the particle surface. These fluxes are coupled to flux to and from the substrate involving epitaxial growth on the substrate and a possible particle flux that can react with species from the ambient during annealing forming some new oxide [85].

We studied the effect of annealing time and temperature on the structural and compositional properties of $\text{Si}_{1-x}\text{Ge}_x$ nanocrystals prepared by rf magnetron co-sputtering method by transmission electron microscopy (TEM), X-ray diffraction (XRD), and Raman spectroscopy measurements. The evolution of $\text{Si}_{1-x}\text{Ge}_x$ nanocrystals has been monitored during high temperature annealing. Results indicate that a phase separation of Si and Ge takes place during long enough high temperature annealing or cooling down process leading to an inhomogeneous structure consist of a Si-rich SiGe core covered by a relatively Ge-rich SiGe shell.

5.2 Experimental Details

The samples used in this work were $\text{Si}_{1-x}\text{Ge}_x$ rich SiO_2 layer sandwiched between two SiO_2 films deposited on Si substrate by rf magnetron co-sputtering from three independent target materials with powers of $P_{\text{SiO}_2} = 350\text{W}$, $P_{\text{Si}} = 100\text{W}$, $P_{\text{Ge}} = 20\text{W}$. The bottom SiO_2 layer with the thickness of about 40 nm was deposited on Si to restrain Ge atoms from growing epitaxially on the Si substrate in the post-annealing process. The top SiO_2 layer with the thickness of about 40 nm was deposited to impede the diffusion of Ge atoms out of the surface. Deposition parameters were fixed to study the effect of annealing time on the local structure of the samples. The typical deposition rate was 4 nm/min, and the thickness of the films was about 350 nm. The XPS depth profile of the as-grown sample is carried out to obtain the relative elemental concentration. Equipping Specs XPS system at a vacuum of 1×10^{-7} Pa depth profiles of Si, Ge, O, and C atoms were recorded. After sputtering three times with 2000 eV Ar^+ ions with the cycle of 2 min followed by a 4 min 3500 eV sputtering the steady state elemental composition values of 32.9, 19, 48.1, and 0 percent have been obtained for Si, Ge, O, and C atoms, respectively.

After deposition, wafers were cleaved and annealed in a quartz tube furnace under flowing N_2 gas at ambient pressure for 1, 3, and 5 h at 1100 °C to understand compositional variations of the nanocrystals in the prolonged high temperature regime. In general, the formation mechanism for $\text{Si}_{1-x}\text{Ge}_x$ nanocrystals embedded in SiO_2 matrix goes through the familiar sequence of nucleation and growth, often followed by coarsening of nanocrystals due to Ostwald ripening. The formation and evolution of $\text{Si}_{1-x}\text{Ge}_x$ nanostructures were studied by cross-sectional high-resolution electron microscope [JEOL2010F]. X-ray diffraction measurements were carried out with the $\text{Cu } K\alpha$ line of a powder diffractometer to obtain conventional 2θ scans between 24-31 and 44-56° at 0.01 steps. This range of 2θ was scanned by long acquisition time per angular step of 15 sec to obtain the exact position and FWHM of the peaks correspond to (111), (220), and (311) diffractions. Raman scattering spectra were taken on a confocal micro-Raman (HR800, Jobin Yvon), attached with Olympus microanaly-

sis system and a charge-coupled device (CCD) camera providing a resolution of 1 cm^{-1} . The spectra were carried out in backscattering geometry with the 632.8 nm line of He-Ne laser at room temperature.

5.3 Observation of Core-Shell Structure by TEM

Among the various sets of samples, in a set with sputtering parameters of $P_{SiO_2} = 350W$, $P_{Si} = 100W$, $P_{Ge} = 20W$ (leading to the formation of Ge-rich $Si_{1-x}Ge_x$ nanocrystals) and annealed at $1100 \text{ }^\circ\text{C}$ for different duration of 1-5 h , an interesting feature has been observed. It was deconvolution tendency of the $Si_{1-x}Ge_x$ related peaks in XRD and Raman measurements in the samples annealed for enough long times. This feature was examined by TEM measurements as well.

Figures 5.1 (a) and 5.1 (b) show the evolution of cross-sectional TEM image of the samples annealed at $1100 \text{ }^\circ\text{C}$ for 1, and 3 h . The circular features seen have been identified to be $Si_{1-x}Ge_x$ nanocrystals from high resolution interference fringes and from selected area diffraction (insets of figures 5.2 (a) and 5.2 (b)). Mixtures of nanocrystals of all sizes with the same average of 22 nm exist within the co-sputtered layers. This large variation can be understood by the Ostwald Ripening process where large nanocrystals grow at the expense of smaller which shrink [86]. Size distribution comparison of these two samples indicates that (figures 5.2 (a) and 5.2 (b)) for the sample annealed for a long time of 3 h the number of nanocrystals with sizes $\leq 10 \text{ nm}$ is about three times of the sample annealed for 1 h , and also large nanocrystals with sizes $> 150 \text{ nm}$ are formed accompanied by significant decrease in the number of nanocrystals having moderate size of 50 nm . The SiO_2 layer between the co-sputtered layer and the substrate does not appear to contain Ge and/or SiGe nanocrystals. This is an expected feature for this annealing treatment, the concentrations in this SiO_2 layer will be less than the solid solubility so there is no driving force for segregation except perhaps during the cooling down process, but since there already exist segregation sites within a short diffusion distance the concentration can be kept close to equilibrium during a large portion of the cooling down process. So, comparing with

the TEM image of the samples annealed at 900 and 1000 °C (not shown here) for 1 *h*, thickness of the upper and bottom SiO₂ layers is slightly decreased and the interface between the SiO₂ and co-sputtered layers is no longer flat.

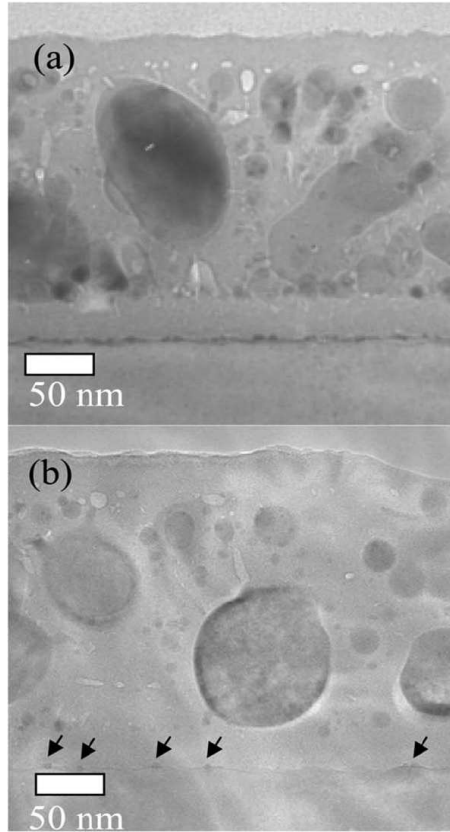


Figure 5.1: Cross-sectional TEM image of the sample annealed at 1100 °C for 1 h (a) and 3 h (b).

On the other hand, in the sample annealed for 1 *h* there is a distinctive layer identified as Ge and/or SiGe precipitated onto the Si substrate which is supposed to be caused by Ge diffusion from the co-sputtering layer. Regarding the dependency of diffusion length on parameters like diffusivity of Ge atoms in SiO₂, annealing time and temperature [87, 88], the sputtered pure SiO₂ layer did not act as a perfect diffusion barrier for Ge for this annealing regime. Diffusion of Ge atoms in SiO₂ and precipitated onto the Si substrate for samples annealed at elevated temperatures of 1000 °C and higher has reported many times and generally is related to the complete miscibility between Ge and Si at high annealing temperatures [89, 90]. In the sample annealed for 3 *h*,

the number of precipitates onto the Si substrate has been decreased and only some small spots have been observed (shown by arrows). We suggest, and justify that this observation during prolonged annealing is a consequence of the intermixing between the precipitant and the Si substrate and formation of SiGe alloy. This is similar to epitaxial systems, in which there is a large thermodynamic driving force for intermixing, because mixing reduces strain energy [91, 92]. Prolonged high temperature annealing leads to increased elemental interdiffusion at the precipitants/substrate and allow an elemental redistribution so that the system can release strain energy as much as possible. Therefore, intermixing results in the precipitants/substrate interface moving down to the substrate side and dilution/dissolving of the precipitants.

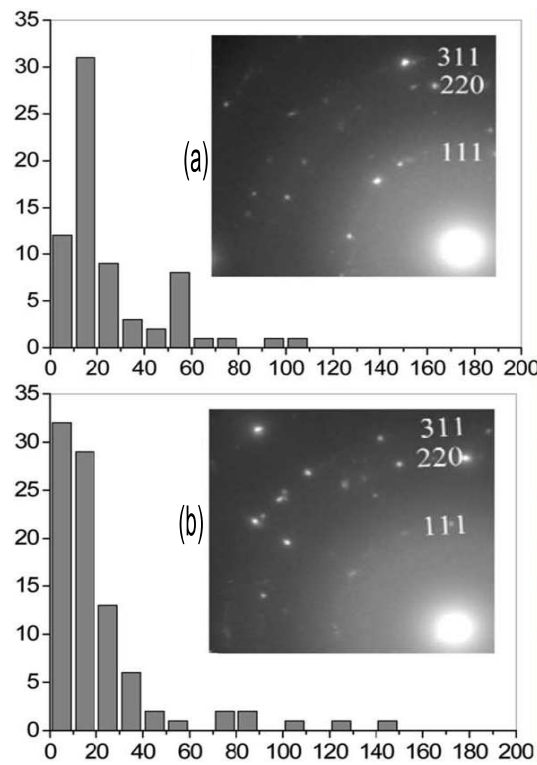


Figure 5.2: Size distribution of the nanocrystals in the sample annealed for 1 h (a) and 3 h (b). Insets show the selected area diffraction patterns.

The more striking feature in the TEM image of the sample annealed for 3 h shown in figure 5.1 (b) is the dark contrast appearing around the nanocrystals with sizes greater than 50 nm. These types of contrasts are often observed in TEM showing precipitates and can arise by different effects pertaining to the analysis method. Interface electron

scattering often causes similar contrasts. There is no direct evidence from TEM that the nanoparticles composition is different near the surface of the nanoparticle. On the other hand, it can not be excluded. As will be discussed below, there may exist driving forces due to difference in atomic sizes and surface energy between Si and Ge which may induce segregation of Ge to the surface of the nanocrystals. Also a bright contrast in the vicinity of the large islands, (like an outer shell) near to the bottom SiO_2 layers, can be attributed to the Si atoms diffused from the substrate. Existence of large number of voids (or pores) in sputtered silicon oxide (as can be seen in our sample in figure 5.1) is necessary for diffusion of the Si atoms in the silicon oxide matrix [87, 88].

5.4 Deconvolution of the XRD Peaks

Figure 5.3 shows XRD spectra for the samples annealed at 1100°C for 1, 3, and 5 h. Three peaks can be resolved at 27.7 , 46 , and 54.5° (figures 5.3 (a) and 5.3(b)), which are located between the expected (111), (220), and (311) Bragg peaks of Si and Ge. At first sight, while the XRD peak of the sample annealed for 1 h is a single diffraction peak corresponding to a single composition, in those of samples annealed for 3 and 5 h the XRD peak tends to decompose into two peaks at 27.6 and 27.9° . By increasing annealing time from 3 h to 5 h, the intensity of the decomposed peak located at 27.9° doesn't change and that of the peak located at 27.6° increases. This feature is seen more clearly for the peaks located at 46 and 54.5° correspond to (220) and (311) diffractions. This result indicates that in the sample annealed for 1 h, uniform $\text{Si}_{1-x}\text{Ge}_x$ nanocrystals with an approximate Ge content of $x = 69$ have been formed. This value was obtained by means of the relationship between lattice constant and Ge content, assuming that $\text{Si}_{1-x}\text{Ge}_x$ is fully relaxed [4]. However, because of the possible stress development on the nanocrystals, the actual value of x could be somewhat different. The evolution of the XRD peaks indicates a phase separation between Si and Ge. Figure 5.3(c) shows the decomposition of the (111) peak of the sample annealed for 3 h by two Lorentzian peaks. We attribute the peak at 27.6° to a portion containing more Ge atoms and the peak at 27.9° to that being relatively Si-rich. It is worth while

to note that nanocrystals located at different depths in SiO₂ matrix measured from the electron beam entrance surface appear like nanocrystals having different Ge content of x . Although there exists a distribution in the Ge content of the islands, the explicit phase separation owing to different Ge content in the XRD pattern should lead to the appearance of duplex in Selected area diffraction (SAD) fringes (insets of fig 5.2 (a) and 5.2 (b)). SAD patterns of two samples don't show any explicit difference between them and pair fringes result from splitting of the diffraction rings has not observed.

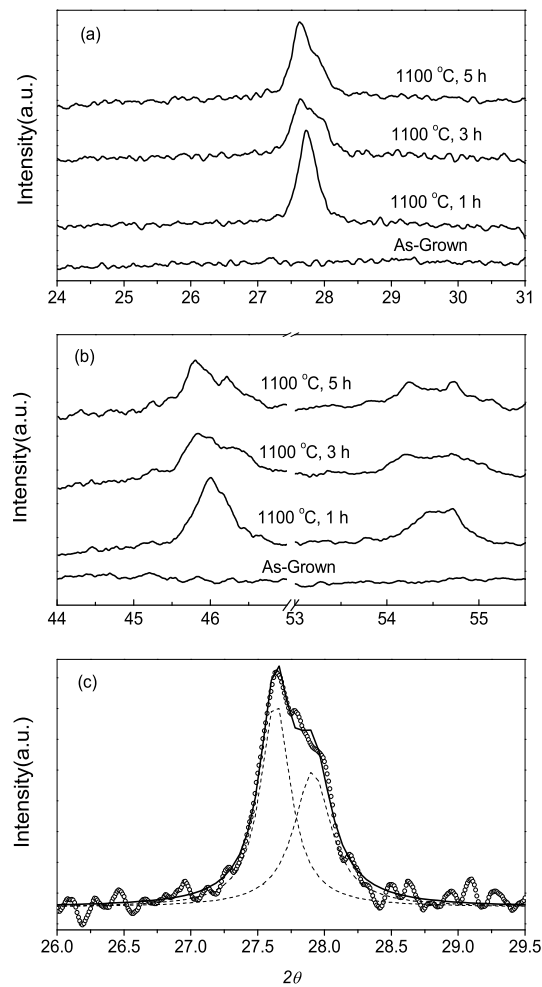


Figure 5.3: XRD pattern of the as grown and the samples annealed at different times in the 2θ interval of $24-31^\circ$ corresponding to (111) planes (a), and $44-56^\circ$ corresponding to (220) and (311) planes (b), and the decomposition of the (111) diffraction peak of the sample annealed for 3 h (c).

By using the XRD signal corresponding to (111) diffraction of the sample annealed

for 1 *h* we can estimate the mean crystallite size *D* and the root-mean-square strain $\langle e^2 \rangle^{1/2}$ [51]. We obtained these quantities by using pseudo-Voigt function in the variance-range method from the equations 4.10 and 4.11. Besides the instrumental broadening correlation considered here, background and Cu $k\alpha_2$ line correlation have been applied as well. We have obtained the values of 22 *nm* and 0.003 for mean crystallite size and root-mean-square strain, respectively, in a good agreement with the average value obtained by TEM. The observed strain can be attributed to the stretching of Si-Ge bonds (2.4 °Å) with respect to relaxed Si_{1-x}Ge_x occurring near the *nc*-Si_{1-x}Ge_x/oxide interface due to the shorter Si-O bonds (1.6 °Å). On the other hand, annealing temperature is a critical parameter in evolution of Si_{1-x}Ge_x nanocrystals. Regarding this, the melting point of Si_{1-x}Ge_x alloy should be considered. It decreases with increasing Ge content. In our system, the liquidus-solidus diagram [94] shows that Si_{0.31}Ge_{0.69} (or Si_{0.35}Ge_{0.65} by Raman analysis) is in a partially melted state at 1100 °C. It is then reasonable to expect that volume expansion of Si_{1-x}Ge_x during liquid to solid transition contribute to stress development on the nanocrystals.

5.5 Further Support from Raman Spectroscopy

We have also employed Raman spectroscopy to monitor the evolution of Si_{1-x}Ge_x nanocrystals as displayed in figure 5.4. In general, the first-order Raman spectrum of a Si_{1-x}Ge_x alloy consist of three main peaks due to nearest-neighbor Ge-Ge (300 *cm*⁻¹), Si-Ge (400 *cm*⁻¹), and Si-Si (500 *cm*⁻¹) stretching vibrations [93]. The latter is weak in Ge-rich alloys and is also masked by the intense peak coming from the Si substrate. Assuming random mixing in the alloy, from the relative integrated intensities of the Ge-Ge and Si-Ge peaks [67], the Ge composition of Si_{1-x}Ge_x structure can be found by using the equation 4.14. For the sample annealed at 1100 °C for 1 *h* the Ge content of *x* was found to be 0.65. This composition homogeneity changes by increasing annealing time, which can be interpreted as a phase separation. From the XRD measurements, the value of the 0.69 is obtained as given above. These two values obtained from Raman and XRD analysis are in agreement with each other. However based on assumptions in both techniques, estimating the Ge composition

has uncertainties. For instance as discussed in the previous section, XRD data predicts the presence of a strain in the nanocrystals opposed to the assumption made in the calculation of Ge composition by XRD.

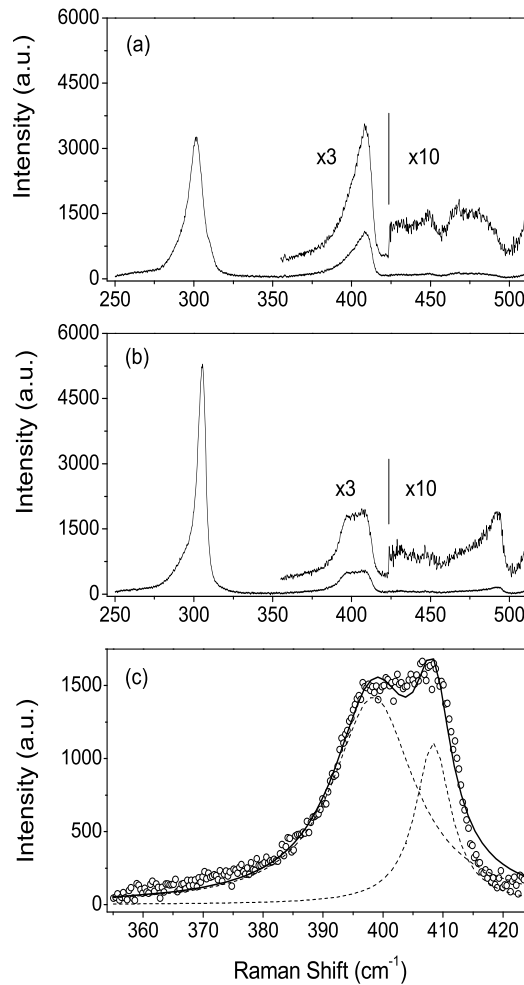


Figure 5.4: Raman spectra of the samples annealed at 1100 °C for 1 h (a), 3 h (b), and decomposed peaks of the Si-Ge vibration mode of the sample annealed at 1100 °C for 3 h (c).

As we know, there are three main factors that affect the Raman frequencies of the $\text{Si}_{1-x}\text{Ge}_x$ alloy, Ge content, stress, and phonon confinement effect. While relaxed $\text{Si}_{0.35}\text{Ge}_{0.65}$ alloy has Ge-Ge and Si-Ge vibration modes located at 293.4 and 406.3 cm^{-1} , respectively [65], in our sample annealed at 1100 °C for 1 h these are located at 301.5 and 408.7 cm^{-1} , respectively (figure 5.4 (a)). This shift towards higher wave numbers can result from the compressive stress on the SiGe nanocrystals due to the stretching of Si-Ge bonds with respect to relaxed SiGe occurring near the interface of

nanocrystals and SiO₂ matrix. As discussed early in XRD section, the stress resulted from volume expansion of SiGe during cooling down process can affect the Raman vibration modes as well. This effect will be more influenced in the sample for extended annealing. We note that, phonon confinement effect which is evident only for the crystallite sizes smaller than 10 nm, in our sample with the mean crystallite size of 22 nm, doesn't have significant effect on the shift of phonon modes.

Comparing Raman spectra of the samples annealed at 1100 °C for 1 and 3 h we see that, while the intensity of the Ge-Ge vibration mode increases and shifts to higher wave number, the intensity of the Si-Ge vibration mode decreases. More interestingly in the samples annealed for 3 and 5 h, the Raman peak has a flat top indicating the presence of inhomogeneous Si_{1-x}Ge_x structure consist of different compositions. The observed Raman peak can be approximately deconvoluted into two Lorentzian type peaks as shown in figure 5.4 (c). Regarding the shift of Si-Ge vibration mode toward lower wave numbers by increasing Ge content [66], we attributed the low energy side of the doublet located at 398.4 cm⁻¹ to the Ge-rich SiGe shell and the other at 408.4 cm⁻¹ to the Si-rich SiGe core. Enlarged peaks in the range of 420-470 cm⁻¹ appear in the Raman spectra of all c-Si_{1-x}Ge_x samples whether they are MBE or LPE grown, superlattices or single epitaxial layers, or bulk polycrystalline alloys. The weak peak located at 430 cm⁻¹ is generally assigned to another Si-Ge phonon peak, and the others observed at 450, 470 cm⁻¹ to localized Si-Si vibration mode in the neighborhood of three and two Ge atoms, respectively [64]. In the spectra of the sample annealed for 3 h these two latter peaks are weakened accompanied with the appearance of a relatively intense peak at 493 cm⁻¹, that is, Si-Si vibration mode with one neighboring Ge atom [64]. This phenomenon together with the decreased intensity of Si-Ge mode accompanied by increased intensity of Ge-Ge mode of the sample annealed for 3 h, and flat top feature of the Si-Ge signal all indicating strongly a phase separation in the SiGe nanocrystals when annealed for long enough time.

In this chapter, our attention is focused on the evolution of SiGe nanocrystals during high temperature annealing. It is clear from our data that early in the annealing SiGe nanocrystals are formed and their composition appears to be uniform, which

is in accordance with the observations of other groups [74, 75]. However, partial or complete separation of Si and Ge from each other takes place in the system upon extended annealing at the high temperature. We attribute this phase separation to the formation of a core-shell structure with a Si-rich SiGe core surrounded by a Ge-rich SiGe shell. When discussing the core-shell character of the SiGe nanocrystals we should take into account contribution of different factors. First of all, because of its larger size, Ge atoms would induce local strains inside the structure. Thus it would be energetically more favourable for Ge atoms to stay on the surface of the islands. Another factor that might give rise to the core-shell structure is that most of the Ge atoms are members of 5-number rings whereas all the Si atoms belong at least to one 6-number ring. Participation of Ge atoms in the surface of the islands suggest that the difference in the cohesive energy can partly be explained by the lower dangling bond energy, and thus also lower surface energy of Ge. Surface segregation of the Ge atoms in SiGe clusters has been studied by Tarus *et al.* by using two different simulation methods: continuous-space Monte Carlo and analytical potential molecular dynamics [76]. They found that the difference in atomic sizes, surface energy and elastic constants all contribute to the segregation effect, with the former two being more dominant. Furthermore, in a theoretical work, Asaduzzaman *et al.* [77] studied the electronic properties of (Si)Ge and (Ge)Si (core)shell nanoparticles by using density-functional tight-binding method. They showed that the former is more stable than the other because of the lower surface energy of the Ge compared with that of Si. Additional strong support for core-shell model can be provided by looking at the surface mobility of Si and Ge. Recently, Huang *et al.* [94] based on the first-principles calculations studied the surface mobility difference between Si and Ge and its effect on the growth of SiGe alloy films and islands. They showed that Ge surface diffusion is generally faster than Si and that the surface mobility of different species exhibits a strong dependence on strain. Further, they showed that the surface diffusion disparity between Si and Ge is greatly enhanced on the island surface compared to that on a smooth layer surface.

CHAPTER 6

OPTICAL CHARACTERIZATION OF THE Si NANOCRYSTALS EMBEDDED IN SiO₂ MATRIX IN WEAK QUANTUM CONFINED REGIME

This chapter is devoted to the photoluminescence properties of SiO₂/SiO₂: Si/SiO₂ sandwich films prepared by co-sputtering followed by a post annealing process. By fixing sputtering parameters, effects of annealing time and temperature on optical properties of the Si nanocrystals have been investigated. The nucleation and growth of the samples with the same sputtering parameters of $P_{Si} = 100\text{ W}$ and $P_{SiO_2} = 350\text{ W}$ were achieved by annealing sputtered samples at 900, 1000, and 1100 °C for times 1, 3, and 5 *h* in a quartz tube furnace under flowing N₂ gas at ambient pressure. The thickness of the films was about 350 *nm*. The room temperature PL has been done with the 532 *nm* line of Nd: YAG laser. Origin and evolution of the PL in weak quantum confinement regime are discussed in the light of X-ray diffraction (XRD), Fourier transform infrared (FTIR), and temperature dependent photoluminescence (TDPL) measurements. It has been found that for all the samples PL peaks tend to decompose to four Gaussian peaks originating from radiative defects in SiO₂ matrix, *nc*-Si/SiO₂ interface related localized defects, localized states in the amorphous Si band gap and quantum confinement of excitons in smaller nanocrystals. Considering the observation of intense luminescence and its decomposition tendency in nanocrystals with average sizes larger than exciton's Bohr radius the necessity to distinguish between the role of smaller and larger nanocrystals in the PL mechanisms has been discussed. Furthermore, possible origin of the interface related localized states in

particular Si=O double bonds in the *nc*-Si/SiO₂ interface have been discussed.

6.1 Quantum Confined Effect vs Interface Related Radiative Recombination

During the past two decades, great effort has been devoted to investigating the photoluminescence properties of Si nanocrystals embedded in SiO₂ matrix as these structures are candidates for a large number of optoelectronic and photonic applications [95]. Although the exact mechanism for light emission remains controversial, it is generally explained with two mechanisms. One is the defect related mechanism that appears mainly due to defects in SiO₂ matrix or in the interface between the nanocrystals and the surrounding SiO₂ matrix [96-99]. The other is the recombination of excitons confined in nanocrystals [97-105]. In recent years, the most general consensus is that defect related localized states at the interface and the quantum confinement of excitons both play important roles and the proper approach seems to be consider both of them rather than choosing one [106-112]. On the other hand, the nanocrystal-nanocrystal (NC-NC) interaction is an important factor in the overall luminescence spectrum. There are at least two fundamental mechanisms by which closely spaced nanocrystals can transfer energy between adjacent nanocrystals [111]. The first one is via tunneling of individual electrons or holes from one cluster to another [113]. The other interaction mechanism is the resonance energy transfer or Forster transfer, in which electron-hole pairs may migrate from smaller cluster to larger one by a dipole-dipole coupling. Some theoretical aspects of the Forster transfer in silicon quantum dots have been discussed recently [114].

Regarding the interface state effect as a function of Si nanocrystal size, some authors suggests that there is a critical nanocrystal size, below which the quantum confinement effect dominates, and above which the interface state effect prevails [107]. Wang et al. separated the interface state recombination effect from the quantum confinement effect in PL signals from the Si-rich oxide material containing Si nanocrystals with sizes of 2-3.5 nm [108]. Their observations revealed that the larger the size of Si nanocrystals and the higher the interface states density, the more beneficial for the in-

interface state recombination process to surpass the quantum confinement process. Simultaneous appearance of defect related and confinement related luminescence was first reported for single *c*-Si quantum wells by Kanemitsu *et al.* [115]. Deconvolution of the PL signals from multiple quantum wells, in which quantum confined related contribution is equal to or exceeds that of the defect related PL was also presented [116]. This effect was attributed to the tunneling of electron-hole pairs from Si nanocrystals within the quantum well layers into the amorphous grain boundary or into the Si/SiO₂ interface region due to coupling between the two observed radiative transition states. More recently Osinniy *et al.* demonstrated deconvolution of the PL signals due to bimodal size distribution of Si nanocrystals embedded into a SiO₂ matrix prepared by rf magnetron sputtering [105].

In the following sections, we present results of the studies carried out to separate the contribution of interfacial state recombination from quantum confined related recombination in PL spectra of the samples prepared by co-sputtering of Si and SiO₂ targets on Si substrate leading to the formation of nanocrystals with diameters larger than the exciton's Bohr radius. The interesting aspects of our results are the observation of more intense photoluminescence from nanocrystals with average size of larger than the exciton's Bohr radius and simultaneous observation of the two recombination processes. The simultaneous and relative contribution of quantum confined and interface related radiative emissions to PL spectra as a function of annealing time and temperature are investigated. We have shown the necessity to distinguish between nanocrystals with sizes below and above the exciton's Bohr radius instead of nanocrystals with specific mean diameter size. Furthermore, possible origin of the interface related localized states in particular Si=O double bonds in the *nc*-Si/SiO₂ interface have been discussed.

6.2 Annealing Treatment Evolution of the PL Spectra from Si Nanocrystals in Weak Quantum Confined Regime

Figure 6.1 shows the PL spectra of the as-grown and annealed samples. All samples exhibit a broad PL band between 550-1050 nm with line shape strongly affected by annealing temperature and time having obvious decomposition tendency. The size and surface chemistry of Si nanocrystals are two major factors affecting the PL spectra. Broadening of the PL is generally attributed to the size distribution of the nanocrystals. As can be seen from figure 1, the broad PL peak of the all annealed samples can be decomposed to four peaks located at 611-624 (peak *M*), 780-801 (peak *Q*), 894-913 (peak *I*) and 984-995 nm (peak *A*). To investigate in detail the evolution of the PL with annealing time and temperature deconvolution process applied to all PL spectra. To identify the origin and evolution of the PL with annealing parameters and distinguish between the role of quantum confinement effect and interface related emission, XRD, Raman spectroscopy, FTIR, and TDPL measurements have been performed.

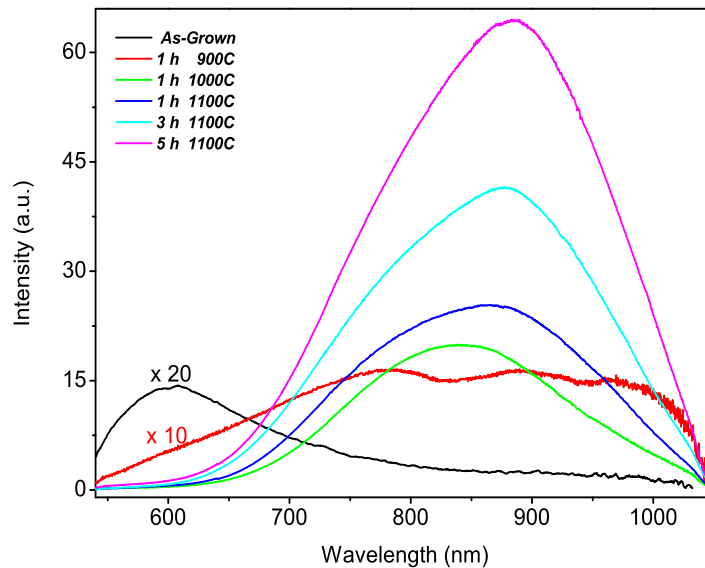


Figure 6.1: Room temperature PL spectra of the Si nanocrystals.

6.2.1 Annealing Treatment Evolution of the X-Ray Diffraction Spectra

Figure 6.2 shows XRD spectra corresponding to (111) diffraction peaks of the as-grown and the samples annealed at 900, 1000, and 1100 °C for 1 h and annealed at 1100 °C for 1, 3, and 5 h in the 2θ scans between 26-30° at 0.01 steps by a long acquisition time of 15 sec. At first sight, while the as-grown sample is amorphous and its spectrum doesn't show any feature, in those of annealed samples the corresponding (111) diffraction is observable. The first stages of the phase separation between Si and SiO₂ matrix starts at 900 °C, and small crystalline Si precipitates are formed within an amorphous SiO₂ matrix, which is characterized by its low intensity and broad XRD spectrum centered at 28.28°. By increasing annealing temperature up to 1000 °C and 1100 °C intensity of the peak increases and FWHM reduces, indicating the increased average size and improved crystallinity of the nanocrystals. The other feature is the shift of (111) diffraction peaks toward lower 2θ values by increasing annealing temperature. By using the corresponding 2θ values and Bragg's law, it was found that compared with bulk Si the lattice constant of the nanocrystals increases by increasing annealing temperature. This result indicates that Si nanocrystals are under strain, and that this effect is increased when larger nanocrystals have been formed. The strain in the nanocrystals varies from 0.004 to 0.006 and 0.008 by increasing annealing temperature from 900 °C to 1000 °C and 1100 °C, which mainly related to the misfit between bond lengths of the Si-Si and Si-O bonds in the *nc*-Si/SiO₂ interface. While in the sample annealed at 900 °C the agglomeration of Si clusters without well defined interface between nanocrystals and matrix take place, by increasing annealing temperature upto 1000 °C and 1100 °C larger nanocrystals with well defined interface formed. It has been shown that when a Si nanoparticle is oxidized and a Si-O-Si layer is formed on the surface, the Si-Si or Si-O-Si bonds are likely to weaken or break in some places because of the large stress at the *nc*-Si/SiO₂ interface. Then the Si=O double bond is more likely to form and stabilize the interface, since it requires neither a large deformation nor an additional element [96, 97, 118-120]. On the other hand, in the samples annealed at 1100 °C for 1, 3, and 5 h the shape and position of the XRD spectra is almost the same. This implies that annealing time doesn't affect the average

size and lattice constant of the samples.

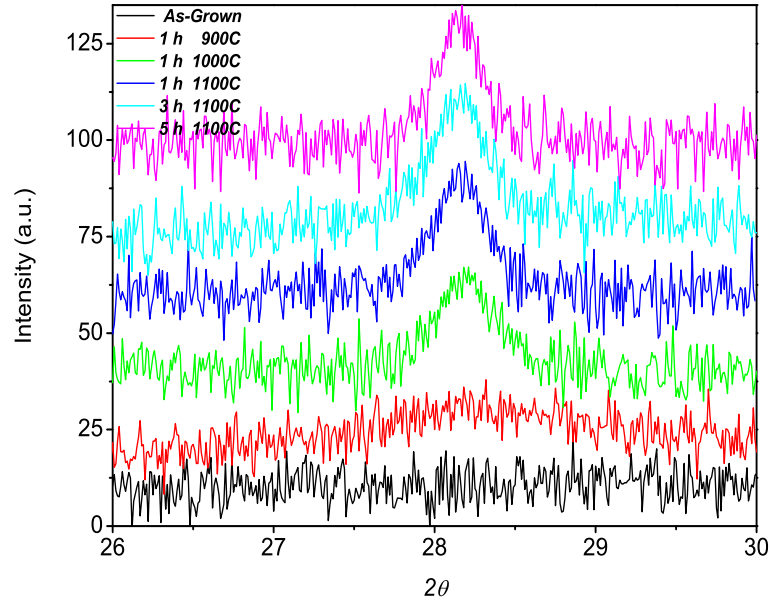


Figure 6.2: X-ray diffraction spectra of the Si nanocrystals.

By using XRD spectra and applying pseudo-Voigt function in the variance-range method, we can estimate the mean crystallite size D and the root-mean-square strain $\langle e^2 \rangle^{1/2}$ by the procedure mentioned in chapter 4. Besides the instrumental broadening correlation considered here, background and Cu $K\alpha 2$ line correlation have been applied as well. By increasing annealing temperature up to 1000 °C and 1100 °C, we have obtained the values of 2.5, 14, and 18 nm for mean crystallite size and 0.003, 0.005, and 0.008 for root-mean-square strain, respectively. For the samples annealed at 1100 °C for 3 and 5 h, we have obtained the same values of the sample annealed at 1100 °C for 1 h. This is in accordance with the result of the experimental and theoretical studies on the role of prolong annealing, in which the average size of the nanocrystals does not change although the size distribution of the nanocrystals evolves from Gaussian like to lognormal like [111, 117].

6.2.2 Annealing Temperature Evolution

As can be seen from figure 6.1, the broad PL peak of the all annealed samples can be decomposed to four peaks located at 611-624 (peak *M*), 780-801 (peak *Q*), 894-913 (peak *I*) and 984-995 nm (peak *A*). To investigate in detail the evolution of the PL with annealing time and temperature deconvolution process applied to all PL spectra. Figures 6.3(a-c) demonstrate the annealing temperature evolution of the samples annealed at 900, 1000, and 1100 °C for 1 h. The as-grown sample is homogeneous and fully amorphous material, without any evidence of phase separation between Si and SiO₂ (figure 6.2). Therefore, the observed luminescence in figure 6.1 located at 600 nm (with its high energy part has been cut off by the edge filter) is related to the radiative recombination centers in SiO₂ matrix. Sputtering process introduces many kinds of point defects into SiO₂, such as the *E'* center (O₃≡Si●), neutral oxygen vacancy (NOV) (O₃≡Si-Si≡O₃), non-bridging oxygen hole center (NBOHC) (O₃≡Si-O●), and dangling bonds (*p_b* center) (Si₃≡Si●). The densities of these defects may be different in as-grown samples, but will be changed usually reduced in different rates by thermal annealing. Some of these defects, such as NOV and NBOHC are radiative recombination centers or so-called luminescence centers (LCs). It is known that NBOHC in SiO₂ can emit light at 570-630 nm and many results of PL in SiO₂ ascribing them to NBOHC have been reported previously [121, 122]. The results obtained from FTIR measurements supporting the attribution of peak *M* to this radiative recombination centers will be discussed.

The first stages of the phase separation between Si and SiO₂ matrix starts at 900 °C and Si nanoclusters with average diameter sizes of 2.5 nm begin to form within an amorphous SiO₂ matrix and there is no well defined interface between the nanoclusters and the matrix. So for the sample annealed at 900 °C for 1 h (figure 6.3 (a)), although the main contribution to the PL spectra comes from the quantum confined related emission (peak *Q* 780 nm) the role of defect related radiative recombination centers in SiO₂ can't be ignored (peak *M* 624 nm). Its contribution in the samples annealed at higher temperatures decreases due to improved stoichiometry of the matrix. The peak *I* (900 nm) which we attribute it to the interface related localized

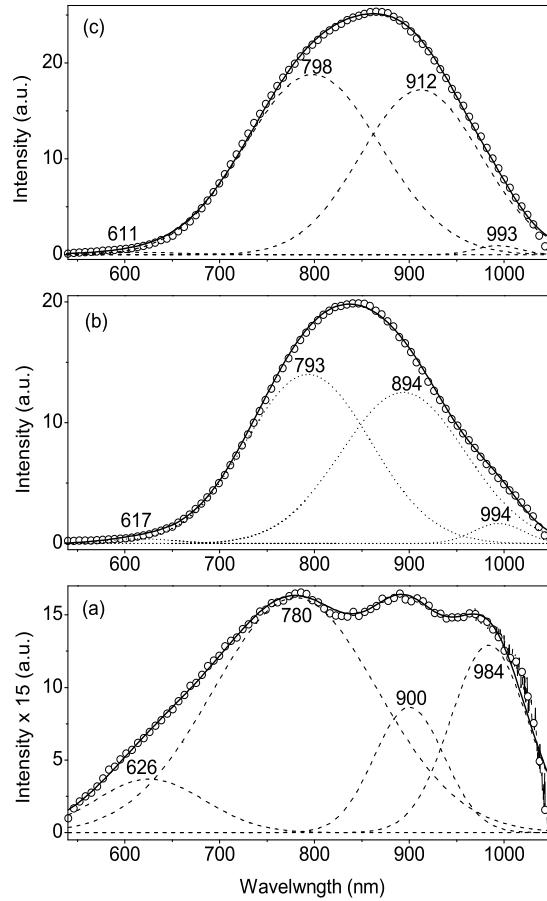


Figure 6.3: Decomposed PL spectra of the samples annealed at 900, 1000, and 1100 °C for 1 *h* (a-c) respectively.

states in larger nanocrystals and NC-NC interactions has small contribution to the PL spectra compared with that of annealed at higher annealing temperatures of 1000 and 1100 °C. On the other hand, the peak A (984 nm) which has been cut off by the edge filter is more pronounced in the samples annealed at lower temperatures of 900 and 1000 °C for 1 *h* in which the amorphous clusters still exist. From their Raman spectra (not shown here) two characteristic peaks around 480 and 150 cm^{-1} corresponding to the TO and TA modes of amorphous Si have been observed [123]. Annealing temperature evolution of the peak A is in accordance with the evolution of luminescence from weakly localized states in the amorphous Si band gap. It has been shown that the luminescence intensity and the confinement energy are stronger in the crystalline structure than in the amorphous structure. So for a given cluster size, the band gap

of *a*-Si is smaller than that of *nc*-Si [124]. The smaller band gap of *a*-Si can be explained by disorder-induced delocalized states (the extended states into the band gap) and the weakly localized states (the band-tail states). Mechanism of visible PL spectrum in *a*-Si nanostructure is often discussed in the light of spatial confinement (instead of quantum confinement) of carriers [125]. According to the spatial confinement model, recombination usually occur after the carriers are trapped in band-tail states, and the PL peak energy decreases with increasing the size of *a*-Si nanostructure. Some information about the recombination mechanism can be inferred from the temperature dependence of the PL spectrum.

By increasing annealing temperature up to 1000 and 1100 °C crystalline Si precipitates with average sizes of 14 and 18 nm accompanied with a well defined interface between the nanocrystals and the surrounding matrix have been formed. Obviously these sizes are larger than the exciton's Bohr radius and the observed intense PL can't be explained only by quantum confinement of excitons in Si nanocrystals. Actually this fact and different behavior of the different part of the PL line shape under annealing time and temperature lead us to distinguish between the role of nanocrystals with sizes smaller and larger than exciton's Bohr radius, and so the role of quantum confined and interface related luminescence. As can be seen from figure 6.3 (a-c), the evolution of peak *Q* (gradual redshift and increased intensity) is just like the temperature dependent evolution of excitons confined in Si nanocrystals.6-8 Therefore we attribute the peak *Q* between 780-801 nm to the exciton confined in Si nanocrystals with sizes smaller than the exciton's Bohr radius. It is worth noting that the emitted wavelength of peak *Q* shows small redshift by increasing annealing temperature, although there is a large increase in the size of nanocrystals. This is a characteristic behavior of a very dense distribution of nanocrystals, in which interaction among adjacent nanocrystals is very strong [126]. On the other hand the peak *I* between 894-913 nm redshifts as well, but its intensity is more affected by the annealing temperature. To investigate the light emission properties of the Si nanocrystals especially annealing evolution of the peak *I*, it is important to consider the effect of NC-NC interactions and that of interface related recombination centers.

The NC-NC energy transfer mechanism is important in the overall luminescence spectrum. For two neighboring nanocrystals with different sizes the excited carriers in the smaller nanocrystal having higher quantized energy levels, may relax either to the valance band of this nanocrystal or to the conduction band of the adjacent nanocrystal with a larger size. The transfer to the neighboring nanocrystal is more probable in the case where the nanocrystals are sufficiently close. In this case the smaller nanocrystals will inject their own excited carriers into the larger nanocrystals, in which radiative interband transition will subsequently take place. This mechanism is via tunneling of individual electrons or holes from one nanocrystal to another [113, 127] and is well known to occur in silicon clusters and forms the basis of silicon nanocrystal memories [128]. In other interaction mechanism due to dipole-dipole interaction between excitons in different nanocrystals, the electron-hole pairs may migrate throughout the nanocrystals without charge transfer [114]. More recently, Belyakov *et al.* by computer simulation showed that the PL spectrum of densely packed Si ensemble is strongly redshifted as a result of tunneling and Forster transfer [111]. They also showed that the two energy transfer mechanisms dominate the PL spectrum when the clusters are separated by less than 2 nm, and can still be significant in the case of Forster transfer over distances of 5 nm or more. On the other hand, when a Si nanoparticle is oxidized and a Si-O-Si layer is formed on the surface, the Si-Si or Si-O-Si bonds are likely to weaken or break in some places because of the large stress at the *nc-Si/SiO₂* interface. Then the Si=O double bond is more likely to form and stabilize the interface, since it requires neither a large deformation nor an additional element. In this model proposed by Wolkin *et al.* to explain the pinning of the band gap [106], it is indicated that the quantum confinement alone can explain the PL on porous nanocrystals larger than 3 nm, and the oxidation of the nanocrystal plays an important role as the nanocrystal sizes are smaller than 3 nm. However in another model suggested by Qin *et al.* [107], these two competitive processes take place in PL in which the oxidation states play a main role as the size of nanocrystal is larger than 3 nm, and the quantum confinement is dominant when the size of nanocrystal is smaller than 3 nm. The location and structure of such luminescent defects are still unclear and the region of the related emission depends on the preparation or simula-

tion methods. Nevertheless, it was suggested that the light-emitting centers from the $nc\text{-Si/SiO}_2$ material could be connected with double bonded Si=O defects [2-5, 14]. Pavesi *et al.* reported measurements of stimulated emission and light amplification in Si nanostructures and demonstrated optical gain. By observing the spectral coincidence of the emission band and the interface state absorption band, they suggested that radiative emission in Si nanocrystals occurs through a radiative state associated with the Si=O bonds in nanocrystal/oxide interface [97].

Here in our samples by increasing annealing temperature the density and size of the crystallized nanoclusters increase, and Si nanocrystals with average sizes larger than exciton's Bohr radius have been formed. In this regime the NC-NC interactions and the energy transfer between them play a key role in the overall luminescence spectrum. We simply assume that while the average size of nanocrystals is larger than exciton's Bohr radius, there exist nanocrystals with sizes smaller and larger than exciton's Bohr radius. We suggest that while some small nanocrystals contribute to the PL emission according to the radiative recombination of the excitons in quantum confinement model (peak Q) the others take part in energy transfer into the larger nanocrystals (peak I). It is worth noting that in the case of energy transfer from small nanocrystals to larger ones by direct tunneling of individual excited carriers, the higher levels of a larger nanocrystal overlap with lower levels of a smaller one, and then the carrier tunneling is resonant. In the case of mismatch between energy levels of adjacent nanocrystals, the carrier tunneling must be assisted by emission or absorption of phonons [111]. In other energy transfer mechanism known as Forster process, due to dipole-dipole interaction excitons migrate from smaller nanocrystals to larger ones without charge transfer. For thermally annealed Si implanted silica, it was suggested that excitons could migrate and be trapped in large nanocrystals [129]. More recently, Khriachtchev *et al.* proposed excitation of the interface related localized light-emitting centers (structures with Si=O bonds) by migrating excitons [130].

6.2.3 Annealing Time Evolution

For the samples annealed for 1, 3, and 5 *h* at 1100 °C, we have obtained the values of 17, 18, and 18 *nm* for mean crystallite size and 0.006, 0.005, and 0.003 for root-mean-square strain, respectively. In general, the formation mechanism for Si nanocrystals embedded in SiO₂ matrix goes through the familiar sequence of nucleation and growth, often followed by coarsening of nanocrystals due to Ostwald ripening process, where large nanocrystals grow on behalf of smaller which shrink. Although the number of nanocrystals with large sizes increases by prolong annealing, the average size of the nanocrystals remains almost the same [111, 117, 131]. In this case, we can expect a decrease in the number of nanocrystals having intermediate size accompanied by an increase in that of smaller ones (evolution from Gaussian like to lognormal like size distribution) [117]. Prolong annealing can remove nonradiative centers without increasing the nanocrystal size, and then the effect would be to cause an increased intensity and a redshift of the main PL spectra [111, 131]. This redshift is not due to increasing cluster size (as confirmed by XRD), but is due to the increased relative contribution of the peaks *I*. As can be seen from decomposed spectra (figs 6.3(a-c)), peaks *Q* and *I* are dominant features of the PL spectra and none of them show any explicit shift. However, the striking feature is the gradual increased intensity of the peaks *I* and exceeding that of peaks *Q*. This is an expected feature, because of the greater statistical probability for interface related localized light-emitting centers to occur on larger nanocrystals and also increased degrees of interaction between the nanocrystals. We would like to relate these interface related localized light-emitting centers to the structures with Si=O double bonds and will discuss in terms of FTIR results in SiO₂-sputtered and co-sputtered films. So, prolong annealing at 1100 °C leads to the relative increased contribution of peaks *I* (figs 6.3(a-c)) and 20 *nm* redshift of the whole PL signal. Recently, by computer simulation it has been demonstrated [111] that the effect of energy migration on the PL histogram of a silicon nanocrystal ensemble with a lognormal size distribution. The PL intensity was increased and redshifted as a result of tunneling and Forster energy transfer in densely packed ensemble.

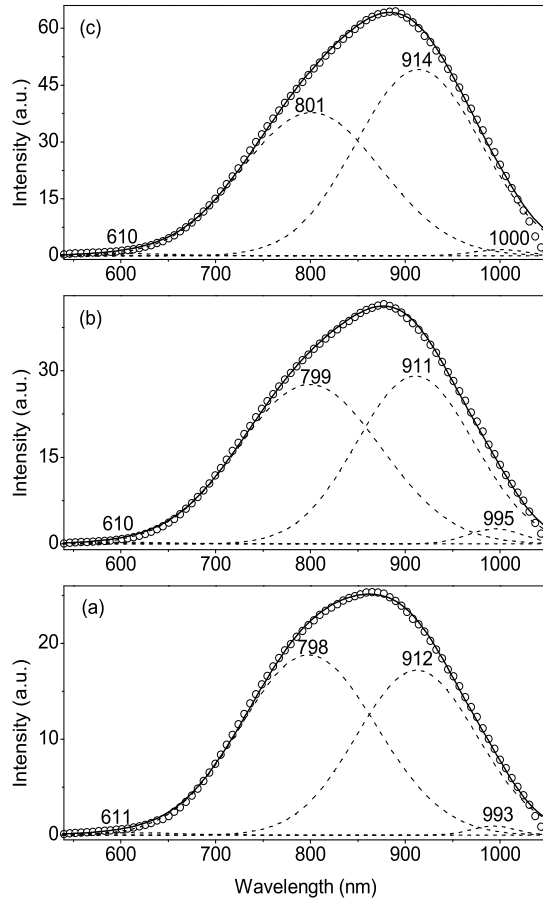


Figure 6.4: Decomposed PL spectra of the samples annealed at $1100\text{ }^{\circ}\text{C}$ for 1, 3, and 5 h (a-c) respectively.

6.3 Temperature Dependent PL Spectra from Si Nanocrystals

To more explore the radiative recombination mechanisms and justify the role of small and large nanocrystals, temperature dependent PL measurements were performed in the range between 33 and 300 K with an interval of 25 K . Figure 6.5 shows the temperature dependent PL spectra of the sample annealed at $1000\text{ }^{\circ}\text{C}$ for 1 h .

6.3.1 Temperature Dependent Evolution of the Integrated PL Intensity

Decomposition procedure has been applied to all PL spectra. Integrated intensity of the decomposed peaks and integrated intensity ratio of peak Q / peak I have been

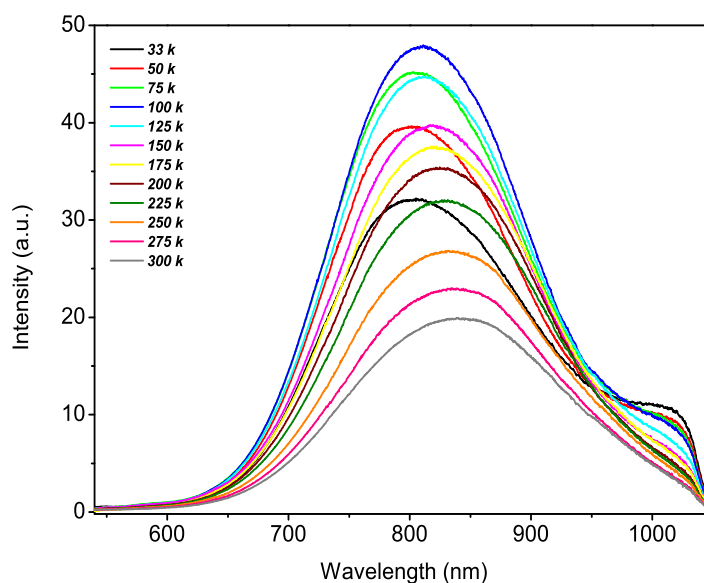


Figure 6.5: Temperature dependent PL spectra of the sample annealed at 1000 °C for 1 h.

shown in figure 6.6. As can be seen the integrated intensity of peak Q increases by increasing temperature up to 100 K, and then decreases with further increasing temperature. This anomalous temperature dependent behavior of PL intensity has been frequently reported by authors [113, 132-136] and is usually interpreted in terms of a threelevel system: the electronic ground state, a lower-energy triplet or dark (*i.e.*, optically forbidden) exciton state XD, and a higher-energy singlet or bright (*i.e.*, optically allowed) exciton state XB. Due to the exchange interaction between the electron and hole, the dark and bright excitons are separated by the exchange splitting Δ which is in the order of a tens of meV in Si nanocrystals in the nanometer size range. Because of dipole-forbidden radiative relaxation of lower-energy excitonic triplet states, the singlet-triplet splitting of excitons results in the thermal activation of radiative recombination processes. This effect associated with hopping/migration of charge carriers to nonradiative recombination centers and/or localized states in the interface was shown to result in an anomalous temperature dependence of the PL intensity exhibiting local maxima in the sub-100 K range.

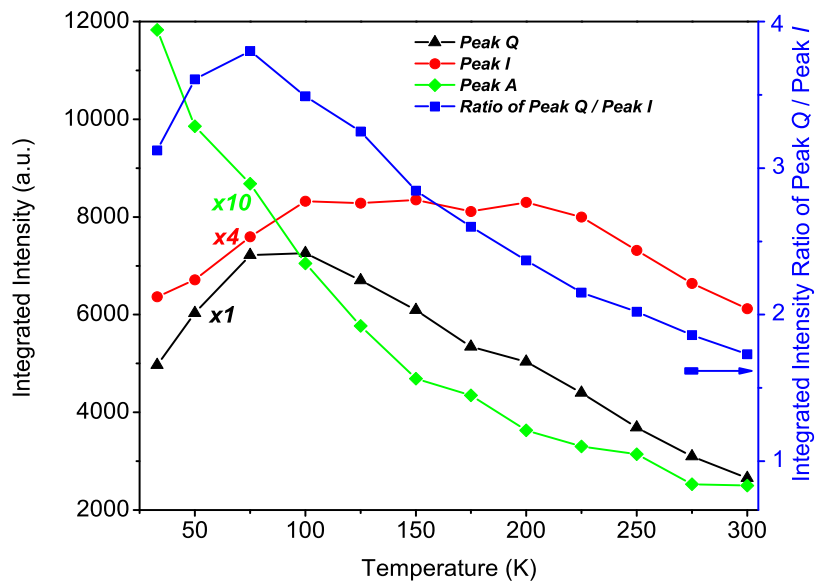


Figure 6.6: Integrated intensity of peak Q , peak I and peak A as a function of temperature and the ratio of peak Q / peak I .

At low temperatures, when migration effects are weak and thermally activated process is dominant, excitons are more localized within the smaller nanocrystals resulting in larger contribution of the peak Q . By increasing temperature up to 100 K, while the intensity of peak I increase slightly, the ratio of peak Q / peak I is increasing as well, *i.e.*, peak Q is still the dominant feature of the PL spectra. After 100 K, the nonradiative recombination channels activated by increasing temperature gives raise to the decreasing of the whole PL spectra (figure 6.5). On the other hand, while the integrated intensity of peak I is almost the same (up to 225 K), the relative contribution of peak Q decreases monotonically leading to the decreased peak Q / peak I ratio (figure 6.6). At higher temperatures in the range of 225-300 K, the nonradiative recombination channels being more activate lead to more decreased intensity of the whole peak and the decomposed peaks. It is worth noting that while the integrated intensity of peak I decreases, its relative contribution is increasing up to room temperature and approaches that of peak Q . The temperature dependency of the integrated intensity of peak Q is just like that of reported for confined excitons in Si nanocrystals, giving

another support to be attributed to the quantum confined related recombination.

6.3.2 Temperature Dependent Evolution of the PL Energy

Unlike the intense studies on temperature dependence PL intensity of the Si nanocrystals, there is a few reports published so far on the PL energy as a function of temperature. The evolution of the PL energy with the temperature can give information to know if the recombination is dominated by the quantum confinement or additional recombination mechanisms should be considered. For Si nanocrystals prepared by ion implantation, Brongersma *et al.* [133]. observed a monotonic shift (60 meV) of the peak position to lower energies when the temperature is increased from 12 to 300 K. That was almost equal to the band energy gap decrease of the bulk Si in the same temperature range, and attributed to the decrease in the band gap energy of the Si nanocrystals with temperature, and interpreted as an evidence for the quantum confinement effect in the observed PL. Heitmann *et al.* [113] reported 45 meV redshift in the PL peak position as the temperature increases from 4.5 to 300 K with a significant deviation from monotonic redshift reported by Brongersma *et al.* below 50 K. As a possible explanation, Heitmann *et al.* proposed the interaction between Si nanocrystals allowing the exciton migration from smaller nanocrystals to larger ones and the possibility of separation between quantum confinement and migration effects on the PL signal. More recently, Gardelis *et al.* [137] by studying different Si nanostructures in the form of porous Si and Si nanocrystals embedded in SiO₂ matrix stated that in order to explain the temperature evolution of the PL spectra one should consider not only quantum size effects in an ensemble of Si nanocrystals, but also the degree of interaction between the Si nanocrystals in the ensemble. They showed that by decreasing porosity the exciton migration becomes more important, and for the sample having lower porosity (higher degree of interconnection) reported 130 meV redshift of the PL in the temperature range from 70 up to 240 K which was much larger than the shift expected from the band gap shrinkage for bulk Si in the same temperature range (40 meV). For Si nanocrystals embedded in SiO₂ matrix (relatively isolated ensembles) they observed 18 and 10 meV redshift for tiny nanocrystals embedded in

SiO₂ and nanocrystal multilayers within SiO₂ respectively, which was much smaller than that of bulk Si. Figure 6.7 demonstrates the PL peak position evolution of the whole PL and the decomposed peaks as a function of temperature. As can be seen while the whole PL peak undergoes 75 meV redshift in the range of 33-300 K, the peak *Q* and *I* show 15 and 7 meV in the same range, respectively. Although the observed redshift for peak *I* is the half of that of peak *Q*, by increasing temperature the NC-NC interactions and migration effects being more important lead to the increased contribution of the peak *I* and so the decreased integrated intensity ratio of peak *Q* / peak *I*. We attribute the observed 75 meV redshift of the whole peak mainly to the relative increased contribution of the peak *I*, indicating the necessity of considering the interface related recombination mechanisms together with quantum confinement related mechanisms.

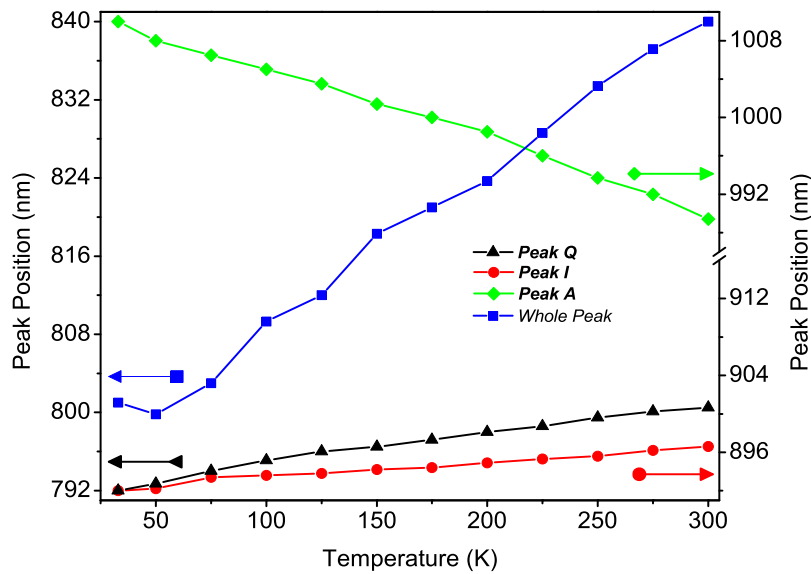


Figure 6.7: Temperature dependent evolution of the peak position of peak *Q*, peak *I*, peak *A*, and whole peak.

Finally we discuss the temperature dependent properties of the PL emission around 950-1050 nm (peak *A*). In the previous section we attributed peak *A* to the radiative recombination of carriers at the band-tail states in a-Si nanostructures inside co-

sputtered layer. Although the origin of this peak has been attributed to the structural disorder of the bulk a -Si phase [138] or to the delocalized recombination in c -Si region adjacent to the wide-gap (visible emitting) region [139], beside their annealing treatment evolution, the temperature dependent PL measurement provides another evidence that the light emission results from band tail states of the a -Si nanoparticles. By increasing temperature from 33 to 300 K it shifts toward higher energies accompanied with an exponential like continuous decrease in its intensity, but observable even at room temperature (figures 6.5, and 6.6). Kanemitsu *et al.* [140] in a study on the temperature dependent photoluminescence from crystalline and amorphous silicon nanostructures demonstrated that while in bulk a -Si and bulk c -Si the near-infrared PL disappears at temperatures above 150 K , the spreading of the band-tail state (blueshift of the lowest energy of carriers in band-tail states) reduces the thermal quenching of the PL intensity in a -Si nanostructures and PL is observed even at room temperature. We discuss the observed blue shift and decreased intensity of peak A in the temperature range of 33-300 K as follow: At low temperatures, the photoexcited electrons and holes thermalize rapidly in the extended states on a ps -timescale to the mobility edges from where further thermalization can only occur by tunneling transitions to localized states at lower energy (energy-loss hopping). Radiative recombination occurs by radiative tunneling between the band tails of the conduction and valence bands while the competing non-radiative channel is associated with tunneling from the band tail into the defects (dominantly deep lying states and differently charged Si dangling-bond states). When the temperature increases, owing to the enhanced mobility of the carriers in the band tail, tunneling to higher lying band-tail states becomes increasingly important and some of them are thermally excited to the extended state [141]. The mobile carries in the extended state are captured at the nonradiative recombination centers and the photoluminescence is quenched. By further increasing temperature up to room temperature, more carriers are excited into the extended states leading to the more decrease of the PL intensity. On the other hand according to the spatial confinement model [125] for PL mechanism in a -Si nanostructures, while the effect of size-dependent luminescence from amorphous semiconductor nanostructures is similar to the effects of quantum confinement, it is instead

due to the statistics of spatial confinement. Carriers are localized into band-tail states whose density increases monotonically from the midgap up into the band. It is the statistics of lowest energy states within a volume that causes luminescence energy to increase as volume decreases. So, by more increasing temperature the more carriers tunneling to upper lying band-tail states leads to the spatial confinement of carriers in a smaller volume therefore blue shift of the related emission is observed.

6.4 Si=O Double Bonds in the Interface, Further Support by FTIR Spectroscopy

To identify structural damage to the SiO₂ network caused by co-sputtering and its reconstruction by annealing treatments, and also to determine the relation between radiative defect characteristics and the observed PL, FTIR spectra were measured. Figure 6.8 shows the absorption spectra of the as-grown and annealed co-sputtered SiO₂/ Si: SiO₂/ SiO₂ samples in the range of 700-1350 cm^{-1} . The well-known absorption modes, which correspond to the symmetric stretching (SS, near 800 cm^{-1}) and asymmetric stretching (AS, near 1084 cm^{-1}) modes of the Si-O-Si bridge are shown [54, 142]. These frequencies can vary with the preparation techniques, for example the latter one varies between about 1086 cm^{-1} for thermally grown SiO₂ to about 1055 cm^{-1} for SiO₂ deposited by low-temperature PECVD techniques. For the reference sample without excess Si (only SiO₂ sputtered film) with the same thickness of the co-sputtered samples it appears at 1062 cm^{-1} (figure 6.9). Annealing treatments improves their stoichiometry and the asymmetric stretching mode shifts toward higher wave numbers approaching that of thermally grown SiO₂ films. Compared with the SiO₂ sputtered sample, this mode shifts markedly toward lower wave numbers (1037 cm^{-1}) and its full width at half maximum (FWHM) becomes broader in the as-grown co-sputtered sample. On the other hand, another peak appearing at 880 cm^{-1} has been annealed out during the heat treatment. These results indicate that the as-grown co-sputtered sample is more off stoichiometric and thus many kinds of point defects have been formed, which some of them such as NOV and NBOHC are radiative recombination centers. The 880 cm^{-1} absorption mode has been discussed in the literature as a mode related to NBOHC situated on Si₆ rings as the origin of

luminescence signal at 570-630 nm [55, 56] and disappears at temperatures above 900 °C [57]. In our samples by increasing annealing temperature, the stoichiometry of the matrix has been improved leading to annealing out of the NBOHC defects accompanied by the decrease in the intensity of the peak *M* in the PL spectra. On the other hand, for annealed co-sputtered samples specially those annealed at 1100 °C for prolong times of 3 and 5 h, in the low wave numbers side of the main Si-O-Si asymmetric stretching band a shoulder appears which has been attributed to the deep level defect states arising from Si dangling bond defects (p_b center) [58]. These defects exist in the *nc*-Si/SiO₂ interface which can be neutral, positively, or negatively charged [111]. Theoretically it has been founded that the carrier trapping at neutral p_b centers is nonradiative, whereas capture at charged centers can lead to photon emission at energies smaller than the bandgap of bulk silicon [143]. Some experimental studies ascribing the broad infrared emission band at 0.8-0.9 eV to the recombination of carriers trapped at Si dangling bonds have been reported [101].

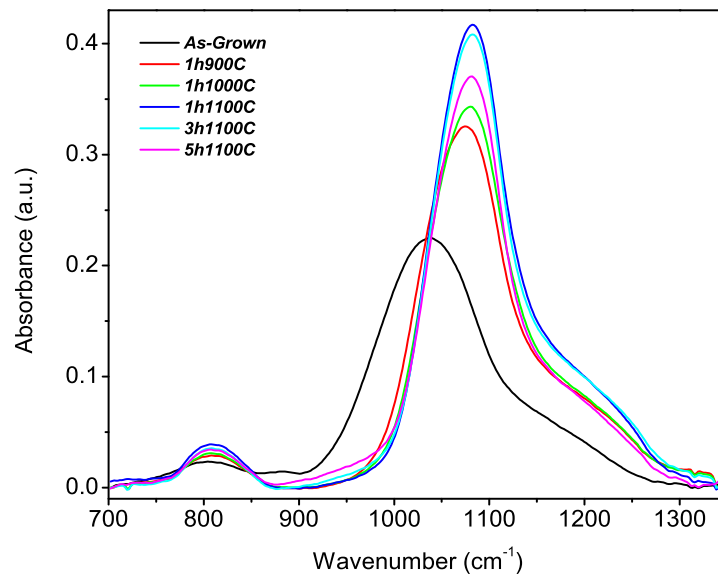


Figure 6.8: Effect of annealing treatments on the FTIR spectra of the co-sputtered SiO₂/ Si: SiO₂/ SiO₂ samples.

In the following we discuss the annealing evolution of the Si-O-Si asymmetric stretch-

ing mode (AS, near 1084 cm^{-1}) in SiO_2 -sputtered and co-sputtered samples together with that of PL spectra and present a discussion which can be interpreted as existence of the oxygen related Si=O double bonds. Figure 6.8 shows the effects of annealing time and temperature on the FTIR spectra of the co-sputtered samples. There are three modifications to the Si-O-Si asymmetric stretching band with increasing annealing temperature from $900\text{ }^\circ\text{C}$ to $1100\text{ }^\circ\text{C}$: (1) the position of the peak shifts from 1074 cm^{-1} to 1084 cm^{-1} approaching that of thermally grown SiO_2 film, (2) the characteristic shoulder on the high-frequency side of the band increases, and (3) the FWHM decreases. On the other hand in the samples annealed at $1100\text{ }^\circ\text{C}$ for 1, 3, and 5 h, while the position of the main AS mode doesn't change by annealing time, its intensity has decreased. The same trend has been observed for the SiO_2 -sputtered films, with two differences: (1) the FWHM of the main peak has been increased in co-sputtered samples (for example in samples annealed at 1100 for 1 h, 82 cm^{-1} vs. 69 cm^{-1}) and (2) the characteristic shoulder on the high-frequency side of the band is more intense in co-sputtered samples (figure 6.9). For fused silica the AS mode represents a main absorption band located at 1075 cm^{-1} corresponding to the wave number position of the asymmetric stretching transverse optical vibration mode (AS1TO) of the Si-O-Si bridge when two adjacent O atoms move in phase [54]. The position of the AS1TO mode is directly related to the average Si-O-Si bond angle, which is equal to 144° in the case of fused silica, and the FWHM (65 cm^{-1}) is related to the distribution of Si-O-Si angles. For our samples the peak position of the AS1TO is almost the same in SiO_2 -sputtered and co-sputtered sample, indicating the same average bond angle. Nevertheless, broadening of the FWHM in co-sputtered samples indicates a larger angle distribution of Si-O-Si bridges compared with SiO_2 -sputtered samples.

The more striking difference is the increased intensity of the characteristic shoulder on the high-frequency side of the band in the co-sputtered samples. This shoulder corresponds to the asymmetric stretching mode of vibration of the Si-O-Si bridge when two adjacent O atoms move out of phase (AS2TO) and has been attributed to coupled modes induced by disorder and its intensity provides then an estimation of disorder [54]. Based on quantum chemical calculations, Gole *et al.* suggested that a portion of the FTIR spectrum for a heavily oxidized porous silicon in the range 1100-1300

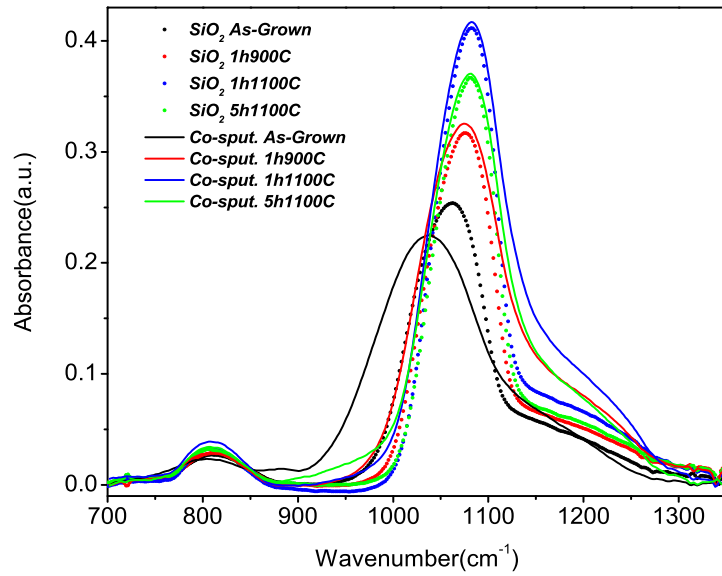


Figure 6.9: Comparison between FTIR spectra of the SiO₂-sputtered and co-sputtered SiO₂/Si: SiO₂/ SiO₂ samples under the same annealing treatments.

cm^{-1} can be reassigned to the Si=O stretching mode of the silanone-based oxyhydrides [60]. In an important study on oxidized porous silicon Wolkin *et al.* demonstrated that when nanocrystalline Si is oxidized and a Si-O-Si layer is formed on the surface, the Si-Si or Si-O-Si bonds are likely to weaken or break in many places because of the large stress at the Si/SiO₂ interface [106]. A Si=O double bond is more likely to be formed and stabilize the interface, since it requires neither a large deformation energy nor an excess element. The knowledge gained from these studies specially pinning of the optical band gap due to the Si=O double bonds at the interface, leads to a load of studies on the *nc*-Si/SiO₂ interface (whose bonding energies are a function of nanocrystal size) [96, 98, 108] since it is widely believed that the interface plays a crucial role on the optical and electrical properties of the Si nanocrystals embedded in SiO₂ matrix. By using Quantum Monte Carlo (QMC) calculations for small nanocrystals and interpolating to the bulk band gap, it has been shown that while one Si=O bond will produce a defect level only for nanocrystal diameters below 2.4 nm, multiple Si=O bonds will lead to the emergence of deep-lying states for large

nanocrystal sizes [106]. It is also found that the shell region around Si nanocrystals bordered by SiO₂ consists of the three Si suboxide states, Si¹⁺, Si²⁺, and Si³⁺, whose densities are also strongly dependent on nanocrystal size. The Si=O bonds that are responsible for optical band gap pinning exist mostly in the outer interface of the shell, indicating that the oxidation state of Si in the Si=O bonds is close to +3 [144]. In a study on the optical properties and emission characteristics of hydrogenated and oxidized Si nanoparticles Li *et al.* by applying density-functional tight-binding method indicated that Si=O bond on the surface of Si nanoparticles can stabilize the excited state and that most of the gaps in the excited state configuration fluctuate within a narrow range of 2.55- 3.01 and 0.52-1.33 eV without and with the Si=O bond on the surface, respectively [145].

Taking into account the above theoretical and experimental reports on the role of Si=O bonds in the interface and the results we have obtained by room temperature PL and TDPL accompanied by the comparison between FTIR spectra of the SiO₂-sputtered and co-sputtered samples confirms that the portion of the shoulder in the range of 1100-1300 cm⁻¹ in co-sputtered samples represents the experimental observation of the Si=O bonds in structures containing Si nanocrystals embedded in SiO₂ matrix. These bonds play a crucial role in the PL peak *I* in which we attributed to the energy transfer from smaller nanocrystals to larger ones with sizes beyond exciton's Bohr radius. Annealing time and temperature evolution of the peak *I* can be well described in the light of XRD results, energy transfer between nanocrystals, and existence of Si=O bonds in the *nc*-Si/SiO₂ interface. By increasing annealing temperature from 900 to 1100 °C, the average size of the nanocrystals increases from 3 to 18 nm. While in the sample annealed at 900 °C the agglomeration of Si clusters without well defined interface between nanocrystals and matrix takes place, by increasing annealing temperature up to 1000 and 1100 °C larger nanocrystals with well defined interface containing Si=O bonds formed to stabilize the Si nanocrystals and lower the strain in the system. We attribute the observed redshift of the peak *I* by increasing annealing temperature to the increased number of the Si=O bonds which leads to the formation of deep-lying states for larger nanocrystals. Increased intensity of the peak *I* can be explained by the increased density of the nanocrystals by raising annealing

temperature up to 1100 °C, and therefore increased probability of the energy transfer between the nanocrystals. On the other hand, by a prolong annealing at 1100 °C the average size of the nanocrystals dose not change and as discussed above the size distribution of the nanocrystals evolves from Gaussian like to lognormal like. The effect would be the reason for the more increased intensity of peak *I* due to increased degree of interaction between the nanocrystals. We note that while by prolong annealing the peak position of the peak *I* doesn't change (figure 6.4 (a-c)), the peak position of the whole PL spectra redshifts from 865 to 885 nm due to increased relative contribution of the peak *I* with respect to peak *Q*.

6.5 Influence of Annealing Time and Temperature on the TDPL of the Si Nanocrystals

The most part of this chapter is devoted to the influence of the annealing time and temperature to the room temperature photoluminescence from Si nanocrystals in weak quantum confined regime. Observation of intense luminescence from Si nanocrystals with sizes larger than Bohr radius, decomposition tendency of the PL spectra and different behavior of the decomposed peak leads us to distinguish between the role of nanocrystals with sizes above and below the Bohr radius. We discussed above the possible origins of the PL mechanisms. By deconvolution of the PL peaks to four Gaussian peaks, we attributed them to radiative defects in SiO₂ matrix, *nc*-Si/SiO₂ interface related localized defects, localized states in the amorphous Si band gap and quantum confinement of excitons in smaller nanocrystals. One of the stronger support to our idea was the temperature dependent PL measurement applied on the sample annealed at 1000 °C for 1 *h*, in which the temperature dependent evolution of integrated intensity and emission energy served the ability to distinguish between the quantum related and interface related luminescence.

The temperature dependent PL applied on the samples annealed 900 °C for 1 *h*, annealed at 1100 °C for 1 *h*, and annealed at 1100 °C for 5 *h* as well. Figures 6.10-6.12 demonstrate the PL spectra of these samples. As can be seen, there is similarities and

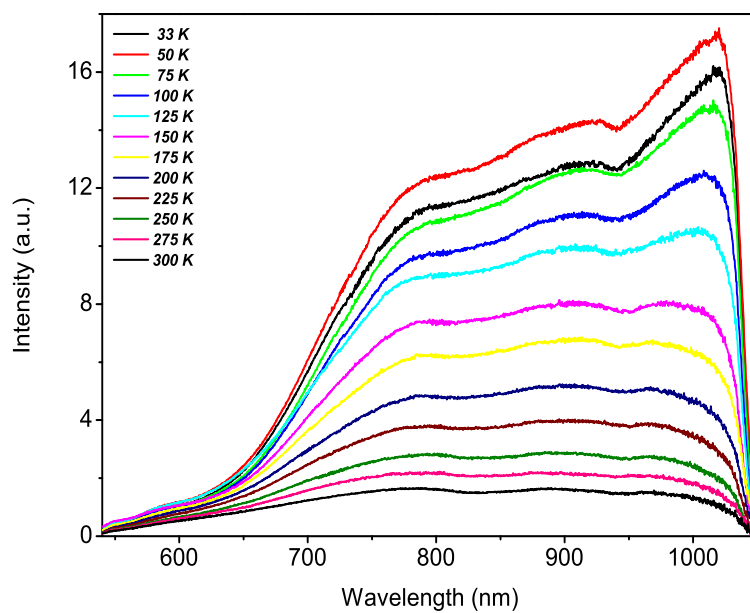


Figure 6.10: Temperature dependent PL spectra of the sample annealed at 900 °C for 1 *h*.

differences between different part of the spectra. Deconvolution processes of these samples is in progress and influence of the annealing time and temperature on the temperature dependent evolution of the emission energy and integrated intensity of the TDPL spectra will be discussed.

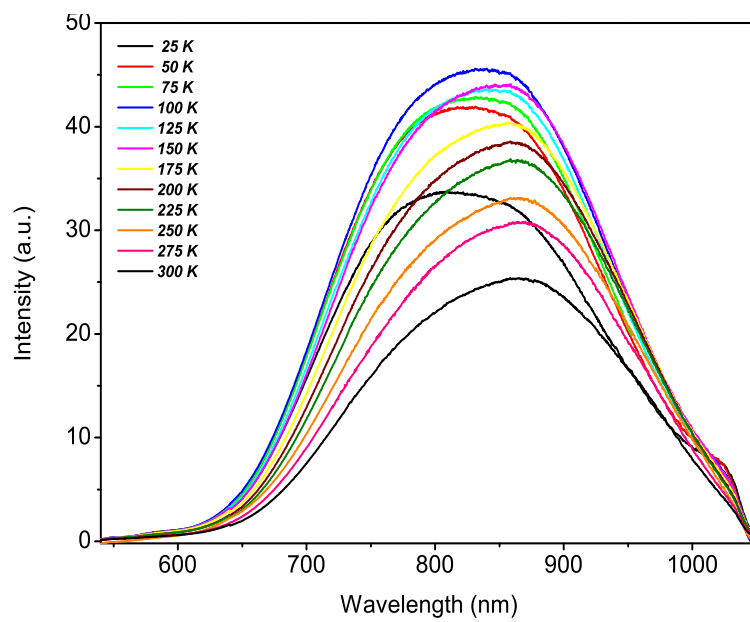


Figure 6.11: Temperature dependent PL spectra of the sample annealed at 1100 °C for 1 *h*.

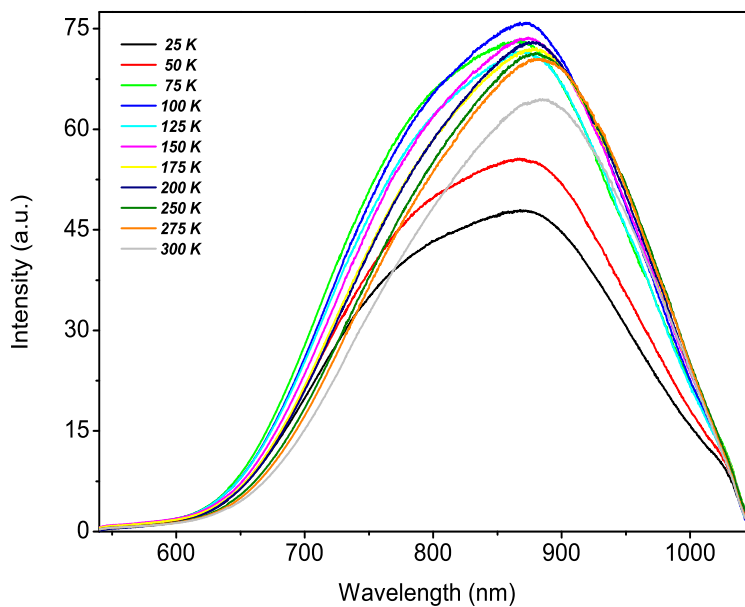


Figure 6.12: Temperature dependent PL spectra of the sample annealed at 1100 °C for 5 *h*.

CHAPTER 7

OPTICAL CHARACTERIZATION OF THE $\text{Si}_{1-x}\text{Ge}_x$ NANOCRYSTALS EMBEDDED IN SiO_2 IN WEAK QUANTUM CONFINED REGIME MATRIX

7.1 Motivation

During the past two decades, great effort has been devoted to investigating the photoluminescence (PL) properties of nanometer size Si and Ge crystals [68, 146, 147]. In particular, many studies have been performed for Si nanocrystals (*nc*-Si) because of their potential application to Si-based optoelectronic devices. A high-energy shift of the PL peak and an increase in the PL intensity with decreasing size have commonly been observed in the near-infrared (NIR) to red regions [148-151]. In contrast to *nc*-Si, there are few reports on the clear size dependence PL for Ge nanocrystals (*nc*-Ge) [152, 153]. Many authors claimed that *nc*-Ge samples exhibit a PL peak around 2.2 eV independent of the size and some authors related that to the defects in SiO_2 matrix or in the interface between the nanocrystals and the surrounding SiO_2 matrix [154-157]. Although the exact mechanism for light emission remains controversial, the most general consensus is that defect related localized states at the interface and the quantum confinement of excitons both play important roles and the proper approach seems to be consider both of them rather than choosing one [106-112].

As for pure *nc*-Si and *nc*-Ge, in the case of nanometer size $\text{Si}_{1-x}\text{Ge}_x$ alloy crystals (*nc*- $\text{Si}_{1-x}\text{Ge}_x$), the quantum confinement of carriers is expected to play an important

role in determining the optical response. Few studies of photoluminescence from the $\text{Si}_{1-x}\text{Ge}_x$ nanocrystals have been reported [158, 75]. Fujii *et al.* [75] observed near-infrared photoluminescence from $\text{Si}_{1-x}\text{Ge}_x$ alloy nanocrystals as small as 4-5 nm and with Ge content of x between 0-0.3 prepared by rf co-sputtering. They stated that since the energy band structure of bulk $\text{Si}_{1-x}\text{Ge}_x$ alloy crystals strongly depends on x , that of $nc\text{-Si}_{1-x}\text{Ge}_x$ should depend on x as well as the particle size. So, they concluded that the band gap energy of $nc\text{-Si}_{1-x}\text{Ge}_x$ will change continuously from the widened band gap of $nc\text{-Si}$ to that of $nc\text{-Ge}$ with increasing x , and claimed that the PL arises from the radiative recombination of excitons confined in $\text{Si}_{1-x}\text{Ge}_x$ nanocrystals.

On the other hand, various calculations suggest strong confinement in Ge and thus a critical particle size, below which the band gap of germanium becomes larger than that of silicon [159-161]. Experimentally, Bostedt *et al.* by using x-ray absorption spectroscopy showed that in the range of investigated particle sizes the quantum size effects of Ge nanocrystals are always stronger compared to Si particles of similar size [162]. More recently, Pan *et al.* [163] investigated the band-gap expansion of Si and Ge nanocrystals in terms of the bond order-length-strength correlation. It was shown that the bond order deficiency of surface atoms dictates electron-phonon coupling and crystal binding, and enhances the size dependence of the observed blue shift in photoemission and photoabsorption of Si and Ge nanocrystals. Compared with Si, Ge nanocrystal exhibits stronger electron-phonon coupling due to larger phonon-induced deformation of the crystal lattice.

In the previous chapter, we studied the simultaneous evolution of quantum confined and interface related luminescence in Si nanocrystals with average sizes larger than the excitons Bohr radius (weak quantum confined regime) [164]. The observed intense luminescence and line shape evolution of different part of the PL spectra by annealing time and temperature at room temperature and temperature dependent photoluminescence, lead us to distinguish between the role of nanocrystals with sizes smaller and larger than the excitons Bohr radius. While in smaller nanocrystals quantum confined effects is dominant, in larger nanocrystals interface related features play key role. In this chapter, we present the PL results from the $\text{Si}_{1-x}\text{Ge}_x$ nanocrystals

embedded SiO₂ layer with sizes between the Bohr radius of excitons in Si (4.9 nm) and Ge (24.3 nm) and with a larger Ge content of x between 0-0.85. We will discuss luminescence mechanisms in terms of radiative defects in SiO₂ matrix, nc -SiGe/SiO₂ interface related localized states, localized states in the a -Si and / or a -SiGe band gap and quantum confinement of excitons in smaller nanocrystals [165].

7.2 Experimental Details

Si_{1-x}Ge_x nanocrystals with a large range Ge content of x between 0-0.85 embedded in SiO₂ matrix were prepared by co-sputtering and post annealing in N₂ ambient. By fixing sputtering power of SiO₂ and Si targets, four sets of samples with Ge power of 0, 5, 10, and 20 W subjected to the same isochronal and isothermal annealing treatment. For each set the effect of annealing time and temperature on the PL spectra have been investigated. Origin and evolution of the photoluminescence (PL) in weak quantum confinement regime are discussed in the light of transmission electron microscopy (TEM), X-ray diffraction (XRD), and Fourier transform infrared (FTIR) measurements. It was found that for all the samples PL peaks tends to decomposed four Gaussian peaks originating from radiative defects in SiO₂ matrix, nc -Si_{1-x}Ge_x/SiO₂ interface related localized defects, localized states in the amorphous Si and/or SiGe band gap and quantum confinement of excitons in smaller nanocrystals. Considering the observation of intense luminescence and its decomposition tendency in nanocrystals with average sizes larger than exciton's Bohr radius the necessity to distinguish between the role of smaller and larger nanocrystals in the PL mechanisms has been discussed.

We have prepared SiO₂/SiO₂: Si: Ge/SiO₂ sandwich films embedded on Si substrate by rf magnetron co-sputtering method with powers of $P_{SiO_2} = 350$ W, $P_{Si} = 100$ W, and $P_{Ge} = 0, 5, 10,$ and 20 W. The bottom SiO₂ layer with the thickness of about 40 nm was deposited on Si to restrain Ge atoms from growing epitaxially on the Si substrate in the post-annealing process. The top SiO₂ layer with the thickness of about 40 nm was deposited to impede the diffusion of Ge atoms out of the surface.

The thickness of the co-sputtered layer was fixed for all the samples (about 270 nm). The typical deposition rate was 4 nm/min. By fixing deposition parameters of the Si and SiO₂ and varying that of Ge target, measurements have been performed to study the effect of Ge content on the annealing time and temperature evolution of the PL spectra. The XPS depth profile of the as-grown sample is carried out to obtain the relative elemental concentration. Equipping Specs XPS system at a vacuum of 1×10^{-7} Pa depth profiles of Si, Ge, O, and C atoms were recorded. After three time sputtering with 2000 eV Ar⁺ ions with the cycle of 2 min followed by a 4 min 3500 eV sputtering of the as-grown samples with $P_{Ge} = 6, 10, \text{ and } 20$ W, the steady state elemental composition values of 6.7, 40.5, 52.8, and 0; 9.1, 39, 51.9, and 0; 19, 32.9, 48.1, and 0 have been obtained for Ge, Si, O, and C atoms, respectively.

After deposition, wafers were cleaved and annealed in a quartz tube furnace under flowing N₂ gas at ambient pressure for times (t) varying between 1-5 h at 900, 1000, and 1100 °C. In general, the formation mechanism for SiGe nanocrystals embedded in SiO₂ matrix goes through the familiar sequence of nucleation and growth, often followed by coarsening of nanocrystals due to Ostwald ripening. The formation and evolution of SiGe nanostructures were studied by cross-sectional high-resolution electron microscope [JEOL2010F]. The structural and compositional properties of the samples examined by XRD and Raman spectroscopy measurements by the procedure explained in chapter 4. The room temperature PL and TDPL measurements have been done by the 532 nm line of Nd: YAG laser. FTIR spectroscopy was measured using Equinox spectrometer (Bruker), in the absorbance mode at wavenumbers between 400-4000 cm⁻¹ with a resolution of 2 cm⁻¹.

7.3 Annealing Treatment Evolution of the PL Spectra from the Samples with $P_{Ge} = 0$ W (Si Nanocrystals)

Figure 7.1 shows PL spectra of the samples with $P_{Ge} = 0$ W (Si nanocrystals) annealed at 900, 1000, and 1100 °C for 1 h and annealed at 1100 °C for 1, 3, and 5 h. All samples exhibit a broad PL band between 480-1050 nm at room temperature.

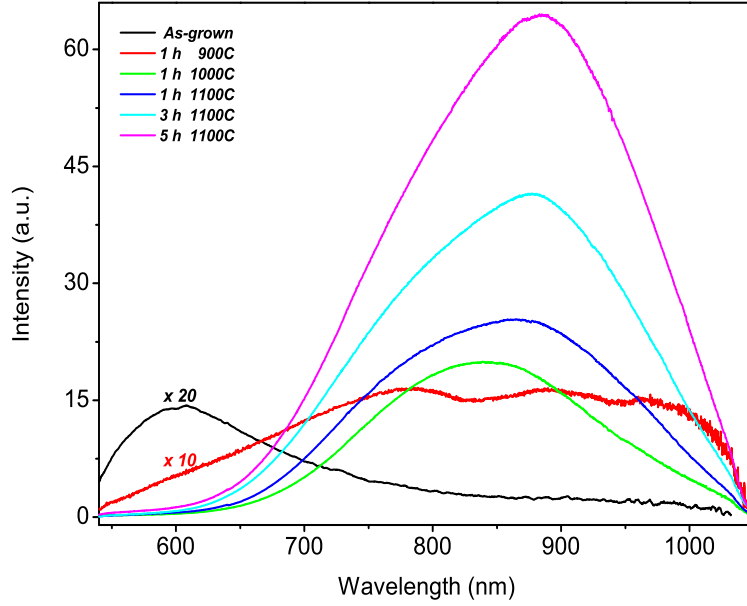


Figure 7.1: Annealing treatment evolution of room temperature PL spectra of the samples with $P_{Ge} = 0 W$ (Si nanocrystals).

All spectra tend to be decomposed four Gaussian peaks (peak M (750-780), peak I (750-780), peak A (750-780), peak Q (750-780)), in which we attributed them to radiative defects in SiO_2 matrix, $nc\text{-Si/SiO}_2$ interface related localized defects, localized states in the amorphous Si band gap and quantum confinement of excitons in smaller nanocrystals, respectively (figure 7.2). In our previous work we discussed in detail on the annealing temperature, annealing time, and temperature dependent photoluminescence (emission energy and integrated intensity) evolution of the four recombination mechanism. Regarding that the nanocrystal sizes were above the exciton Bohr radius, we discussed about the necessity to distinguish between the role of nanocrystals with sizes above and below the exciton Bohr radius. The details are given in previous chapter and here we have shown the decomposed peaks to have a comparison with that of samples prepared by different $P_{Ge} = 5, 10,$ and $20 W$.

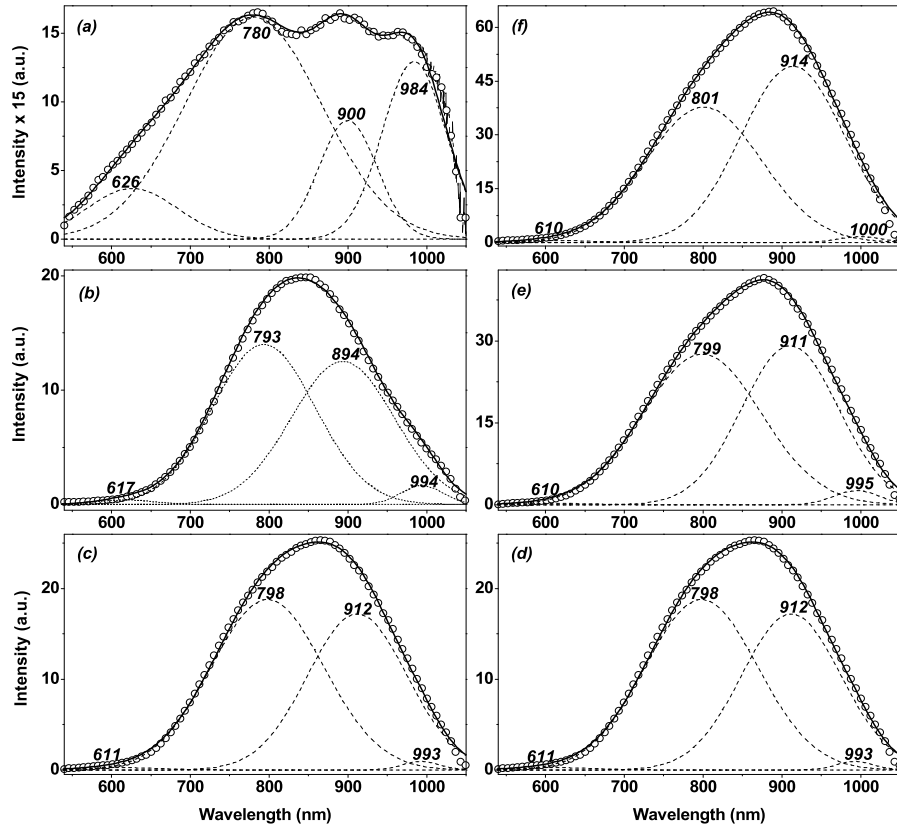


Figure 7.2: Decomposed PL spectra of the samples with $P_{Ge} = 0$ W (Si nanocrystals) annealed at 900, 1000, and 1100 °C for 1 h (a-c), and annealed at 1100 °C for 1, 3, and 5 h (d-f).

7.4 Annealing Treatment Evolution of the PL Spectra from $\text{Si}_{1-x}\text{Ge}_x$ Nanocrystals with $P_{Ge} = 10$ W

Figure 7.3 shows the PL spectra evolution of the SiGe nanocrystals with $P_{Ge} = 10$ W and with the same other sputtering parameters and annealing treatments of the samples with $P_{Ge} = 0$ W, demonstrated previous section. As can be seen, all the samples have broad spectra between 480-1050 nm with obvious decomposition tendency under annealing time and temperature with similarity and differences compared with the reference samples without Ge content. The more intense PL has been observed in the samples annealed at higher temperature of 1100 °C for prolong times of 3 and 5 h. To identify the origin and evolution of the PL with annealing parameters and distinguish between the role of quantum confinement effect and interface related radiative defects, decomposed PL spectra's of the samples have been shown in figures 7.4(a-f).

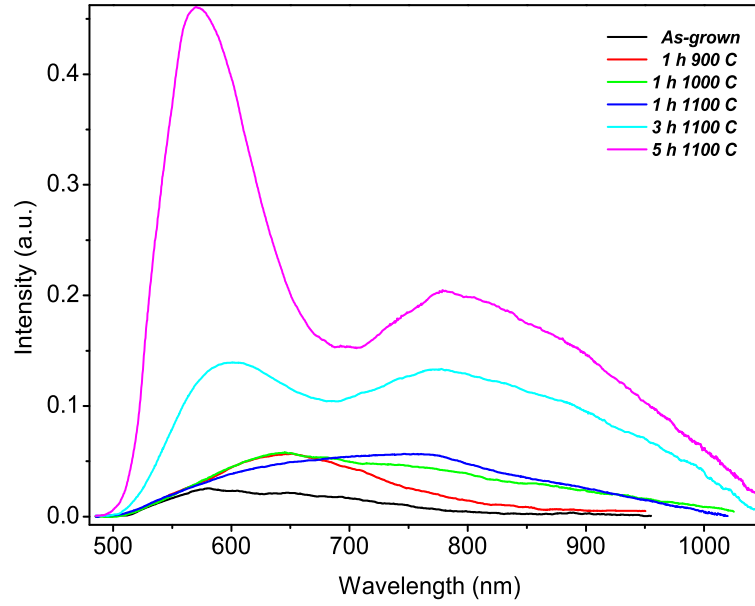


Figure 7.3: Annealing treatment evolution of room temperature PL spectra of the samples with $P_{Ge} = 10 W$.

Annealing temperature evolution of the decomposed peaks is shown in figures 7.2(a-c). As confirmed by TEM and XRD, the mean size of the nanocrystals increases from 4, 7, and 11 nm by increasing annealing temperature from 900, 1000 to 1100 °C. The first stages of the phase separation between SiGe and SiO₂ matrix starts at 900 °C and SiGe clusters are just start to form within an amorphous SiO₂ matrix and there is no well defined interface between the nanocrystals and the matrix. So, for the sample annealed at 900 °C for 1 h (figure 7.4(a)) the radiative recombination centers in SiO₂ matrix have major contribution to the PL spectra (peak *M* between 570-629 nm). By increasing annealing temperature up to 1000 °C crystalline SiGe precipitates with sizes of 7 nm accompanied by a well defined interface between the nanocrystals and the matrix have been formed. Therefore in the PL spectra, the role of quantum confined related (peak *Q* between 715-750 nm) and interface related (peak *I* between 863-908 nm) features has been increased. For the sample annealed at 1100 °C for 1 h the quantum confined related luminescence plays a dominant role.

Annealing time evolution of the samples annealed at 1100 °C has been shown in figures 7.4(d-f). For these samples mixtures of nanocrystals of all sizes with the

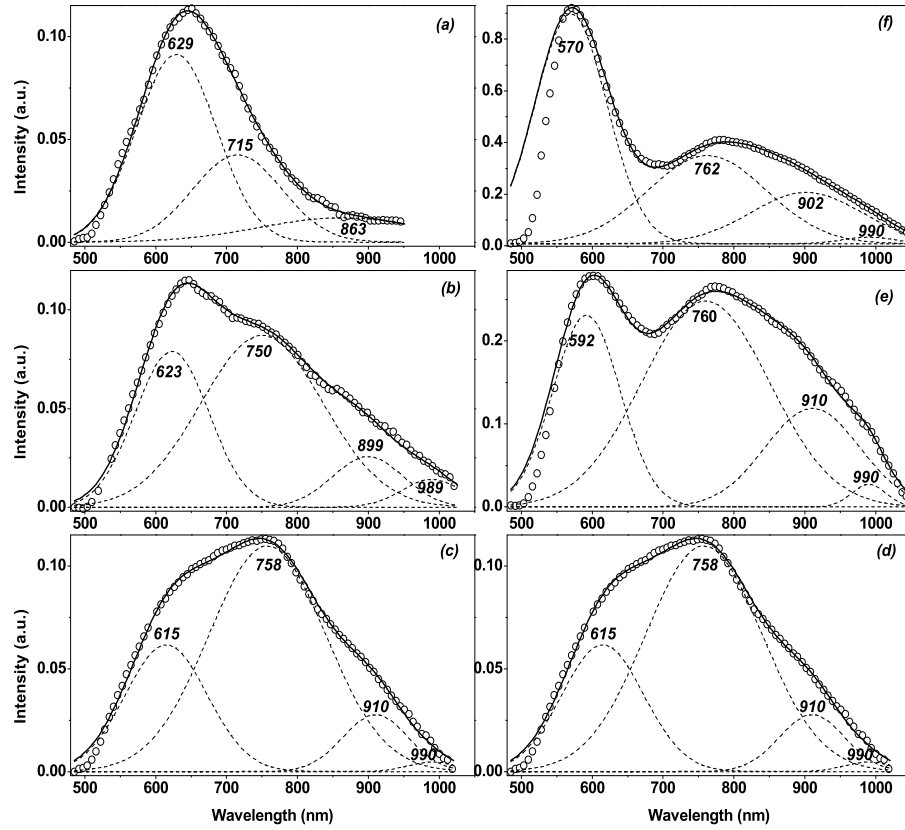


Figure 7.4: Decomposed PL spectra of the samples with $P_{Ge} = 10$ W annealed at 900, 1000, and 1100 °C for 1 h (a-c), and annealed at 1100 °C for 1, 3, and 5 h (d-f).

same average of 11 nm exist within the co-sputtered layers. This large variation can be understood by the Ostwald Ripening process where large nanocrystals grow on behalf of smaller which shrink. Although the numbers of nanocrystals with large sizes increases by prolong annealing, the average size of the nanocrystals is almost the same [11, 10, and 11]. Prolong annealing can remove nonradiative centers without increasing the nanocrystal size, and then the effect would be to cause an increased intensity and a redshift of the main PL peak [111, 131]. This redshift is not due to increasing cluster size (as confirmed by XRD), but is due to the increased relative contribution of the peaks I .

The peak M between 570-630 nm, which is also present in the as-deposited film, its high energy part has been cut off by the edge filter. In the samples without Ge content, the intensity of this peak was ignorable compared to other peaks. In these

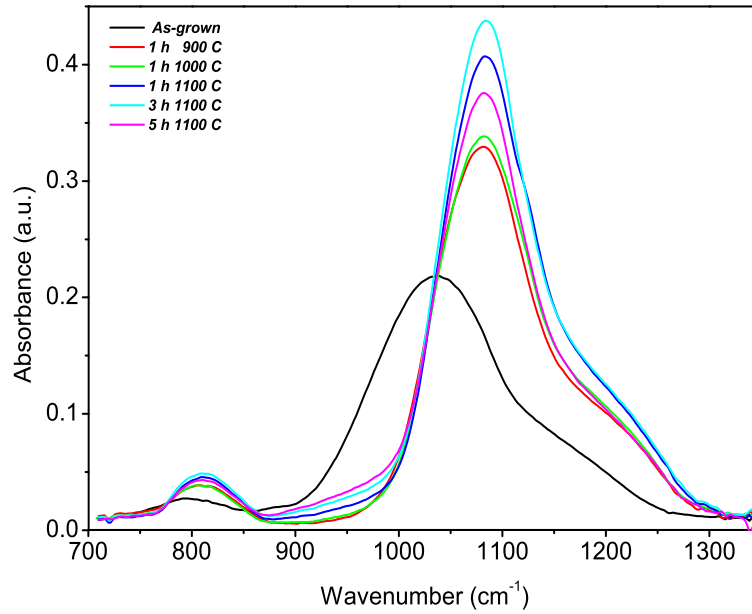


Figure 7.5: Annealing treatment evolution of FTIR spectra of the samples with $P_{Ge} = 10 W$.

samples, its contribution decreases by increasing annealing temperature and annealed out at higher temperature of $1100\text{ }^{\circ}C$. This was accompanied by disappearance of the 880 cm^{-1} in FTIR spectra, which generally attributed to NBOHC in the SiO_2 . However in the samples containing Ge due to the PL quenching in whole spectra, its intensity becomes comparable with that of quantum confined and interface related peaks. Similar to the Si samples, increasing annealing temperature reduces relative contribution of the peak M , but it still exists in the sample annealed at higher temperature of $1100\text{ }^{\circ}C$. Nevertheless, its relative contribution enhanced by prolong annealing at higher temperature of $1100\text{ }^{\circ}C$. Furthermore, a gradual blueshift was both observed by increasing annealing time and temperature. This different annealing evolution is related to the appearance of Ge related NBOHC in the SiO_2 matrix.

7.5 Evolution of the PL Spectra from $\text{Si}_{1-x}\text{Ge}_x$ Nanocrystals with the Same Annealing Treatment and Different $P_{Ge} = 0, 5, 10,$ and $20 W$

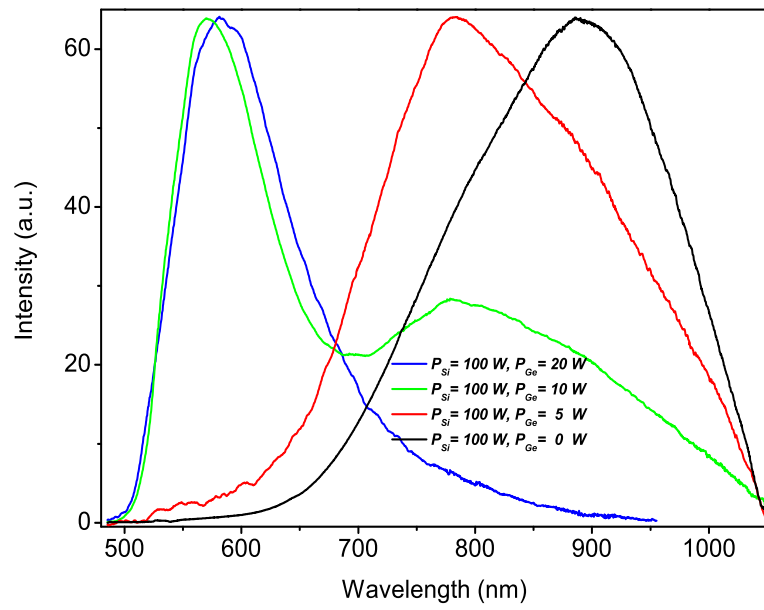


Figure 7.6: PL spectra of the samples with $P_{Ge} = 0, 5, 10,$ and 20 W annealed at $1100\text{ }^\circ\text{C}$ for 5 h .

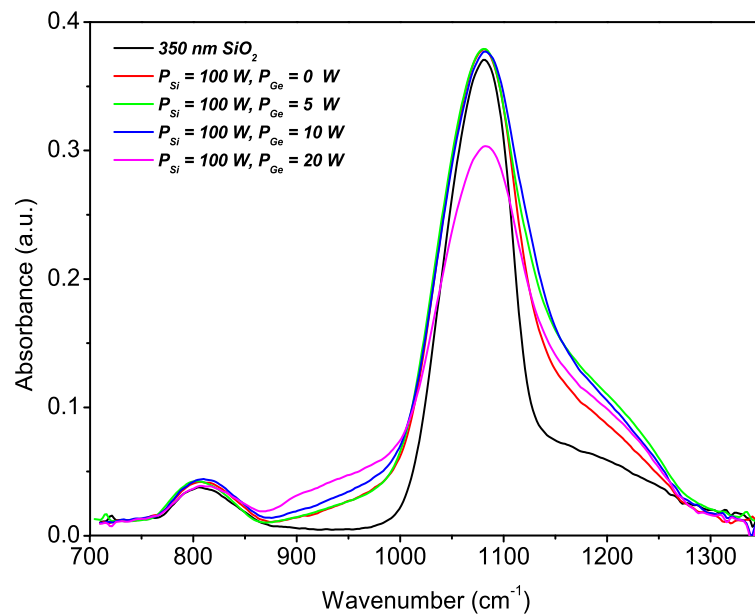


Figure 7.7: FTIR spectra of the samples with $P_{Ge} = 0, 5, 10,$ and 20 W annealed at $1100\text{ }^\circ\text{C}$ for 5 h .

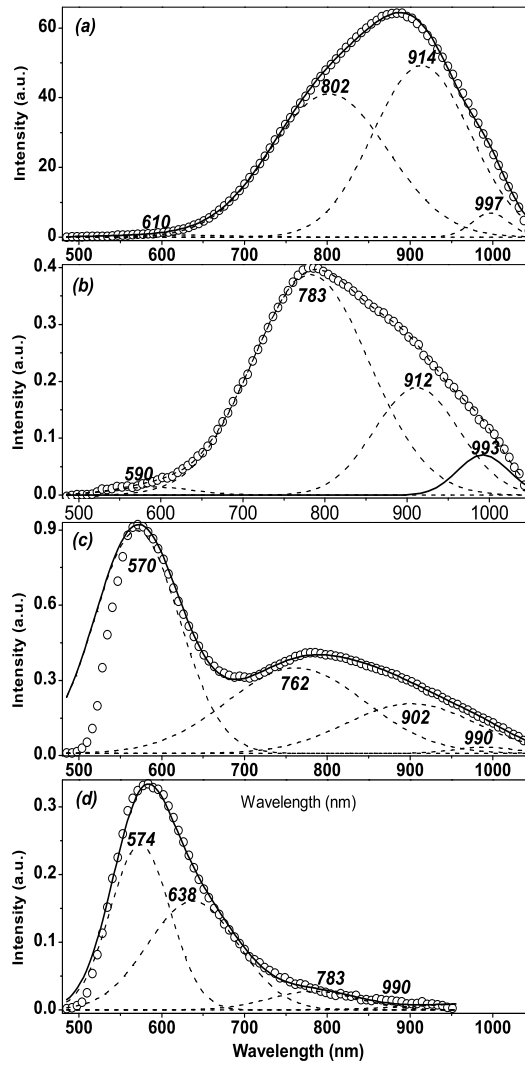


Figure 7.8: Decomposed PL spectra of the samples with $P_{Ge} = 0$ (a), 5 (b), 10 (c), and 20 W (d) annealed at $1100\text{ }^{\circ}\text{C}$ for 5 h.

CHAPTER 8

CONCLUSION

In this work we have prepared Si and $\text{Si}_{1-x}\text{Ge}_x$ nanocrystals by rf magnetron co-sputtering method. The effect of annealing parameters and Ge content of x on the structural and optical properties sandwiched $\text{SiO}_2/\text{SiO}_2$: Si: Ge/ SiO_2 nanostructures have been investigated. For characterization we have used cross-sectional high resolution electron microscope (HREM), X-ray diffraction (XRD), Raman spectroscopy (RS), Fourier transform infrared (FTIR), photoluminescence (PL), and temperature dependent PL (TDPL) techniques.

It was shown that Ge content of x , annealing temperature, and annealing time are important parameters affecting the structural and optical properties of Si and $\text{Si}_{1-x}\text{Ge}_x$ nanocrystals embedded in SiO_2 matrix. We have observed a uniform $\text{Si}_{1-x}\text{Ge}_x$ nanocrystals formation upon annealing at relatively low temperatures and short annealing time. However, Ge-rich $\text{Si}_{1-x}\text{Ge}_x$ nanocrystals do not hold their compositional uniformity when annealed at high temperatures for enough long time. A segregation process leading to separation of Ge and Si atoms from each other takes place. This process has been evidenced by a double peak formation in the XRD and Raman spectra. Possible mechanisms for this segregation are discussed in the light of experimental evidences. There are two significant candidates: A possible flux of the Si and Ge atoms in SiGe islands itself influenced by differences in atomic sizes and surface energy between Si and Ge atoms, and another flux between co-sputtered layer and the substrate involving epitaxial growth of Ge and/or SiGe precipitated onto the Si substrate.

Related to the optical properties of Si nanocrystals by fixing sputtering parameters,

influence of annealing time and temperature on the simultaneous observation and relative contribution of quantum confined and interface related radiative emission to PL spectra is investigated. Our results indicate that the larger the size of Si nanocrystals, the higher the interface state density, and the more the interface state recombination dominates over the quantum confinement process. We have shown the necessity to distinguish between nanocrystals with sizes below and above the excitons Bohr radius instead of nanocrystals with specific mean diameter size. On the other hand, temperature dependent photoluminescence (TDPL) measurements have been applied to investigate in detail the involving PL mechanisms and the competing thermally activated emission process and the thermally activated escape process of carriers into nonradiative recombination centers and/or tunneling of the excitons into the *nc*-Si/SiO₂ interface or to larger nanocrystals. Furthermore, we presented the PL results from the Si_{1-x}Ge_x nanocrystals embedded SiO₂ matrix with sizes between the Bohr radius of excitons in Si and Ge and with a larger range Ge content of *x* between 0-0.85. We discussed luminescence mechanisms in terms of radiative defects in SiO₂ matrix, *nc*-SiGe/SiO₂ interface related localized states, localized states in the amorphous Si band gap and quantum confinement of excitons in smaller nanocrystals.

REFERENCES

- [1] D. Windisch, and P. Becker, Phys. Stat. Solidi A **118** (1990) 379.
- [2] O. Brummer, V. Alex, and G. Schulze, Ann. Phys. **28** (1972) 118.
- [3] J. F. C. Baker, and M. Hart, Acta Crystallogr. A **31** (1975) 364.
- [4] J. P. Dismukes, L. Ekstrom, and R. J. Paff, J. Phys. Chem. **68** (1964) 3021.
- [5] H. J. Herzog, "In Properties of strained and relaxed silicon germanium, ed. E. Kasper, IEE emis Datareviews Series No. 12, p. 49-52", INSPEC, London (1995).
- [6] <http://www.ioffe.ru/SVA/NSM/Semicond/>.
- [7] J. Chelikowski, and M. Cohen, Phys. Rev. B **14** (1976) 556.
- [8] W. Bludau, A. Onton, and W. Heinke, J. Appl. Phys. **45** (1974) 1846.
- [9] S. Zwerdling, B. Lax, L. Roth, and K. Button, Phys. Rev. **114** (1959) 80.
- [10] Y. M. Niquet, D. Rideau, C. Tavernier, H. Jaouen, and X. Blase, Phys. Rev. B **79** (2009) 245201.
- [11] J. Weber and M. I. Alonso, Phys. Rev. B **40** (1989) 5683.
- [12] M. S. Hybertsen, Phys. Rev. Lett. **72** (1994) 1514.
- [13] D. Jurbergs, E. Rogojina, L. Mangolini, and U. Kortshagen, Appl. Phys. Lett. **88** (2006) 233116.
- [14] Y. Kanemitsu, S. Okamoto, M. Otobe, and S. Oda, Physical Review B **55** (1997) R7375.
- [15] M. V. Wolkin, J. Jorne, P. M. Fauchet, G. Allan, and C. Delerue, Phys. Rev. Lett. **82** (1999) 197.
- [16] A. Puzder, A. J. Williamson, J. C. Grossman, and G. Galli, Phys. Rev. Lett. **88** 097401 (2002).
- [17] N. Dalbosso, M. Luppi, S. Ossicini, E. Degoli, R. Magri, G. Dalba, P. Fornasini, R. Grisenti, F. Rocca, L. Pavesi, S. Boninelli, F. Priolo, C. Spinella, and F. Iacona, Phys. Rev. B **68** (2003) 085327.

- [18] A.N. Kholod, V.L. Shaposhnikov, N. Sobolev, V.E. Borisenko, F.A. Davitaya, S. Ossicini, *Phys. Rev. B* **70** (2004) 035317.
- [19] J.R. Heath, J.J. Shiang, A.P. Alivisatos, *J. Chem. Phys.* **101** (1994) 1607.
- [20] L. T. Canham, *Appl. Phys. Lett.* **57** (1990) 1046.
- [21] V. Lehmann, "Electrochemistry of Silicon", Wiley-VCH, Weinheim (2002).
- [22] W. Theip, *Surf. Sci. Rep.* **29** (1997) 91.
- [23] E. Sabatani, Y. Kalisky, A. Berman, Y. Golan, N. Gutman, B. Urbach, and A. Sa'ar, *Opt. Mater.* **38** (2008) 1766.
- [24] B. Urbach, N. Korbakov, Y. Bar-David, S. Yitzchaik, and A. Sa'ar, *J. Phys. Chem. C* **111** (2007) 16586.
- [25] S. Ben-Tabou de-Leon, R. Oren, M. E. Spira, S. Yitzchaik, and A. Sa'ar, *Appl. Phys. Lett.* **84** (2004) 4361.
- [26] H. Lin, T. Gao, J. Fantini, and M. J. Sailor, *Langmuir* **20** (2004) 5104.
- [27] S. Furukawa and T. Miyasato, *Jpn. J. Appl. Phys.* **27** (1988) L2207.
- [28] W. S. Cheong, N. M. Hwang, and D. Y. Yoon, *J. Cryst. Growth*, **204**, (1999) 52.
- [29] S. Charvet, R. Madelon, R. Rizk, B. Garrido, O. González-Varona, M. Lopez, A. Perez-Rodriguez, and J. R. Morante, *J. Luminesc.* **80** (1988) 241.
- [30] U. Kahler and H. Hofmaeister, *Opt. Mater.* **17** (2001) 83.
- [31] A. J. Kenyon, P. F. Trwoga, C. W. Pitt, and G. Rehm, *Appl. Phys. Lett.* **73** (1998) 523.
- [32] Z. X. Ma, X. B. Liao, J. He, W. C. Cheng, G. Z. Yue, Y. Q. Wang, and G. L. Kong, *J. Appl. Phys.* **83** (1998) 7934.
- [33] L. Ferraioli, M. Wang, G. Pucker, D. Navarro-Urrios, N. Damosso, C. Kom-pocholis, and L. Pavesi, *J. Nanomater.* **2007** (2007) 43491.
- [34] T. Shimizu-Iwayama, S. Nakao, and K. Saitoh, *Nucl. Instrum. Meth. B* **121** (1997) 450.
- [35] K. S. Min, K. V. Scheglov, C. M. Yang, H. A. Atwater, M. L. Brongersma, and A. Polman, *Appl. Phys. Lett.* **69** (1996) 2033.
- [36] J. Linnros, N. Lalic, A. Galeckas, and V. Grivickas, *J. Appl. Phys.* **86** (1999) 6128.

- [37] G. Ledoux, J. Gong, F. Huisken, O. Guillois, and C. Reynaud, *Appl. Phys. Lett.* **80** (2002) 4834.
- [38] D. J. Lockwood, Z. H. Lu, and J. M. Baribeau, *Phys. Rev. Lett.* **76** (1996) 539.
- [39] M. Zacharias, J. Heitmann, R. Scholz, U. Kahler, M. Schmidt, and J. Blasing, *Appl. Phys. Lett.* **80** (2002) 661.
- [40] M. Dovrat, Y. Oppenheim, J. Jedrzejewski, I. Balberg, and A. Saar, *Phys. Rev. B.* **69** (2004) 155311.
- [41] Y. Posada, I. Balberg, L. F. Fonseca, O. Resto, and S. Z. Wiesz, In *Proc. Microcrystalline and Nanocrystalline Semiconductors* **638** (2000) 1.
- [42] J. L. Vossen, and W. Kern, "Thin film processes", Academic Press, San Diego, (1978).
- [43] R. K. Waits, *J. Vac. Sci. Tech. A* **18** (2000) 1736.
- [44] D. Riabinina, C. Durand, M. Chaker, and F. Rosei, *Appl. Phys. Lett.* **88** (2006) 073105.
- [45] P. B. Hirsch, A. Howie, R. B. Nicholson, D. W. Pashley, and M. J. Whelan, "Electron Microscopy of Thin Crystals", Kreiger, London, (1977).
- [46] D. B. Williams, "Practical Analytical Electron Microscopy in Materials Science", Philips, Einhoven, (1984).
- [47] N. A. P. Mogaddam, A. S. Alagoz, S. Yerci, R. Turan, S. Foss, and T. G. Finstad, *J. Appl. Phys.* **104** (2008) 124309.
- [48] H. Munder, "in Porous Silicon Science and Technology, edited by J. C. Vial and J. Derrien", Les Editions de Physique, Les Ulis, (1995).
- [49] D. Comedi, O. H. Y. Zalloum, E. A. Irving, J. Wojcik, T. Roschuk, M. J. Flynn, and P. Mascher, *J. Appl. Phys.* **99** (2006) 023518.
- [50] J. I. Langford and A. J. C. Wilson, *J. Appl. Cryst.* **11** (1978) 102.
- [51] F. Sanchez-Bajo, and F. L. Cumbreira, *J. Appl. Cryst.* **30** (1997) 427.
- [52] M. Cernansky, *Mater. Struct.* **7** (2000) 3.
- [53] H. Wieder, M. Cardona, and C. Guamieri, *Phys. Status Solidi B* **92** (1979) 99.
- [54] T. Kirk, *Phys. Rev. B* **38**, 1255 (1988).
- [55] Z. Hajnal, P. Deak, T. Kohler, R. Kaschner, and T. Frauenheim, *Solid State Commun.* **108** (1998) 93.

- [56] L. Skuja, Solid State Commun. **84** (1992) 613.
- [57] B. Averboukh, R. Huber, K. W. Cheah, Y. R. Shen, G. G. Qin, Z. C. Ma, and W. H. Zong, J. Appl. Phys. **92** (2002) 3564.
- [58] D. J. Lockwood, Solid State Commun. **92** (1994) 101.
- [59] V. A. Belyakov, V. A. Burdov, R. Lockwood, and A. Meldrum, Adv. Opt. Tech. **2008** (2009) 279502.
- [60] J. L. Gole, and D. A. Dixon, J. Phys. Chem. B **101** (1997) 8098.
- [61] F. Anastassakis, A. Pinckzuk, E. Bumstein, F. H. Pollak, and M. Cardona, Solid State Comm. **8** (1970) 133.
- [62] A. Zwick, and R. Carles, Phys. Rev. B **48** (1993) 6024.
- [63] R. Shuker, and R. W. Gammon, Phys. Rev. Lett. **25** (1970) 222.
- [64] M. I. Alonso and K. Winer, Phys. Rev. B **39** (1989) 10056.
- [65] H. K. Shin, D. J. Lockwood, and J. M. Baribeau, Solid State Commun. **114** (2000) 505.
- [66] S. Rath, M. L. Hsieh, P. Etchegoin, and R. A. Stradling, Semicond. Sci. Technol. **18** (2003) 566.
- [67] M. A. Renucci, J. B. Renucci, and M. Cardona, "Proceeding of the 2nd International Conference on Light Scattering in Solids", Flamarrion, Paris, (1971).
- [68] D. J. Lockwood, "Semicond. Semimet. vol. 49", Academic Press, San Diego, (1998).
- [69] A. Rodriguez, M. I. Ortiz, J. Sangrador, T. Rodriguez, M. Avella, A. C. Prieto, J. Jimenez, A. Kling, and C. Ballesteros, Phys. Stat. Sol. (a) **204** (2005) 1639.
- [70] D. W. Kim, T. Kim, and S. K. Banerjee, IEEE Trans. Electron Devices **50** (2003) 1823.
- [71] I. B. Akca, A. Dana, A. Aydinli, and R. Turan, Appl. Phys. Lett. **92** (2008) 052103.
- [72] O. Nur, M. Karlsteen, M. Willander, R. Turan, B. Aslan, M. O. Tanner, and K. L. Wang, Appl. Phys. Lett. **73** (1998) 3920.
- [73] L. J. Lauhon, M. S. Gudiksen, D. Wang, and C. M. Lieber, Nature **420** (2002) 57.
- [74] J. G. Zhu, C. W. White, J. D. Budai, S. P. Withrow, and Y. Chen, J. Appl. Phys. **78** (1995) 4386.

- [75] S. Takeoka, K. Toshikiyo, M. Fujii, S. Hayashi, and K. Yamamoto, *Phys. Rev. B* **61** (2000) 15988.
- [76] J. Tarus, M. Tantarimaki, and K. Nordlund, *Nucl. Instrum. Methods Phys. Res. B* **228** (2005) 51.
- [77] A. M. Asaduzzaman and M. Springborg, *Phys. Rev. B* **74** (2006) 165406.
- [78] Y. H. Kuo, Y. K. Lee, Y. Ge, S. Ren, J. E. Roth, T. I. Kamins, D. A. B. Miller, and J. S. Harris, *Nature* **437** (2000) 1334.
- [79] A. Kolobov, H. Oyanagi, N. Usami, S. Tokumitsu, T. Hattori, S. Yamasaki, K. Tanaka, S. Ohtake, and Y. Shiraki, *Appl. Phys. Lett.* **80** (2002) 488.
- [80] Y. M. Yang, X. L. Wu, G. G. Su, G. S. Huang, J. C. Shen, and D. S. Hu, *J. Appl. Phys.* **96** (2004) 5239.
- [81] M. I. Alonso, M. D. Calle, J. O. Osso, M. Garriga, and A. R. Goni, *J. Appl. Phys.* **98** (2005) 033530.
- [82] A. Malachias, S. Kycia, G. Medeiros-Ribeiro, R. Magalhaes-Paniago R, T. I. Kamins, and R. S. Williams, *Phys. Rev. Lett.* **91** (2003) 176101.
- [83] M. Y. Valakh, V. O. Yukhymchuk, V. M. Dzhagan, O. S. Lytvyn, A. G. Milekhin, O. P. Pchelyakov, F. Alsina, and J. Pascual, *Nanotechnology* **16** (2005) 1464.
- [84] I. N. Demchenko, K. Lawniczak-Jablonska, S. Kret, A. V. Novikov, J. Y. Laval, M. Zak, A. Szczepanska, A. N. Yabloskiy, and Z. F. Krasilnik, *Nanotechnology* **18** (2007) 0115711.
- [85] E. S. Marstein, A. E. Gunnaes, A. Olsen, T. G. Finstad, R. Turan, and U. Serincan, *J. Appl. Phys.* **96** (2004) 4308.
- [86] J. D. Verhoeven, "Fundamentals of Physical Metallurgy, P. 400", John Wiley & Sons, (1975).
- [87] Y. Maeda, *Phys. Rev. B* **51** (1995) 0658.
- [88] W. K. Choia, H. G. Chew, V. Ho, V. Ng, W. K. Chim, Y. W. Ho, and S. P. Ng, *J. Cryst. Growth* **288** (2006) 79.
- [89] K. H. Heinig, B. Schmidt, A. Markwitz, R. Grotzschel, M. Strobel, and S. Oswald, *Nucl. Instrum. Methods Phys. Res. B* **148** (1999) 969.
- [90] H. Fukuda, T. Kobayashi, T. Endoh, and Y. Ueda, *Appl. Surf. Sci.* **130-132** (1998) 776.
- [91] Y. Tu and J. Tersoff, *Phys. Rev. Lett.* **98** (2007) 096103.

- [92] C. Lang, S. Kodambaka, F. M. Ross, and D. J. H. Cockayne, *Phys. Rev. Lett.* **97** (2006) 226104.
- [93] E. Kasper and K. Lyutovich, "Properties of Silicon, Germanium and SiGe", INSPEC, London, (2000).
- [94] L. Huang, F. Liu, G. H. Lu, and X. G. Gong, *Phys. Rev. Lett.* **96** (2006) 016103.
- [95] N. Daldosso and L. Pavesi, *Laser Photon Rev.* **3** (2009) 508.
- [96] A. Puzder, A. J. Williamson, J. C. Grossman, and G. Galli, *Phys. Rev. Lett.* **88** (2002) 097401.
- [97] L. Pavesi, L. Dal Negro, C. Mazzoleni, G. Franzo, and F. Priolo, *Nature* **408** (2000) 440.
- [98] G. Hadjisavvas, and P. C. Kelires, *Phys. Rev. Lett.* **93** (2004) 226104.
- [99] S. Godefroo, M. Hayne, M. Jivanescu, A. Stesmans, M. Zacharias, O. I. Lebedev, G. V. Tendeloo, and V. V. Moshchalkov, *Nature Nanotech.* **3** (2008) 174.
- [100] U. Serincan, G. Aygun, and R. Turan, *J. Luminescence* **113** (2005) 229.
- [101] S. Takeoda, M. Fujii, and S. Hayashi, *Phys. Rev. B* **62** (2000) 16820.
- [102] F. Iacona, G. Franzo, and C. Spinella, *J. Appl. Phys.* **87** (2000) 1295.
- [103] G. Ledoux, O. Guillois, D. Porterat, C. Reynaud, F. Huisken, and B. Kohn, and V. Paillard, *Phys. Rev. B* **62** (2000) 15942.
- [104] M. Kulakci, U. Serincan, R. Turan, and T. G. Finstad, *Nanotechnology* **19** (2008) 455403.
- [105] V. Osinniy, S. Lysgaard, V. Kolkovsky, V. Pankratov, and A. N. Larsen, *Nanotechnology* **20** (2009) 195201.
- [106] M. V. Wolkin, J. Jorne, P. M. Fauchet, G. Allan, and C. Delerue, *Phys. Rev. Lett.* **82** (1999) 197.
- [107] G. G. Qin, and Y. J. Li, *Phys. Rev. B* **68** (2003) 85309.
- [108] X. X. Wang, J. G. Zhang, L. Ding, B. W. Cheng, W. K. Ge, J. Z. Yu, and Q. M. Wang, *Phys. Rev. B* **72** (2005) 195313.
- [109] A. Saar, Y. Reichman, M. Dovrat, D. Krapf, J. Jedrzejewski, and I. Balberg, *Nano Lett.* **5** (2005) 2443.
- [110] J. Martin, F. Cichos, F. Huisken, and C. V. Borczyskowski, *Nano Lett.* **8** (2008) 656.

- [111] V. A. Belyakov, V. A. Burdov, R. Lockwood, and A. Meldrum, *Adv. Opt. Tech.* **2008** (2009) 279502.
- [112] A Saar, *J. Nanophotonics*, **3** (2009) 032501.
- [113] J. Heitmann, F. Muller, L. Yi, and M. Zacharias, *Phys. Rev. B* **69** (2004) 195309.
- [114] G. Allan and C. Delerue, *Phys. Rev. B* **75** (2007) 195311.
- [115] Y. Kanemitsu and S. Okamoto, *Phys. Rev. B* **56** (1997) R15561.
- [116] R. Rolver, M. Forst, O. Winkler, and B. Spangenberg, *J. Vac. Sci. Technol. A* **24** (2006) 141.
- [117] N. A. P. Mogaddam, A. S. Alagoz, S. Yerci, R. Turan, S. Foss, and T. G. Finstad, *J. Appl. Phys.* **104** (2008) 124309.
- [118] M. Lopez, B. Garrido, C. Garcia, P. Pellegrino, A. Perez-Rodriguez, J. R. Morante, C. Bonafos, M. Carrada, and A. Claverie, *Appl. Phys. Lett.* **80** (2002) 1637.
- [119] L. Dal Negro, M. Cazzanelli, L. Pavesi, S. Ossicini, D. Pacifici, G. Franzo, F. Priolo, and F. Iacona, *Appl. Phys. Lett.* **82** (2003) 4636.
- [120] Y. Chao, A. Houlton, and B. R. Horrocks, *Appl. Phys. Lett.* **88** (2006) 263119.
- [121] L. X. Yi, J. Heitmann, R. Scholz, and M. Zacharias, *J. Phys.: Condens. Matter* **15** (2003) S2887.
- [122] A. Podhorodecki, G. Zatoryb, J. Misiewicz, J. Wojcik, and P. Mascher, *J. Appl. Phys.* **102** (2007) 043104.
- [123] H. Rinnert, M. Vergnat, and A. Burneau, *J. Appl. Phys.* **89** (2001) 237.
- [124] M. Molinari, H. Rinnert, and M. Vergnat, *Europhys. Lett.* **66** (2004) 674.
- [125] M. J. Estes and G. Moddel, *Phys. Rev. B* **54** (1996) 14633.
- [126] F. Iacona, C. Bongiorno, C. Spinella, S. Boninelli, and F. Priolo, *J. Appl. Phys.* **95** (2004) 3723.
- [127] R. Lockwood, A. Hryciw, and A. Meldrum, *Appl. Phys. Lett.* **89** (2006) 263112.
- [128] S. Tiwari, F. Rana, H. Hanafi, A. Hartstein, E. F. Crabbe, and K. Chan, *Appl. Phys. Lett.* **68** (1996) 1377.
- [129] J. Linnros, N. Lalic, A. Galeckas, and V. Grivickas, *J. Appl. Phys.* **86** (1999) 6128.

- [130] L. Khriachtchev, T. Nikitin, R. Velagapudi, J. Lahtinen, and S. Novikov, *Appl. Phys. Lett.* **94** (2009) 043115.
- [131] B. Garrido, M. Lopez, O. Gonzalez, A. Perez-Rodriguez, J. R. Morante, and C. Bonafos, *Appl. Phys. Lett.* **77** (2000) 3143.
- [132] P. D. J. Calcott, K. J. Nash, L. T. Canham, M. J. Kane, and D. Brumhead, *J. Phys.: Condens. Matter* **5** (1993) L91.
- [133] M. L. Brongersma, P. G. Kik, A. Polman, K. S. Min, and H. A. Atwater, *Appl. Phys. Lett.* **76** (2000) 351.
- [134] S. Luttjohann, C. Meier, M. Offer, A. Lorke, and H. Wiggers, *Europhys. Lett.* **79** (2007) 37002.
- [135] J. Wanga, M. Righini, A. Gnoli, S. Foss, T. Finstad, U. Serincan, and R. Turan, *Solid State Commun.* **147** (2008) 461.
- [136] H. Rinnert, O. Jambois, and M. Vergnat, *J. Appl. Phys.* **106** (2009) 023501.
- [137] S. Gardelis, A. G. Nassiopoulou, N. Vouroutzis, and N. Frangis, *J. Appl. Phys.* **105** (2009) 113509.
- [138] C. W. Tsang and R. A. Street, *Phys. Rev. B* **19** (1979) 3027.
- [139] Y. Mochizuki, M. Mizuta, Y. Ochiai, S. Matsui, and N. Ohkubo, *Phys. Rev. B* **46**, (1992) 12353.
- [140] Y. Kanemitsu, *J. Luminescence* **100** (2002) 209.
- [141] W. Fuhs, *J. Non-Cryst. Solids* **354** (2008) 2067.
- [142] A. Gencer Imer, S. Yerci, A. S. Alagoz, M. Kulakci, U. Serincan, T. G. Finstad, and R. Turan, *J. Nanosci. Nanotechnol.* **10** (2010) 525.
- [143] M. Lannoo, C. Delerue, and G. Allan, *J. Luminescence* **57** (1993) 243.
- [144] S. Kim, M. C. Kim, S. Choi, K. J. Kim, H. N. Hwang, and C. C. Hwang, *Appl. Phys. Lett.* **91** (2007) 103113.
- [145] Q. S. Li, R. Q. Zhang, S. T. Lee, T. A. Niehaus, and T. Frauenheim, *Appl. Phys. Lett.* **91** (2007) 043106.
- [146] A. G. Cullis, L. T. Canham, and P. D. J. Calcott, *J. Appl. Phys.* **82** (1997) 909.
- [147] D. J. Lockwood, "Semicond. Semimet. vol. 49", Academic Press, San Diego, (1998).
- [148] D. Kovalev, H. Heckler, G. Polisski, and F. Koch, *Phys. Status Solidi B* **215** (1999) 871.

- [149] H. Takagi, H. Ogawa, Y. Yamazaki, A. Ishizaki, and T. Nakagiri, *Appl. Phys. Lett.* **56** (1990)2379.
- [150] S. Schuppler, S. L. Friedman, M. A. Marcus, D. L. Adler, Y. H. Xie, F. M. Ross, Y. J. Chabal, T. D. Harris, L. E. Brus, W. L. Brown, E. E. Chanban, P. F. Szajowski, S. B. Christman, and P. H. Citrin, *Phys. Rev. B* **52** (1995) 4910.
- [151] Y. Kanzawa, T. Kageyama, S. Takeoka, M. Fujii, S. Hayashi, and K. Yamamoto, *Solid State Commun.* **102** (1997) 533.
- [152] M. Fujii, S. Hayashi, and K. Yamamoto, "in *Recent Research Development in Applied Physics*", edited by S. G. Pandalai, Transworld Research Network, Trivandrum, Vol. 1, (1995).
- [153] S. Takeoka, M. Fujii, S. Hayashi, and K. Yamamoto, *Phys. Rev. B* **58** (1998) 7921.
- [154] J. P. Wilcoxon, P. P. Provencio, and G. A. Samara, *Phys. Rev. B* **64** (2001) 035417.
- [155] K. S. Min, K. V. Shcheglov, C. M. Yang, H. A. Atwater, M. L. Brongersma, and A. Polman, *Appl. Phys. Lett.* **68** (1996) 2511.
- [156] D. C. Paine, C. Caragianis, T. Y. Kim, Y. Shigesato, and T. Ishahara, *Appl. Phys. Lett.* **62** (1993) 2842.
- [157] M. Nogami, and Y. Abe, *Appl. Phys. Lett.* **65** (1994) 2545.
- [158] A. K. Dutta, *Appl. Phys. Lett.* **68** (1996) 1189.
- [159] H. Hu, and D. He, *Chem. Vap. Deposition* **12** (2006) 751.
- [160] T. Takagahara and K. Takeda, *Phys. Rev. B* **46** (1992) 15578.
- [161] N. A. Hill, S. Pokrant, and A. J. Hill, *J. Phys. Chem. B* **103** (1999) 3156.
- [162] Y. M. Niquet, G. Allan, C. Delerue, and M. Lanoo, *Appl. Phys. Lett.* **77** (2000) 1182.
- [163] C. Bostedt, T. van Buuren, T. M. Willey, N. Franco, L. J. Terminello, C. Heske, T. Moller, *Appl. Phys. Lett.* **84** (2004) 4056.
- [164] L. Pan, Z. Sun, and C. Sun, *Scripta Materialia* **60** (2009) 1105.
- [165] N. A. P. Mogaddam, A. Seyhan, A. G. Imer, and R. Turan, Submitted to the journal of Applied Physics.
- [166] N. A. P. Mogaddam, and R. Turan, To be submitted to the journal of Applied Physics.

VITA

NADER ASGHAR POUR MOGHADDAM

Contact Information:

Middle East Technical University, Department of Physics, Ankara, 06531, Turkey

E-mail: *nasghar@newton.physics.metu.edu.tr*, *nader.apm@gmail.com*

Tel: 0090 536 239 27 32, 0090 312 210 50 94 Fax: 0090 312 210 50 99

Fields of Research Interest:

- Fabrication, Characterization, and Optoelectronic Application of Si, Ge, and $\text{Si}_{1-x}\text{Ge}_x$ Nanocrystals
- Thermally Stimulated Conductivity Measurements in Layered Crystals
- MOS-based Radiation Sensors
- Capacitive Micromachined Ultrasonic Transducers
- Thin Film Preparation Techniques: rf magnetron co-sputtering, Thermal evaporation
- Characterization Techniques: X-ray diffraction (XRD), High-resolution transmission electron microscopy (HRTEM), Raman spectroscopy (RS), Fourier transform infrared (FTIR) spectroscopy, Photoluminescence (PL), Temperature dependent photoluminescence (TDPL), X-ray photoelectron spectroscopy (XPS), electron spin resonance (ESR) spectroscopy, Thermally stimulated current (TSC) spectroscopy, photoconductivity decay measurements

Educational and Research Experience:

- 2008- 2009

ULTRAMEMS Group, METU-MEMS with contract no 107E153

Department of Electrical and Electronics Engineering, METU, Ankara, Turkey

- 2007 -

Semiconductor Materials and Devices (SMD) group, METU-CENTER with contract no 17125

Physics Department, METU, Ankara, Turkey

- 2006 - 2007

EU FP6 projects SEMINANO under the contract, NMP4 CT2004 505285

Physics Department, METU, Ankara, Turkey

- 2004-2006

Semiconductors Research Group

Physics Department, METU, Ankara, Turkey

- 2004- 2005

Lab Instructor

Physics Department, METU, Ankara, Turkey

- 1998- 1999

Lab Instructor

Physics Department, Tabriz University, Tabriz, Iran

- 1997- 1998

Assistant Lecturer

Physics Department, Tabriz University, Tabriz, Iran

List of Publications During PhD Program:

1. Determination of trapping center parameters of Tl_2InGaS_4 -layered crystals by thermally stimulated current measurements

Nader A.P. Mogaddam, N.S. Yuksek, N.M. Gasanly, and H. Ozkan, *J. Alloy. Compd.* **417** (2006) 23.

2. Thermally stimulated currents in layered semiconductor $Tl_4In_3GaS_8$
N. M. Gasanly, H. Ozkan, and *N. A. P. Mogaddam*, *Semicond. Sci. Technol.* **21** (2006) 1250.

3. Thermally stimulated current observation of trapping centers in an undoped $Tl_4Ga_3InSe_8$ layered single crystal
N. M. Gasanly, *N. A. P. Mogaddam*, and H. Ozkan, *Cryst. Res. Technol.* **41** (2006) 1100.

4. Phase separation in SiGe nanocrystals embedded in SiO_2 matrix during high temperature annealing
N. A. P. Mogaddam, A. S. Alagoz, S. Yerci, R. Turan, S. Foss, and T. G. Finstad, *J. Appl. Phys.* **104** (2008) 124309.

5. Photoluminescence from Si Nanocrystals Embedded in SiO_2 Matrix in Weak Quantum Confined Regime
N. A. P. Mogaddam, A. Seyhan, A. Gencer Imer, R. Turan, Submitted to the journal of Applied Physics.

6. Influence of Ge Content and Annealing Treatments on the PL Properties of $nc-Si_{1-x}Ge_x$ Embedded in SiO_2 Matrix in Weak Quantum Confined Regime
N. A. P. Mogaddam, and R. Turan, To be Submitted to the journal of Applied Physics.

7. Radiation Effects on MOS Structure with Ge Nanocrystals Embedded in SiO_2
E. Yilmaz, T. Shishiyanu, *N. A. P. Mogaddam*, and R. Turan, To be Submitted to the Journal of Sensors and Actuators.

8. Influence of Annealing Temperature and Time on the Evolution of Quantum Confined and Interface Related Luminescence from $nc-Si$ by Temperature-Dependent Photoluminescence

N. A. P. Mogaddam, and R. Turan, In Progress.

9. Structural Evolution of the $nc\text{-Si}_{1-x}\text{Ge}_x$ Studied by TEM, XRD, FTIR, and Raman Spectroscopy

N. A. P. Mogaddam, and R. Turan, In Progress.

10. Structural Evolution of Ge Nanocrystals by Annealing Environments

N. A. P. Mogaddam, and R. Turan, In Progress.

Presentations:

• June 2010

E-MRS Spring Meeting 2010, Congress Center, Strasbourg, France

Radiation Effects on MOS Structure with Ge Nanocrystals Embedded in SiO_2

E. Yilmaz, T. Shishiyanu, *N. A. P. Mogaddam*, and R. Turan

• June 2009

E-MRS Spring Meeting 2009, Congress Center, Strasbourg, France

Photoluminescence from Si Nanocrystals Embedded in SiO_2 Matrix in Weak Quantum Confined Regime

*N. A. P. Mogaddam**, A. Seyhan, A.G. Imer, and R. Turan

• June 2009

5. Ulusal Nanobilim ve Nanoteknoloji Konferansi, Eskisehir, Turkey

Effect of Ge Nanocrystals in Dielectric of MOS-based Radiation Sensors

S. T. Shishiyanu*, *N. A. P. Mogaddam*, E. Yilmaz, and R. Turan

• June 2009

5. Ulusal Nanobilim ve Nanoteknoloji Konferansi, Eskisehir, Turkey

Origin of PL from Si Nanocrystals Embedded in SiO_2 Matrix in Weak Quantum Confined Regime

*N. A. P. Mogaddam**, A. Seyhan, A.G. Imer, and R. Turan

- May 2008

E-MRS Spring Meeting 2008, Congress Center, Strasbourg, France

Photoluminescence properties of SiGe nanocrystals embedded in SiO₂ matrix by magnetron sputtering

*N. A. P. Mogaddam**, A. Seyhan, A.S. Alagoz, S. Yerci, and R. Turan

- March 2008

MRS Spring 2008, Moscone West and San Francisco Marriott, USA

Si, Ge and SiGe Nanocrystals Embedded in Transparent Matrices for Light Conversion for Solar Cell Applications

R. Turan*, I. Dogan, A.S. Alagoz, *N.A.P. Moghaddam*, U. Serincan, A. Seyhan, S. Yerci, M. Kulakci, A.G. Imer, I. Yildiz

- April 2008

International Workshop on Photovoltaic Materials and Devices, Ankara, Turkey

Ge and SiGe nanocrystals Formed in Transparent Matrices for the Next Generation Solar Cell

I. Dogan*, A. S. Alagoz, *N. A. P. Mogaddam*, U. Serincan, A. Seyhan, M. Kulakci, A. Gencer Imer, I. Yildiz, S. Yerci, and R. Turan

- December 2008

2nd International Symposium on Energy and Environment, Central Hong Kong

Solar Cells and Third Generation Solar Cell Studies at METU

I. Dogan*, I. Yildiz, U. Guler, S. Ozturk, S. Canli, A. S. Alagoz, *N. A. P. Mogaddam*, M. Kulakci, U. Serincan, Z. D. Eygi, U. Bostanci, R. Turan

- August 2007

18. ULUSAL ELEKTRON MIKROSKOPI KONGRESI, Eskisehir, Turkiye

Investigation of Structural Properties of Group IV Semiconductor Nanocrystals Em-

bedded in Dielectric Matrices

Rasit Turan*, *Nader Asgharpour*, Selcuk Yerci, Ugur Serincan, Steiner Foss, Terje G. Finstad

- June 2007

International Workshop on SEMIconductor NANOstructure
Bad Honnef, Germany

Evolution of SiGe Nanocrystals in SiO₂ Matrix

*Nader Asghar Pour Moghaddam**, Selcuk Yerci, and Rasit Turan

- June 2007

International Workshop on SEMIconductor NANOstructure
Bad Honnef, Germany

Probing Group IV Nanocrystals With Diagnostic Techniques

R. Turan*, I. Dogan, A.S. Alagoz, *N.A.P. Moghaddam*, U. Serincan, A. Seyhan, S. Yerci, M. Kulakci, A.G. Imer, I. Yildiz

- June 2007

NANOTR-III, Nanoscience and Nanotechnology Conference, Bilkent, Ankara, Turkey

Effect of Annealing Time and Temperature on the Structural Property of SiGe Nanocrystals

*N.A.P. Mogaddam**, S. Yerci, S. Foss, T.G. Finstad, and R. Turan

- September 2005

Turk Fizik Dernegi 23. Fizik Kongresi, Mugla University, Turkey

Trap levels in layered semiconductor Tl₂InGaS₄

*Nader A. P. Mogaddam**, N. M. Gasanly, H. Ozkan